

ELECTRON TRANSFERS BETWEEN SMALL NANOPARTICLES

Tessa M. Carducci

A dissertation submitted to the faculty at the University of North Carolina at Chapel Hill in partial fulfillment of the requirements for the degree of Doctor of Philosophy in the Department of Chemistry.

Chapel Hill
2015

Approved by:

Royce W. Murray

R. Mark Wightman

James W. Jorgenson

Wei You

Andrew M. Moran

© 2015
Tessa M. Carducci
ALL RIGHTS RESERVED

ABSTRACT

Tessa M. Carducci: Electron transfers between small nanoparticles
(Under the direction of Royce W. Murray)

Chapter one is an introduction to electrochemistry of monolayer-protected clusters and iridium oxide nanoparticles.

Chapter two examines the temperature dependence of electron transfer (ET) kinetics in solid-state films of mixed-valent states of monodisperse, small (< 2 nm) Au monolayer protected clusters (MPCs). The mixed valent MPC films, coated on interdigitated array electrodes (IDAs), are $\text{Au}_{25}(\text{SR})_{18}^{0/1-}$, $\text{Au}_{25}(\text{SR})_{18}^{1+/0}$, and $\text{Au}_{144}(\text{SR})_{60}^{1+/0}$, where SR = hexanethiolate for Au_{144} and phenylethanethiolate for Au_{25} . Near room temperature and for *ca.* 1:1 mol:mol mixed valencies, the bimolecular ET rate constants (assuming a cubic lattice model) are $\sim 2 \times 10^6 \text{ M}^{-1} \text{ s}^{-1}$ for $\text{Au}_{25}(\text{SR})_{18}^{0/-1}$, $\sim 3 \times 10^5 \text{ M}^{-1} \text{ s}^{-1}$ for $\text{Au}_{25}(\text{SR})_{18}^{+1/0}$, and $\sim 1 \times 10^8 \text{ M}^{-1} \text{ s}^{-1}$ for $\text{Au}_{144}(\text{SR})_{60}^{+1/0}$. Their activation energy ET barriers are, respectively, 0.38 eV, 0.34 eV, and 0.17 eV. At lowered temperatures (down to *ca.* 77 K), the thermally activated (Arrhenius) ET process dissipates, revealing a tunneling mechanism in which the ET rates are independent of temperature, but among the different MPCs fall in the same order of ET rate: $\text{Au}_{144}^{+1/0} > \text{Au}_{25}^{0/-1} > \text{Au}_{25}^{+1/0}$.

Electron transfers (ET) in mixed valent ferrocene/ferrocenium materials are ordinarily facile. In contrast, **chapter three** shows the presence of *ca.* 1:1 mixed valent ferrocenated thiolates in the organothiolate ligand shells of < 2 nm dia. Au_{225} , Au_{144} , and Au_{25} monolayer protected clusters (MPCs) exerts a retarding effect on ET between them at room and at lowered temperatures. At lowered temperatures (down to *ca.* 77 K), the thermally activated

(Arrhenius) process dissipates and ET rates become temperature independent. Among the Au₂₂₅, Au₁₄₄, and Au₂₅ MPCs, the temperature independent ET rates fall in the same order of ET rate as at ambient temperatures: Au₂₂₅ > Au₁₄₄ > Au₂₅. The MPC ET activation energy barriers are little changed by the presence of ferrocenated ligands, and are primarily determined by the Au nanoparticle core size.

Chapter four introduces iridium oxide nanoparticles (IrOx NPs). The electronic conductivity of films of IrOx composed of ca. 2 nm NPs is strongly dependent on the film oxidation state. The Ir^{IV}Ox NPs can be electrochemically converted to several oxidation states, ranging from Ir^{III} to Ir^V oxides. The NP films exhibit a very high apparent conductivity, e.g., 10⁻² S cm⁻¹, when the NPs are in the oxidized +4/+5 state. When the film is fully reduced to its Ir^{III} state, the apparent conductivity falls to 10⁻⁶ S cm⁻¹.

Chapter five reports second order rate constants of associative ligand exchanges of Au₂₅L₁₈ MPCs (L = PhenylC2) of various charge states, measured by proton NMR at room temperature and below. Differences in second order rate constants (M⁻¹ s⁻¹) of ligand exchange (positive clusters ~1.9 x 10⁻⁵ vs. negative ones ~1.2 x 10⁻⁴) show that electron depletion retards ligand exchange. The ordering of rate constants between the ligands benzeneselenol > 4-bromobenzenethiol > benzenethiol reveals that exchange is accelerated by higher acidity and/or electron donation capability of the incoming ligand. Together, these observations indicate that partial charge transfer occurs between the nanoparticle and ligand during the exchange and that this is a rate-determining effect in the process.

ACKNOWLEDGEMENTS

I would first like to thank my research advisor and mentor Professor Royce W. Murray for spending the last five years helping me succeed. After over fifty years as a professor at UNC and having mentored hundreds of students, I make up an insignificant proportion of his career, but he will always be the greatest influence on mine. Even though I won't have the luxury of being steps away from his office once I leave UNC, I hope I am always able to think of what advice he might give me and use that as a guide for navigating new territory.

I would next like to thank my committee members, especially Professors R. Mark Wightman and James W. Jorgenson, for believing in my capabilities as a student and expressing enthusiasm for my research. Also, thank you to Professor John D. Simon, who gave me the opportunity to pursue undergraduate research in his lab at Duke. I don't know if I would have pursued graduate school had it not been for his example and willingness to entrust me with independent work in his lab. His integrity and vested interest in students' success will continue to inspire me throughout my career. Additionally, I would like to thank Dr. Cheleste M. Thorpe for giving me my first opportunity to conduct research in a lab.

Finally, I would like to thank my family and close friends for their patience and support throughout not only my five years of graduate school but my entire life up until this point. I am thankful that working hard and bettering myself is just as rewarding to them as it is to me.

TABLE OF CONTENTS

LIST OF FIGURES	x
LIST OF TABLES	xii
LIST OF ABBREVIATIONS AND SYMBOLS	xiii
CHAPTER 1: INTRODUCTION TO ELECTROCHEMISTRY OF MONOLAYER- PROTECTED CLUSTERS AND IRIIDIUM OXIDE NANOPARTICLES	1
1.1 Introduction	1
1.2 About MPCs – Preparation and Methods for Study and Characterization	4
1.2.1 MPC Preparation and Characterization	4
1.2.2 Voltammetry and Other Properties as a Function of Nanoparticle Size	9
1.3 ET of Au MPCs.....	16
1.3.1 ET of Au MPCs freely diffusing in solution	17
1.3.2 ET of Au MPCs in self-assembled films	20
1.3.3 ET of Au MPCs in wetted films	24
1.3.4 ET of Au MPCs in dry films	27
1.3.5 ET of Au MPCs in dry, chemically-linked films.....	29
1.3.6 Low temperature ET of Au MPCs.....	31
1.3.7 Observing single ET events of Au MPCs	33
1.4 Synthesis, electronic, and optical properties of Pd, Pt, Ru, Ag, etc. MPCs	35
1.4.1 Palladium MPCs.....	35
1.4.2 Platinum MPCs.....	37

1.4.3	<i>Ruthenium MPCs</i>	38
1.4.4	<i>Silver MPCs</i>	39
1.4.5	<i>Other metal MPCs</i>	40
1.4.6	<i>Au alloy MPCs</i>	40
1.5	Electrochemical Applications of MPCs	43
1.5.1	<i>Unique electrochemistry of surface functionalized MPCs</i>	43
1.5.2	<i>Catalysis</i>	47
1.5.3	<i>Electrochemical sensors</i>	50
1.6	Introduction to Iridium Oxide Nanoparticles	58
1.7	Tables and figures	61
CHAPTER 2: KINETICS AND LOW TEMPERATURE STUDIES OF ELECTRON TRANSFERS IN FILMS OF SMALL (< 2 NM) AU MONOLAYER PROTECTED CLUSTERS.....		75
2.1	Introduction	75
2.2	Experimental	78
2.2.1	<i>Materials</i>	78
2.2.2	<i>Synthesis of Au MPCs</i>	78
2.2.3	<i>Characterization of Au MPCs</i>	78
2.2.4	<i>Preparation of Mixed-Valent Au MPCs</i>	79
2.2.5	<i>Film Preparation on Interdigitated Array Electrodes</i>	80
2.2.6	<i>Low Temperature Conductivities of Solid-State Au MPC Films</i>	80
2.3	Results and discussion.....	82
2.3.1	<i>Electronic Conductivity of Au MPC Films from 77 to 300 K Temperatures</i>	82
2.3.2	<i>EA and σ_{EL} Measurements in the Thermally-Activated Region</i>	83

2.3.3	<i>Expression of Conductivity as Electron Self-exchange Rate Constants.</i>	85
2.4	Acknowledgements	86
2.5	Tables and figures	87
CHAPTER 3: TEMPERATURE DEPENDENCE OF SOLID STATE ELECTRON EXCHANGES OF MIXED VALENT FERROCENATED AU MONOLAYER PROTECTED CLUSTERS		92
3.1	Introduction	92
3.2	Experimental	95
3.2.1	<i>Materials.</i>	95
3.2.2	<i>Synthesis of Au MPCs.</i>	95
3.2.3	<i>Film Preparation on Interdigitated Array Electrodes.</i>	96
3.3.	Results and discussion	96
3.3.1	<i>Characterization of Au MPCs.</i>	96
3.3.2	<i>Preparation of Mixed-Valent Au MPCs.</i>	97
3.3.3	<i>Low Temperature Electronic Conductivities of Solid-State Au MPC Films.</i>	98
3.3.4	<i>Electronic Conductivity of MPC Films from 77 to 300 K.</i>	99
3.4	Acknowledgements	103
3.5	Tables and figures	104
CHAPTER 4: ELECTRONIC CONDUCTIVITY OF FILMS OF ELECTROFLOCCULATED ~2 NM IRIIDIUM OXIDE NANOPARTICLES		110
4.1	Introduction	110
4.2	Experimental	111
4.3	Results and discussion	112
4.4	Acknowledgements	114
4.5	Tables and figures	115

CHAPTER 5: INVOLVEMENT OF CHARGE TRANSFER IN LIGAND EXCHANGE REACTIONS OF Au_{25} MONOLAYER PROTECTED CLUSTERS	117
5.1 Introduction	117
5.2 Experimental	118
5.3 Results and Discussion.....	119
5.4 Acknowledgements	121
5.5 Tables and figures	122
APPENDIX A: MORE DETAILED INFORMATION ABOUT $\text{Au}_{25}(\text{SC}_2\text{Ph})_{18}$ AND $\text{Au}_{144}(\text{SC}_6\text{H}_{13})_{60}$ SYNTHESSES AND A SCHEMATIC OF THE IDA ELECTRODE.....	126
A.1 Synthesis of $\text{Au}_{144}(\text{SC}_6\text{H}_{13})_{60}$	126
A.2 Synthesis of $\text{Au}_{25}(\text{SC}_2\text{Ph})_{18}$	127
A.3 Figures	129
APPENDIX B: RECALCULATED VALUES OF σ_{EL} BASED ON THE IMPROVED ESTIMATES OF δ	130
REFERENCES	131

LIST OF FIGURES

Figure 1.1. Breakdown of X-ray crystal structure of $[\text{TOA}^+][\text{Au}_{25}(\text{SCH}_2\text{CH}_2\text{Ph})_{18}]$	62
Figure 1.2. Different physical states of monolayer-protected Au nanoparticles	63
Figure 1.3. Cyclic voltammetry of Au_{144}	64
Figure 1.4. General classification of MPC voltammetries.....	65
Figure 1.5. Au_{25} voltammetry	66
Figure 1.6. Microelectrode SWVs for particles postannealing.....	67
Figure 1.7. Cartoon of electron hopping conductivity in mixed-valent Au MPC film.....	68
Figure 1.8. Schematic drawing of a Au SNPE.....	69
Figure 1.9. Optimized structure of cluster of composition $\text{Au}_{54}\text{Ag}_{60}(\text{RSAuSR})_{30}$	70
Figure 1.10. Ferrocenated Au MPCs	71
Figure 1.11. Vapor-sensing Au MPC applications	72
Figure 1.12. Au_{25} sol-gel framework sensing application	73
Figure 1.13. Films of IrOx nanoparticles.....	74
Figure 2.1. Cartoon of electron hopping conductivity in mixed-valent Au MPC film.....	88
Figure 2.2. Differential pulse voltammetry of Au_{144} and Au_{25} MPCs.....	89
Figure 2.3. Arrhenius plot of mixed valent solid state Au MPC films	90
Figure 2.4. Arrhenius plots of mixed valent solid state Au_{25} MPC films.....	91
Figure 3.1. Differential pulse voltammetry (DPV) of ferrocenated Au MPCs.....	107
Figure 3.2. Arrhenius plots of solid-state ferrocenated Au_{144} MPC films.....	108
Figure 3.3. Arrhenius plots of solid-state ferrocenated Au_{225} MPC films.....	109
Figure 4.1. Image of a dual Pt working electrode.....	115
Figure 4.2. Conductivity measurements of the IrOx film:.....	116

Figure 5.1. NMR spectrum of $\text{Au}_{25}(\text{PhC}_2\text{S})_{18}^{-1}$ in CD_2Cl_2	123
Figure 5.2. Ligand exchange reaction extent	124
Figure 5.3. Plot of the natural log of the fraction of unexchanged ligand vs. time	125
Figure A.1. Schematic of the interdigitated array (IDA) electrode	129
Figure B.1. Arrhenius plots of solid-state nonferrocenated MPC films	130

LIST OF TABLES

Table 1.1. Known MPC nanoparticles and their ligands	61
Table 2.1. Thermally-activated ET parameters.....	87
Table 3.1. Densities obtained through pycnometry and δ	104
Table 3.2. Thermally-activated ET parameters.....	105
Table 5.1. Ligand exchange kinetics and charge state	122
Table 5.2. Ligand exchange kinetics for benzene-thiol or -selenol incoming ligands	122

LIST OF ABBREVIATIONS AND SYMBOLS

=	Double bond
≡	Triple bond
•HO	Hydroxyl
•O ²⁻	Peroxide
°C	Degrees Celsius
¹ O ₂	Singlet oxygen
AC	Alternating current
ACS	American Chemical Society
aF	Attofarad
A _{Finger}	Conductive area of IDA finger
AFM	Atomic force microscopy
Ag	Silver
Ar	Argon
A _{Total}	Total conductive area of IDA
Au	Gold
Au@Pd	Gold palladium core shell particle
AuFc ^{+1/0}	Ferrocene +1/0 redox couple on Au MPC
Az	Azurin
B	Boron
β	Electronic coupling term for ET tunneling
BBT	Bromobenzenethiol

BE	Bulk electrolysis
Bu	Butyl
C	Carbon or concentration
C _{CLU}	Cluster capacitance
C _{DL}	Double layer capacitance
Ce	Cerium
CEA	Carcinoembryonic antigen
C _{EL}	Double layer capacitance of the electrode
C _{Film}	Concentration of MPCs in film
CHANL	Chapel Hill Analytical and Nuclear Laboratory
Cl	Chlorine
cm	Centimeter
CO	Carbon monoxide
CO ₂	Carbon dioxide
C _{SAM}	Capacitance of self-assembled monolayer
Cu	Copper
CV	Cyclic voltammetry
D	Deuterium
d	Distance between two fingers (IDA gap)
D1	Delay time (in NMR)
DCE	Dichloroethane
D _E	Electron diffusion coefficient
δ	Electron hopping distance

DFT	Density functional theory
DMSO	Dimethylsulfoxide
DNA	Deoxyribonucleic acid
DOSY	Diffusion-ordered NMR spectroscopy
DPV	Differential pulse voltammetry
DSC	Differential scanning calorimetry
E_A	Activation energy
ECL	Electrochemiluminescence
E_{Elec}	Electrolysis potential
ELISA	Enzyme-linked immunosorbent assay
ϵ	Dielectric constant of the monolayer
ϵ_0	Permittivity of free space
E_{PZC}	Point (potential) of zero charge
ET	Electron transfer
eV	Electron volt
$E^{\circ}_{\text{Z,Z-1}}$	Formal potential of the Z/Z-1 redox couple
$E^{\text{Z+1/Z}}$	Formal potential of the Z+1/Z redox couple
Fc	Ferrocene
Fc-Au MPCs	Ferrocenated gold MPCs
Fe	Iron
FWHM	Full width at half-maximum
g	Grams
H	Hydrogen

H ₂ O ₂	Hydrogen peroxide
HAADF-STEM	High-angle annular dark field scanning transmission electron microscopy
HOMO	Highest occupied molecular orbital
HPLC	High performance liquid chromatography
HRP	Horseradish peroxidase
IDA	Interdigitated array electrode
IR	Infrared
Ir	Iridium
K	Kelvin
kDa	Kilodalton
k _{ET}	Rate constant of electron transfer
k _{EX}	Bimolecular self-exchange rate constant
k _{Fc,EX}	Bimolecular self-exchange rate constant between the Fc redox couple
k _{HOP}	First-order electron hopping rate constant
kJ	Kilojoules
KOH	Potassium hydroxide
L	Liters
LB	Langmuir-Blodgett
l _{EFF}	Effective ligand length
LOD	Limit of detection
LUMO	Lowest unoccupied molecular orbital
M	Molarity
m/z	Mass to charge ratio

MALDI	Matrix-assisted laser desorption ionization
meV	Milli-electron volts
μm	Micrometer
mL	Milliliter
mol	Mole
MPC	Monolayer-protected clusters
MS	Mass spectrometry
MUA	Mercaptoundecanoic acid
mV	Millivolts
MW	Molecular weight
NaBH ₄	Sodium borohydride
NaOH	Sodium hydroxide
Ni	Nickel
nm	Nanometer
nM	Nanomolar
NMR	Nuclear magnetic resonance spectroscopy
NP	Nanoparticle
O ₂	Oxygen gas
Oct	Octyl
Ω	Ohms
OER	Oxygen evolution reaction
ORR	Oxygen reduction reaction
PAMAM	Poly(amido amine)

Pd	Palladium
PEG	Polyethylene glycol
Ph	Phenyl
PhC ₂ SH	Benzeneethanethiol
π	Pi
pM	Picomolar
p-MBA	para-Mercaptobenzoic acid
PME	Protein monolayer electrochemistry
ppm	Parts per million
Pt	Platinum
QCM	Quartz crystal microbalance
QDL	Quantized double layer
r	MPC core radius
R	Gas constant
r ₀	Average edge-to-edge distance between neighboring MPC cores
r ²	Statistical measure of quality of the regression line
ROS	Reactive oxygen species
Ru	Ruthenium
S	Sulfur
s	Seconds
S/N	Signal-to-noise ratio
σ_{APP}	Apparent conductivity
σ_{EL}	Electronic conductivity

SAMs	Self-assembled monolayers
SAW	Surface acoustic wave
SAXS	Small angle x-ray scattering
Se	Selenium
SECM	Scanning electrochemical microscopy
STM	Scanning tunneling microscopy
T	Temperature
Te	Tellurium
TEM	Transition electron microscopy
TGA	Thermogravimetric analysis
THF	Tetrahydrofuran
TMMAC	N,N,N-trimethyl(8-mercaptooctyl)ammonium chloride
TOA	Tetraoctylammonium
TOF	Time-of-flight
UV-vis	Ultraviolet-visible
V	Volts or voltage
VOCs	Volatile organic compounds
z	Charge state

CHAPTER 1: INTRODUCTION TO ELECTROCHEMISTRY OF MONOLAYER-PROTECTED CLUSTERS AND IRIIDIUM OXIDE NANOPARTICLES¹

1.1 Introduction

The monolayer protected cluster (MPC) subject was born in research published by Brust and Schiffrin¹ in 1994. This authors' laboratory had at that time become interested in preparing metal nanoparticles that, in the fashion of already-known self-assembled monolayers,^{2,3} could be isolated, handled, and rationally manipulated.⁴⁻⁷ The Schiffrin contribution was an excellent synthetic pathfinder and was adopted in the author's lab with thanks to these pioneers.

Over the ensuing years, the Brust-Schiffrin synthesis has seen an evolution of variants. The metal most-chosen for the nanoparticle core is gold because the nanoparticle's surface(s) can be rather effectively protected from formation of an oxidized layer (which is problematic for Ag cores) by bonding (i.e., ligating) them with a monolayer shell of organothiolate ligands. The organothiolate ligands can bear a great variety of additional chemical functionalities, singly or as a mixture of different ligands. For smaller nanoparticles—of which those containing 25 gold atoms are important examples—the ligand “monolayer” itself has structural elements in the form of —SR—Au—SR— ring-like “staple” structures like those shown in Figure 1.1.^{8,9} This particular nanoparticle has been structurally defined by single crystal determinations for its

¹ Copyright (© 2015) From *Nanoelectrochemistry* by Tessa M. Carducci and Royce W. Murray/Shigeru Amemiya and Michael V. Mirkin. Reproduced by permission of Taylor and Francis Group, LLC, a division of Informa plc

reduced “native” $\text{Au}_{25}\text{L}_{18}^-$ ⁹ and its one-electron oxidized forms.¹⁰ Important further insights have been supplied by a density function theory representation.¹¹ It is evident from Figure 1.1 that a monolayer protected Au cluster is not simply a small clump of Au atoms to which organothiolate ligands are attached to prevent their coalescence. The nanoparticle “clump” of atoms has structure both in arrangement of its internal Au and of its organothiolate ligands.¹²

A coarse analogy to MPCs can be drawn with dendrimer structures.¹³ These have similarity to MPC nanoparticles by having multiple peripheral chemical functionalities. The analogy is structurally imperfect in the sense that dendrimers become less dense near their centers, while the opposite is true of MPCs.

The general idea of preparing a nanometer-scale particle that can be chemically functionalized is quite appealing since so much more can be varied than simply the nanoparticle diameter. Table 1.1 shows some of the different organothiolate ligands and functional groupings that have been used in Au MPC chemistry, and references to their syntheses and characterizations. The chemical behavior of the MPC is dominated by the organothiolate ligands and its appended functional groups. The different thiolate ligands also determine (or influence) nanoparticle solubility, since the nanoparticle presents its external ligand shell to the solvating medium. The ligands also contribute to the MPC optical spectrum, but the overall optical spectrum of a Au MPC tends to be dominated by the strong absorbance of the Au core. The ligands on an MPC can be identical (chemically speaking), but MPCs that bear mixtures of different ligands can also be prepared. In the latter case, one might use a mixture of ligands in the MPC synthesis, or the original ligands may have been replaced (in part or fully) by new ones in a process akin to ligand exchange for a metal complex (also termed “place exchange”).¹⁴⁻¹⁶ The author has often chosen the latter synthetic course for a pragmatic reason: preparing MPCs

from a limited set of thiols (such as hexanethiol or the thiol HSCH₂CH₂Ph) allows establishing experimental parameters that constrain the core size(s) produced. Afterwards, plus perhaps some core-size fractionation in the interest of improving monodispersity, ligands may then be changed. The chemical details of how ligand exchanges occur comprise another interesting, and still evolving, aspect of MPC chemistry. For example, consider that for ligands bound in the “staple” structures shown in Figure 1.1 to become replaced with a different organothiolate ligand, multiple bonds are broken for each organothiolate ligand. The details of such reactions remain to be adequately dissected.

There are also chemical processes which can transport Au moieties between nanoparticles. These operate in so-called “annealing” steps in MPC nanoparticle preparation.¹⁷ An initially formed mixture of different sizes of MPC nanoparticles can often be reformed into a more uniform set of nanoparticle composition(s), because there exist innate preferences for different sizes (e.g., atom numbers). The entities which are released from nanoparticles during annealing are probably similar to the tetrameric versions (AuL)₄ observable by mass spectrometry as seen by Cliffler, et al.¹⁸ While there is some research activity in extending MPC chemistry to nanoparticles in which the cores contain other metals, or mixtures thereof, this article will focus on Au MPCs.

Another important variable in regard to electrochemical experiments is the state of the nanoparticle sample. Is it dissolved in solution, or present as a film on an electrode? Figure 1.2 shows cartoons of how the nanoparticle could be presented to an electrode; there is clearly an abundance of variables. However, a variety of other kinds of measurements and ideas have been invoked which aid our understanding of electron transfer (ET) events. These include, for example, transient absorption showing aspects of the quantum confinement effect for Au

MPCs,¹⁹ ET catalysis reactions,²⁰ mass spectrometry of mixed ligand nanoparticles,²¹ ETs at liquid-liquid interfaces,²² and an important theoretical perspective regarding thiolate ligand bonding, termed “divide and protect”.²³ These and selected others are further described in the sections that follow. A variety of reviews of MPC nanoparticle electrochemistry have appeared,^{8,12,24-28} as well as journal themed issues.²⁹

1.2 About MPCs – Preparation and Methods for Study and Characterization

1.2.1 MPC Preparation and Characterization

A simple plan for preparing a thiolated Au nanoparticle is to reduce a Au salt in the presence of the selected thiol. A closer look at this reaction reveals an enormous range of choices of reaction conditions that can, variously, produce nanoparticles all of the same Au core size or nanoparticles having a mixture of sizes. A mixture of produced sizes can be induced to digest towards more uniform nanoparticle size(s) by using a prolonged reaction time, the presence or addition of excess thiol, a change in temperature, isolation of the nanoparticles following a change in solvent medium—there is a long list of options available to the nanoparticle synthesizer. Details of the list change according to whether the desired nanoparticles are aqueous or organic-soluble. The diversity of preparation chemistries is actually rather large.

The first deliberately ligand-stabilized small Au nanoparticles were described by Schmid.³⁰ The ligands were triphenylphosphine and chloride, and the Au nanoparticles were labeled as Au₅₅(Ph₃P)₁₂Cl₆. The claimed Au₅₅ composition of these nanoparticles was for some time not generally accepted—it may have been a mixture instead. However, more recent work³¹ based on MALDI mass spectrometry has confirmed the existence of alkanethiolate stabilized Au₅₅(SC₁₈H₃₇)₃₁ and Au₅₄(SC₁₈H₃₇)₃₀ nanoparticles, as well as a sensitivity of the obtained composition to the synthetic pathway employed.

As noted above, the modern era of work on thiolate-protected Au nanoparticles dawned¹ in work by Brust and Schiffrin at Liverpool University (U.K.) two decades ago (1994). In the spirit of the analytical chemistry of nanoparticles, and with a band of capable collaborators, this author hurled a variety of measurement approaches at the question: what are they? Our first contribution⁴ to this topic described nanoparticles with ca. 1.2 nm (dia.) cores coated with C8, C12, or C16 alkanethiolate ligands. Methodology covered a wide range of measurements, including ¹H and ¹³C NMR, elemental analysis, differential scanning calorimetry (DSC), thermogravimetry (TGA), diffusion-ordered NMR spectroscopy (DOSY), small-angle X-ray scattering (SAXS) data on MPC solutions, and images of films from scanning tunneling (STM), and atomic force microscopy (AFM). This early paper also presented measurements of electron hopping through dry films of these materials, demonstrating distance-dependent electron tunneling through the intervening alkanethiolate chains surrounding the Au nanoparticles. Attention next turned to their solution voltammetry,⁵ notably nanoparticles labeled with thiolated Fc groups, producing a recognizable electrochemical signal.

Besides showing the expected signature of the Fc wave, the experiment revealed that further valuable information about the nanoparticles lies in currents associated with electrochemical charging of the electrical double layers of the Au core. This charging current, like that of the Fc reaction, is mass transport-controlled. Such transport-controlled charging was an already-recognized behavior of colloidal metal nanoparticles.³² Nanoparticles bearing no electroactive ligands also produce a mass transport-controlled charging current. Additionally, if their poly-dispersity can be reduced, they can also produce a distinctive voltammetric pattern⁶ based on one electron charging steps of the nanoparticle's electrical double layer, and over a certain range of sizes, show a pattern termed "quantized double layer charging", illustrated in

Figure 1.3. This is an electrostatically driven phenomenon; the current peaks arise for increments of charging the nanoparticle's electrical double layer by successive one electron changes.

Electron microscopy is an obvious and widely available tool for the study of nanoparticles. The information content from standard TEM instrumentation, for nanoparticles with very small (1-3 nm diameter) dimensions, is somewhat constrained by the need to register multiple images to provide a representative histogram of the range of nanoparticle sizes present. Determining the atom arrangements in such small nanoparticles at very high resolution requires care with regard to avoiding “beam damage” caused by inadequate thermal dissipation. When heated sufficiently, MPCs can lose thiolate ligands and experience core-sintering. A special electron microscopy approach called high-angle annular dark field scanning transmission electron microscopy (HAADF-STEM) can produce images interpretable in terms of the numbers of Au atoms per core³³ where the intensities could be used to estimate that the average cores in two samples contained only about 13-14 Au atoms, and in another, a broader range of 183 ± 116 atoms. Also, while conventional TEM in and of itself does not provide chemical identity of the nanoparticle, many TEM instruments are equipped with X-ray emission detectors which give valuable elemental composition data.

Clearly the “analytical chemistry of very small nanoparticles” requires multiple kinds of measurements among which nanoparticle diameter is just one of several important parameters. Mass spectrometry can provide important and definitive measurements on MPCs, particularly when ligand loss and/or core fragmentation can be avoided. For the smallest nanoparticles, electrospray³⁴ and MALDI-TOF³⁵ mass spectrometry measurements have successfully provided atomically precise mass measurements. In an exploration of ligand exchange chemistry of

Au₂₅L₁₈ nanoparticles, unfragmented nanoparticles of masses > 7 kDa could be observed, and the ligand exchange reaction was demonstrated to be a stochastic process. That is, exchange of an initially uniform thiolate ligand shell on a Au nanoparticle by a different thiolate ligand quickly leads to a poly-disperse ligand mixture.³⁶ If there is no preference for bonding one ligand over the other, to the Au core, the equilibrium distribution of ligand populations would follow a binominal distribution. The mixed ligand mixture population for a Au₂₅ nanoparticle is not exactly centered, so there is a slight preference for the –SCH₂CH₂Ph ligand over the hexanethiolate ligand. This preference would be difficult to detect from a kinetically based non-equilibrium measurement.

It is generally challenging to obtain mass spectra of larger sized MPCs (such as Au₁₄₄) without incurring some nanoparticle fragmentation. This is mildly surprising since very heavy and unfragmented ions formed from protonations of multiple base sites on large biological entities are commonly observable in electrospray experiments. The multiple protonations of base sites reduce the m/z (mass/charge) ratios of such ions into m/z ranges commensurate with common mass spectrometer limits. When the same tactic (multiple charging) was attempted however to reduce the m/z values for Au₁₄₄ nanoparticles (MW approaching 40 kDa), they could not be charged to sufficiently large m/z values. This likely reflects how the small (relative to a biological entity) dimension of the nanoparticle core leads to severe electrostatic repulsion effects. This problem was addressed³⁷ for nanoparticles with Au₁₄₄ cores, by place-exchange introduction of multiple intrinsically charged thiolate ligands (i.e., ligands bearing cationic quaternary ammonium groupings). The tactic of using intrinsically charged ligands produced Au₁₄₄ nanoparticles with charge (z) values from 10+ to 15+ on the nanoparticle core, allowing

successful electrospray observations. The Au-thiolate bonding was sufficiently strong to resist ligand dissociation.

Another powerful route to observing Au nanoparticle structure is based on crystallography of single crystals of purified nanoparticles. This tactic of course classically requires obtaining a high level of nanoparticle purity, or a period of nanoparticle refining. This was successfully done for the first time by Kornberg et al,^{38,39} producing Au₁₀₂(p-MBA)₄₄ (p-MBA = p-mercaptobenzoic acid) crystals. These forerunner nanoparticles, like the Au₂₅L₁₈ variety,^{8,9} showed a proclivity for formation of semi-ring or “staple” ring structures (Figure 1.1). The central Au atoms of the Au₁₀₂ nanoparticle were packed in a Marks decahedron, with the surrounding Au atoms in somewhat complex and unusual arrangements. This paper was accompanied by a useful commentary by Whetten and Price.⁴⁰ The structural assessment of the [(Oct)₄N⁺ Au₂₅L₁₈⁻] nanoparticle anion (Figure 1.1) also was preceded by a several day-long storage of a nanoparticle sample under selected solvents and isolation by solvent-induced precipitation. After several days, needle shaped black crystals could be isolated.^{9,12} This synthetic beginning has been followed by further reports of single crystal structure determinations for Au₃₈L₂₄ (L = SC₂H₄Ph) and Au₃₆L₂₄ (L = SC₂H₄Ph) nanoparticles.^{41,42}

It is not surprising that the Au nanoparticles which have been thus far structurally defined by single crystal measurements are all in the lower size range; this reflects the challenges of attaining sufficiently monodisperse material for single crystal formation. For example, a mass spectral study⁴³ of the Au₁₄₄(SC₂H₄Ph)₆₀ nanoparticle produced a high quality mass determination, but the materials available apparently did not yield to single crystal isolation.

A different synthetic approach, devised by the Crooks laboratory, invokes dendrimer stabilization of the nanoparticles by encapsulating them. Several different nanoparticle types⁴⁴⁻

⁵⁰ have been sequestered by poly(amidoamine) dendrimers, including Pd, Pt, Au, ferromagnetic Ni, and core-shell Pd-Au and bimetallic nanoparticles. Au and Pd nanoparticles were prepared by sequestering the metal ions into the dendrimers, then reducing them. Size control was sufficient to observe the distinctive pattern of quantized double layer charging.⁵¹

1.2.2 Voltammetry and Other Properties as a Function of Nanoparticle Size

We now take up the voltammetry of nanoparticles of known or identifiable sizes. Figure 1.4 provides a general classification of MPC voltammetry according to the number of Au atoms. Nanoparticles with less than about 100 Au atoms develop an energy gap between HOMO and LUMO electronic levels, and are “molecule-like”. Au₂₅ is by far the most thoroughly investigated molecule-like nanoparticle. The energy gap decreases with increasing size and closes at about 100 atoms, where the voltammetric pattern changes to that of Figure 1.3, which is exemplified by Au₁₄₄. This pattern persists over a range of ca. 100 to 300 Au atoms per nanoparticle, which is determined by the individual double layer capacitances of the nanoparticles. Thus, Au₁₄₄ nanoparticles behave as quantum capacitors, chargeable in discrete one-electron increments well-spaced on the potential scale, as in Figure 1.3. The range of this behavior ends when the nanoparticle, and its double layer capacitance, are large enough that waves for individual one-electron increments of charge start to overlap and merge. This occurs when the voltage spacing of the current peaks approaches ca. 100 mV. Larger nanoparticles, with larger double layer capacitances ultimately yield a continuum of charging current—which is the familiar “normal” behavior of electrochemical double layer charging of electrodes. There are also a number of reported Au nanoparticle preparations in which different core dimensions have been obtained, but not explored electrochemically.

Besides the delineation of Figure 1.4, the discussion can be divided according to whether the nanoparticle is organic-soluble or water soluble; this is substantially a function of the chosen ligands. Hydrophobic ligands like hexanethiolate and phenylethanethiolate confer organic solvent solubility on the nanoparticle, whereas ligands like glutathiolate yield water soluble nanoparticles. These statements refer to nanoparticles in the core size range of ca. Au_{11} to cores larger than a few hundreds of atoms. Unfortunately, electrochemical observations on MPCs are much more constrained in aqueous media, and most of the voltammetric literature is in aprotic, organic phases. The chosen ligands of course also impact the task of preparing samples which are monodisperse in core size, or only roughly so.

Nanoparticles that are organic-soluble frequently bear ligands that are alkanethiolates or similar hydrophobic thiolates. The largest Au core size for which a distinct quantized double layer (QDL) charging pattern has been seen⁵¹ is $\text{Au}_{225}(\text{S}(\text{CH}_2)_5\text{CH}_3)_{75}$. This nanoparticle sample was admixed with Au_{144} species, but in the context of an HPLC separation the Au_{225} double layer charging peaks, spaced about 185 mV apart, could be seen. Another core size property is the optical (UV-Vis) spectrum, which can display a surface plasmon band at about 520 nm. This band appears for the Au_{225} and larger nanoparticles but is largely absent for Au_{144} and smaller nanoparticles.

The voltammetry of the 1.1 nm diameter Au_{25}^- nanoparticle, with $-\text{SCH}_2\text{CH}_2\text{Ph}$ ligands was described Figure 1.5 in detail in 2004.⁵² Unfortunately, for a period of time, owing to the limitations of TEM imaging, it was mislabeled⁵²⁻⁵⁷ as a Au_{38} nanoparticle. This was corrected in 2007^{21,34} when definitive electrospray ionization mass spectrometry of the nanoparticle was obtained. Subsequently, as noted above, the crystal structure of this nanoparticle was attained (Figure 1.1). Figure 1.5 shows that there are two pairs of oxidation waves (e.g., two doubly

occupied molecular orbitals) and one pair of reduction steps. The voltammetry was observed at lowered temperature in order to stabilize the products of the most positive and negative ET steps. There is a 1.6 V separation between the first oxidation and the first reduction, which after a 0.29V charging energy correction shows that the nanoparticle exhibits a HOMO-LUMO energy gap of ca. 1.33 V, definitely a molecule-like characteristic.

The voltammetry for the first oxidation step, $\text{Au}_{25}^{-1/0}$, shows that the ET is mildly sluggish, as was reported⁵⁸ by Maran. The sluggishness opened the door to an NMR investigation⁵⁹ of its ET kinetics, which showed that the homogeneous solution self-exchange rate constant was $3 \times 10^7 \text{ M}^{-1} \text{ s}^{-1}$ with a 25 kJ/mol activation energy barrier (E_A). This barrier energy is larger than expected for an outer sphere ET of a species of MPC size, but was consistent with the voltammetry reported by Maran⁵⁸. The larger barrier is also consistent with a detected difference⁵⁹ in Raman Au—S stretch energies for the Au—S bond in the -1 vs. zero-valent MPC oxidation states.

The electrochemical potentials for charging of Au MPC cores are affected by the chemical nature of the thiolate ligands, exhibiting substituent effects on the Au_{25} redox potentials.⁵³ This was illustrated in ligand exchange experiments on the Au_{25} nanoparticle,⁶⁰ where serially replacing the ligands $-\text{SCH}_2\text{CH}_2\text{Ph}$ on Au_{25} cores with different numbers of $-\text{SPh(p-X)}$ (where $\text{X} = -\text{NO}_2$ or $-\text{Br}$) ligands produced shifts in formal potential commensurate with general molecular knowledge of how electron induction and changes in electron density for a redox species become reflected in its redox potentials. It is interesting that these changes are linear with the number of ligands. DFT theory predictions for the effect of serially replacing $-\text{SCH}_3$ ligands with $-\text{CH}_2\text{Cl}$ ligands; the changes are again linear. Differences in slope simply reflect differences in electron-withdrawing properties of the ligands.

As shown above in Figure 1.5, doublet waves appear in the Au₂₅ nanoparticle voltammetry for the successive one electron oxidations of Au₂₅L₁₈⁻ and Au₂₅L₁₈⁰ and successive one electron reductions of Au₂₅L₁₈⁻. Having an odd number of metal centers, the “native” Au₂₅L₁₈⁻ nanoparticle (L = SC₂H₄Ph⁻) is a charged, -1 species; it would otherwise have a singly occupied HOMO level. This nanoparticle is readily oxidized when air-exposed.⁶¹ The oxidized form (Au₂₅L₁₈⁰) contains an unpaired electron and is observably paramagnetic.⁶²

Electrochemically generated luminescence (ECL) refers to experiments in which reduced and oxidized states of a species are alternately generated and allowed to react in a common diffusion layer around the electrode(s).⁶³ An alternative ECL generating mode is to reduce or oxidize the proposed emitter in the presence of another species whose reduced or oxidized form rapidly decomposes in a manner producing a strongly oxidizing or reducing state. The additional species is referred to as a co-reactant. It is known^{55,64} that Au₂₅ (and Au₁₄₄) nanoparticles exhibit luminescence in the near-IR. The Au₂₅ luminescence can also be evoked by ECL, as shown by Li, et al.⁶⁵ Li also showed that Au₂₅ ECL emission could be observed by use of the common coreactant S₂O₈²⁻ whose reduction leads to the highly electron deficient SO₄⁻ species. In a more complete report, Ding, et al⁶⁶ showed that ECL is produced when Au₂₅ reduced to the -2 state reacts with its +2 oxidized state. This reaction



produces a broad emission at 893 nm. The emission is seen only on the reduction cycle since the Au₂₅²⁻ dianion is only fleetingly stable. The emission intensity could be enhanced by using the common ECL coreactant benzoyl peroxide. The detected 893 nm photon energy is very close to the HOMO-LUMO gap energy of Au₂₅⁺ as estimated from the Au₂₅ voltammetry.

The Au₃₈ species was isolated for electrochemical study^{17,67} by Quinn in 2008. This study was important in another way as it illustrated⁶⁷ how sensitive the observed nanoparticle current-potential patterns can be to the nanoparticle's preparation history. The nanoparticles were size-focused by prolonged and repeated annealing in solutions containing excess hexanethiol ligand. The Au₃₈ study also showed how subtle differences in the preparation protocol can lead to predominance of a Au₃₈ nanoparticle product rather than Au₂₅. The voltammetric pattern—doublets of oxidation and reduction waves—that appeared (Figure 1.6)⁶⁷ for Au₃₈ nanoparticle solutions in CH₂Cl₂ qualitatively resembles that of Au₂₅ nanoparticles but with a definite difference in the voltage separation (1.2 V) between the first oxidation and first reduction steps, e.g., the HOMO-LUMO gap. The peak potential separation for Au₃₈, after a 0.3 V correction for charging energy, corresponds to a 0.9 V HOMO-LUMO energy gap, distinctly different from that (ca. 1.3 V) for Au₂₅ nanoparticles.

Another interesting aspect of the Au₃₈ nanoparticle voltammetry,¹⁷ is that oxidation of the HOMO state electron pair (and reduction into the LUMO) occurs as doublet waves. The doublet waves reflect successive removal or addition of pairs of electrons at voltages separated by the ca. 0.3 V nanoparticle charging energy. The clearness of the voltammetry in regard to this doublet from occupied electron levels is obviously quite dependent on annealing of the prepared nanoparticle sample.

Au₆₇ was established in a report by Dass et al in 2013 that included an exceptionally complete characterization⁶⁸ by optical, mass spectrometric, electrochemical and first-principles theoretical analysis. The nanoparticle was formulated as Au₆₇(SR)₃₅²⁻ where R = -CH₂CH₂Ph or hexyl. Its voltammetry (in THF) is qualitatively reminiscent of the Au₂₅ pattern of levels, showing doublets of anodic and cathodic pulse voltammetry peaks. The initial oxidation and

reduction peaks are separated by a gap of 0.74V. Based on a general similarity of its voltammetry and energy gap to that reported for a nanoparticle tentatively labeled as Au₇₅,⁶⁹ it is speculated that the latter's approximate Au atom count could be revised to Au₆₇.

The phenomenon of quantized double layer (QDL) charging^{6,12} in differential pulse voltammetry of Au₁₄₄ is illustrated in Figure 1.3. An idealized view of this phenomenon is that the current peaks correspond to increments of charging the nanoparticle's electrical double layer by successive one electron changes of the nanoparticle electron population. The clearest examples of this property have been observed for Au₁₄₄(SC₆H₁₃)₆₀.⁷⁰ A highly simplified model of QDL charging⁷¹ regards the nanoparticle, dissolved in an electrolyte solution, as a concentric sphere capacitor. The nanoparticle's ligands (alkanethiolates or –SCH₂CH₂Ph, for example) serve as the capacitor dielectric, and the MPC capacitance C_{CLU} can be thereby stated as

$$C_{CLU} = 4\pi\epsilon\epsilon_0 \frac{r}{d} (r + d) \quad (1.2)$$

where ϵ_0 is the permittivity of free space, ϵ is the dielectric constant of the monolayer, r the radius of the core, and d the chain length of the thiolate ligand. This relation shows that the core radius and monolayer chain length are the manipulable MPC variables influencing individual cluster capacitances. The cluster capacitance increases with core radius and decreases with monolayer chain length, and these effects are indeed seen in prepared Au₁₄₄ nanoparticle samples, for both solutions⁷¹ and films.⁷²

Although remarkably effective, the concentric sphere view for the capacitance of C_{CLU} is a serious over-simplification. While it does represent the expected change in capacitance with increasing alkanethiolate chain length, the model does not account for permeation of solvent into the ligand monolayer which means that the QDL peak spacing can vary with solvent.⁷² It would obviously also become impacted for multi-functionalized thiolate ligands. Another issue is that

the degree of nanoparticle molecularity may become significant. Using density-functional theory, a more molecular picture of quantized charging for Au₁₄₄ nanoparticles was put forth by Hakkinen and coworkers.⁷³ The projected densities of electron states (PDOS) immediately around the HOMO and LUMO levels for the 29 kDa (Au₁₄₅) nanoparticle show a series of levels that crudely resembles the QDL model, but the level spacing is somewhat different and less regular—as indeed the experiment reveals. The average spacing between states in the HOMO-LUMO is only 0.02 eV. If one defines molecularity as possession of a HOMO-LUMO gap, the Au₁₄₄ nanoparticle is very modestly so.

Mertens et al⁷⁴ have shown that QDL voltammetry of hexanethiolate coated MPCs of the Au₁₄₄ size can also be observed in a room temperature ionic liquid. The DPV peak spacing involving the $z = 0$ charge state was larger than the potential spacing between other voltammetric peaks.

An optical bandgap, the threshold for photons to be absorbed by a material, differs from the electrochemically detected HOMO-LUMO. The absorption involves no change in the electrical charge state of the material, unlike an ET process. The optical gap for Au₁₄₄ nanoparticles depends somewhat on the ligands but for –SH ligands, is calculated⁷⁵ to be 0.175 eV. The experimental gap for Au₁₄₄ nanoparticles with –SCH₂CH₂Ph ligands is 0.186 eV.

It is important to understand that the double layer charging peaks of MPC solutions—such as those in Figure 1.3—are only *formally* analogous to current peaks seen in conventional one electron redox reactions. Thus, the QDL charging currents^{70,76,77} are controlled by rates of diffusion of the MPCs, and mixtures of MPCs with adjacent states of core charge (z) are mixed valent solutions that follow the Nernst equation in regard to the *average* core potential. The potentials at which the QDL charging events appear can be described⁷¹ by

$$E^o_{z,z-1} = E_{PZC} + \frac{(z-1/2)e}{C_{CLU}} \quad (1.3)$$

where $E^o_{z,z-1}$ is the formal potential of the $z/(z-1)$ charge state “couple” and is given by DPV peak potentials, E_{PZC} is the potential of zero charge (i.e., $z = 0$) of the cluster, and z is signed such that $z > 0$ and $z < 0$ correspond to core “oxidation” and “reduction” respectively. This relation predicts a linear plot of $E^o_{z,z-1}$ vs. charge state (termed a “z-plot”) and is useful in allowing evaluation of an average value of C_{CLU} from its slope and inspection for irregular or systematic changes in C_{CLU} as a function of potential and charge state. Values of C_{CLU} can also, of course, be obtained from the spacing of any adjacent pair of charging peaks.

We have seen earlier that Au nanoparticles can be labeled with redox moieties (such as Fc) as part of their organothiolate ligand shell. If the nanoparticle’s ligand shell is composed entirely of redox labeled organothiolates, the density of the redox groupings on the exterior surface of the ligand shell can invoke steric constraints on the ligand population.⁵⁷ Thus, the population of hexanethiolate ligands on Au₁₄₄ nanoparticles has been estimated to be 53, whereas the estimated population of hexanethiolate ligands with terminal Fc groupings on the same core size nanoparticle is 39. This apparent steric crowding effect increases for nanoparticles of smaller core size.

1.3 ET of Au MPCs

Quantifying electron transport between Au MPCs or Au MPCs and another redox species is critical for understanding their core-size and ligand dependent properties and how to tune them for application in electronic devices. As depicted in Figure 1.2, there are three main ways in which ET in Au MPC films can be studied: in solutions, in self-assembled monolayers (SAMs), and in films that are in direct contact with the electrode surface. Within the latter category, films

can be self-assembled or dropcast, dry or solvent-wetted, or in their native state or chemically linked. Electron transport between Au MPCs for each state differs dramatically and their ET characteristics and parameters must be distinguished.

1.3.1 ET of Au MPCs freely diffusing in solution

ET in solutions- either in aqueous or organic media- is typically studied as an electron exchange between a freely diffusing Au MPC and an electrode surface. Little is known about the exact details of the interaction between MPC and electrode surface, but in an oxidation reaction, the electron is hypothesized to be transferred from within the metal core of the cluster, tunneling through the insulating ligand to the electrode surface. In a reduction reaction, the reverse process occurs.

ET in solutions of Au MPCs are typically studied by cyclic voltammetry or scanning electrochemical microscopy (SECM). A report from the Cliffel group⁷⁸ established a methodology for measuring the forward heterogeneous ET rate through the thiol monolayer of Au MPCs in solution, using the SECM feedback mode. They develop a formula for extracting the ET rate constant from SECM approach curves for monodisperse thiolate-protected Au₁₄₄ MPCs. They found that in freely diffusing solution, the MPC ligand length tends to be the more dominant factor in determining the rate constant of ET; a C₆ ligand gave an ET rate constant (0.11 cm/s) two orders of magnitude larger than C₁₂ (0.0048 cm/s). For phenylethanethiol-protected Au₁₄₄, the rate of ET was 0.035 cm/s, on the same order of magnitude as C₈ (0.024 cm/s) and one order slower than C₆, showing that ligand aromaticity is not a significant player in ET kinetics in solution. In comparing ET kinetics amongst different clusters with respect to core size, the ET rate constants for hexanethiolate-protected Au₂₅ clusters were determined by cyclic voltammetry and electrochemical impedance to be 0.015-0.022 cm/s,⁷⁹ approximately one order

of magnitude lower than the ET rate constant for hexanethiolate-protected Au₁₄₄. Looking at differences in ET kinetics amongst redox couples of the same cluster, Maran, et al.⁵⁸ measured the rate in ET in hexanethiolate-protected Au₂₅ clusters via CV and found that ET rates for the +1/0 charge state transition were slower than those of the 0/-1 redox couple, by about one-half an order of magnitude. The above results indicate that the effects on ET rate in order of most to least influential are: ligand length, core size, and redox couple.

ET kinetics have also been characterized in Au MPC molecular melts. Electron transport through the undiluted room temperature melt occurs by a diffusion-like core-to-core electron hopping process. In a molecular melt of polyethylene glycol (PEG)-protected Au₂₅ MPCs, first order electron hopping rate constant of $2 \times 10^4 \text{ s}^{-1}$ and second order rate constant of $3.8 \times 10^5 \text{ M}^{-1} \text{ s}^{-1}$ were obtained via potential step chronoamperometry.⁸⁰ In a later report, addition of electrolyte and free PEG or CO₂ as plasticizers to a molecular melt of polyethylene glycol-protected Au₂₅ MPCs resulted in the formation of a conductive room temperature molten salt. Activation energies of transport and rates of both electron and counterion transport within the melt were measured using voltammetry, chronoamperometry, and electrochemical impedance. Rates and activation energies were found to correlate closely with each other. Plasticization by addition of small molecule solvent components resulted in a four-fold increase in k_{EX} (from 1.15 to $4.4 \times 10^{-7} \text{ M}^{-1} \text{ s}^{-1}$) and halving of E_{A} (from 50 to 22 kJ mol⁻¹).⁵⁴

As an aside, note that different units are used for the homogeneous and heterogeneous ET rate constants. It is in fact not straightforward to compare these rate constants obtained through different methods and conversions between units can be approximate. Different theories can model the ET transfer as an electron diffusion coefficient (D_{E} , cm² s⁻¹), a first order reaction

(k_{HOP} , s^{-1}), or a second order (k_{EX} , $M^{-1} s^{-1}$) process. This produces the diversity of units found in the literature for electron transport in MPCs. Their equivalences are⁸⁰

$$D_E = \frac{k_{HOP}\delta^2}{6} = \frac{k_{EX}\delta^2 C}{6} \quad (1.4)$$

Calculating the ET rate constant in different ways is sometimes helpful for comparison of values across the literature. Sometimes, a more general k_{ET} is used.

It was also discovered that ET between Au MPCs in solution can be manipulated, due to electron parity of the cluster, by an applied external magnetic field. This topic is called magnetoelectrochemistry. External magnetic fields can influence ET kinetics by changing the field-induced splitting of originally degenerate energy states. Redox potentials of Au MPCs and subsequent currents become dependent on electrode orientation within the magnetic field and magnetic field strength.^{81,82}

ETs in solutions of Au MPCs can also be described in terms of their exchanges with an additional redox species in solution. Murray, et al.⁸³ showed that MPCs could undergo ET reactions with other redox-active species in their solutions. In later experiments by Kontturi et al.,⁸⁴ ET reaction between organic-soluble Au MPCs and an aqueous redox species (Ce(IV), $Fe(CN)_6^{3-/4-}$, $Ru(NH_3)_6^{3+}$, and $Ru(CN)_6^{4-}$) was measured with both feedback and potentiometric modes of SECM. Charge transfers occurring heterogeneously at the liquid-liquid interface were slow compared to electron self-exchanges between MPCs. In a report by Murray, et al.,²² the bimolecular rate constant of the reaction between organic-soluble Au_{25} clusters (misabeled as Au_{38}) and an aqueous redox species was determined through negative-feedback SECM approach curves. In agreement with predictions from Marcus theory, this process involving Au MPCs at the liquid-liquid interface was faster than ET reactions between conventional aqueous and organic redox species.

1.3.2 ET of Au MPCs in self-assembled films

In typical Au MPC ET experiments with SAMs, the clusters are linked to a metal electrode surface through a self-assembled alkyl chain monolayer with specific linking sites. The electron is presumed to be transferred to/from the tethered MPC through the chain linker to/from the electrode surface. Techniques used to measure ET rates in Au MPCs attached to SAMs are potential step voltammetry and electrochemical AC impedance. Rate constants determined through impedance measurements have the virtue of less distortion due to uncompensated resistance. Also, rate constants determined using cyclic voltammetry are explicitly based on the kinetic behavior of the sub-population of MPCs that produces the most prominent current peaks. Potential step voltammetry resolves more peaks and thus gives a better indication of the diversity of rate constants of the redox species in the monolayer.⁸⁵

Chen⁸⁶ first constructed Au MPC SAMs by incorporating some alkanedithiols into the Au MPC ligand shell in order to attach the MPCs to a gold surface. The result was a film of Au MPCs that exhibited distinctive step-like charging features. When the capacitances are in the order $C_{\text{SAM}} > C_{\text{EL}}$, quantized double layer charging phenomena could be observed in the voltammetry of the Au MPC SAMs. The charging also appeared to be rectified, suggesting that ion-pairing can alter the value of C_{EL} , depending on potential, and can be tuned to give transistor-like behavior.⁸⁷ The ET rate constants of C_4 to C_8 chain length MPC SAMs was measured via cyclic voltammetry and electrochemical impedance. In dichloromethane, the values of k_{ET} decreased from 150 to 3 s⁻¹ with increasing alkyl chain length of the SAMs and from 15.5 to 7 s⁻¹ in water.⁸⁸

A recent study measuring the ET rate constants of various metal MPCs on alkanedithiol SAMs showed that the ET rate depends on the nature of the electrode metal. This can be

explained based on the varying densities of electronic states of the different metals; the apparent ET rate constant for decanedithiol SAMs were 1170, 360 and 14 s^{-1} for MPCs of Au, Pt and Pd, respectively.⁸⁹ This is an interesting result, although it is unclear if MPC size and capping ligand were completely uniform among the clusters of different metal cores. SAMs of Au MPCs have also been formed using biferrocene dithiol derivatives.⁹⁰ The main claim to fame of Au MPC SAMs and films is that the Coulomb staircase can be observed. For disordered films, such charging is not distinctly observed.

Multilayer films can also be formed upon alkanedithiol SAMs and exhibit charging features. In an experiment looking at the effect of film thickness and chain length effect on ET in dry films, IDA electrodes were modified with dithiol (the gold fingers part) and silane (the glass part), then immersed in dithiol Au MPCs for film growth. k_{ET} was found in a steady state rotated disk electrode experiment to be dependent on film thickness and charge state.⁹¹

Another way to assemble films of Au MPC on an electrode surface is through carboxylate-metal ion linkages. For example,⁸⁵ monolayers of mercaptoundecanoic acid (MUA) on Au electrodes can be formed by immersion in an ethanol solution of MUA. Au MPCs can be attached by immersing the MUA functionalized electrodes first into ethanol solutions of Zn and then solutions of mixed monolayer hexanethiolate/MUA-protected MPCs, subsequently rinsing to remove MPCs not bound to the electrode surface. This yields a monolayer of MUA-carboxylate- Zn^{+2} -carboxylate-MUA Au MPCs on the electrode surface. The ET rate constant was measured using cyclic voltammetry (100 s^{-1}), electrochemical impedance ($90\text{-}160\text{ s}^{-1}$), and potential step voltammetry ($40\text{-}150\text{ s}^{-1}$).

Quantized charging properties were also studied in multilayered films of this type where layers of Au MPCs were linked controllably and reversibly to the underlying monolayer via the

carboxylate/(Cu²⁺ or Zn²⁺)/carboxylate linkage.⁷² The electron transport within these multilayered, or so-called polymer network films, was characterized in several ways. Murray, et al.,⁹² used cyclic voltammetry and potential step chronoamperometry to determine D_E ($\sim 10^{-9}$ cm² s⁻¹), k_{HOP} (2×10^6 s⁻¹) and k_{EX} (2×10^8 M⁻¹ s⁻¹). Note the use of second order units for k_{EX} ; the electron self-exchange rate constant reflects the bimolecularity of the process. In another experiment, Murray, et al.⁹³ determined the electronic conductivity (σ_{EL}) of such multilayered films on IDA electrodes immersed in hexane (1.8×10^{-4} Ω^{-1} cm⁻¹), acetone (1.3×10^{-4} Ω^{-1} cm⁻¹), ethanol (1.1×10^{-4} Ω^{-1} cm⁻¹), dichloromethane (2×10^{-4} Ω^{-1} cm⁻¹), and as a dry film in air (3.9×10^{-4} Ω^{-1} cm⁻¹). These data show that differences in solvation have minor effects on electron transport within the film. Increasing the length of the ligand from C₄ to C₁₂ results, however, in much larger changes (ca. 3 orders of magnitude decrease in σ_{EL}). Also significantly, the electronic conductivity of the dry film was enhanced by the presence of organic vapors, suggesting a possible application in vapor sensing. Later, Murray, et al.⁹¹ measured k_{ET} in the network polymer films by a steady state rotated disc electrode voltammetry method (1×10^5 s⁻¹) and in the dry state using IDAs (4×10^6 s⁻¹). Cu²⁺-bridged multilayer films have also been formed with Au MPCs containing a ferrocenated alkanethiolate ligand for enhanced ET.⁹⁴

Dyer, et al.⁹⁵ reported controlled assembly of films of Au MPCs by Cu²⁺-pyridine complexation. These films are analogous to Cu²⁺-carboxylate linked films. A monolayer of pyridine-terminated thiol ligand is attached to the Au electrode surface, then mixed monolayer Au MPCs containing some pyridine-terminated ligand binds Cu²⁺ along with the pyridine-terminated ligand attached to the electrode surface. Multiple layers of MPCs can be formed by alternating dipping cycles, leading to pyridine-Cu²⁺ linkages between neighboring MPCs.

Rectified charging in the presence of some hydrophobic counterions in aqueous solution was observed for these types of films as well, presumed to be caused by ion-pairing.

The Langmuir-Blodgett (LB) method is another important self-assembly strategy and results in a film made up of from one to several monolayers of MPCs on an electrode surface. In an early report by Shiffrin, et al.,⁹⁶ a self-assembled multilayered thin film was prepared consisting of alternating layers of ~ 6 nm alkanedithiol-protected Au MPCs. Electron transport throughout the film was determined to occur through an electron-hopping mechanism, suggesting that the Au MPCs in the film retain their individual character (as opposed to fusing together into larger units of bulk-like gold). σ_{EL} was ca. $10^{-4} \Omega^{-1} \text{cm}^{-1}$ and thermally activated by 0.02 eV. Electronic conductivity decreased by an order of magnitude with each additional three $-\text{CH}_2$ units in the dithiol chain. σ_{EL} of the film also increases with mechanical compression; the pressure likely affects the distance between clusters.⁹⁷ A chain length effect in multilayered self-assembled films was also observed by Vossmeier, et al.⁹⁸ Additionally, electronic conductivity was found to increase dramatically with the number of deposition layers, the largest takeoff point occurring at around five layers. This is important for understanding the quantitative nature of the current response of an Au MPC film to organic vapors, in relation to possible applications in sensing.

In order to better quantify current dependence on film thickness and the influence of counterion permeation on the onset potential, the Quinn group⁹⁹ proposed a theoretical model to describe the cyclic voltammetric responses of Langmuir-Schafer films (which are analogous to LB films but assembled differently). It was observed that cathodic peak potential shifts occur when the negative counterion is made progressively more hydrophobic. The importance of understanding ion penetration comes into play in studying electron transport in Au MPC films at

a phase boundary. The Quinn group also measured k_{ET} in an LB monolayer of ~ 6 nm Au MPCs by using SECM at the nanocluster-electrode interface. The hydrophilicity of the redox couple, $FcCH_2OH$ vs. $Fe(CN)_6^{4-}$, influenced the apparent ET rate in the Au MPC film presumably due to differences in penetration.¹⁰⁰ Chen and coworkers¹⁰¹ observed single electron charging features and measured the electronic conductivity of ~ 2 nm alkanethiolate-protected Au MPCs in a LB monolayer at the air-water interface on interdigitated array electrodes. Films of Au MPCs with C_4 and C_5 chains exhibited Ohmic, linear i - V behavior while those with longer chains underwent rectifying charge transfer attributed to differences in electrolyte penetration between the ligand shells. σ was on the order of $10^{-3} \Omega^{-1} \text{ cm}^{-1}$ and varied with the interparticle spacing of the monolayer in the LB trough.¹⁰²

Kim and Lee¹⁰³ studied electron transport at the air-water interface in LB monolayers of dithiol-protected Au_{25} and the effect of interparticle spacing. Through the use of atomically precise clusters, the effects of ligand and core size can be distinguished. Clusters with dimensions in the quantum confinement region have become increasingly relevant to applications due to their unique electronic properties and highly monodisperse synthesis. Au_{25} nanoparticles show particular promise for utility in sensing devices because of their large surface area to volume ratio. k_{HOP} through the LB monolayer was $\sim 10^6 \text{ s}^{-1}$ for C_5 dithiol and $\sim 10^4 \text{ s}^{-1}$ for C_9 dithiol.

1.3.3 *ET of Au MPCs in wetted films*

The discussion is now moved from ordered films and monolayers to films that are formed by dropcasting or some other method that yields a disordered film structure. Interparticle distance is likely less uniform in dropcast films than in self assembled films. Dropcasting is simpler than self-assembly methods and therefore more attractive for use in device fabrication,

but variability of interparticle spacing likely contributes to the fact that quantized charging features are typically not observed. Another important difference to note is that for sufficiently thick dropcast films, currents passed through the film tend to plateau, whereas in films of distinct monolayers, electron transport rate increases with each deposition layer.⁹⁹ This has important implications for devices that aim at quantitatively utilizing electronic conductivity of MPCs.

The study of Au MPC films in contact with an aqueous electrolyte has important implications for sensing and electronic devices. k_{HOP} ($\sim 10^4 \text{ s}^{-1}$) and k_{EX} ($\sim 10^5 \text{ M}^{-1} \text{ s}^{-1}$) were measured by chronoamperometry for $\sim 1.8 \text{ nm}$ hexanethiolate-protected Au MPC dropcast films contacted by an aqueous electrolyte.¹⁰⁴ Deng and Chen¹⁰⁵ investigated, using SECM, rectifying charge transfer for dropcast Au MPC films contacted by an aqueous electrolyte. They observed a mass change at the electrode with de/adsorption of counterions and their de/solvation at more positive potentials than the E_{PZC} where charging features are observed that clearly depend upon the hydrophobicity of the counterion. Electrochemical impedance revealed that electron transport within the film was slower than counterion transport by at least an order of magnitude. In another report,¹⁰⁶ they examined rectifying charge transfer in multilayered dip-dried films (i.e., a gold electrode dipped into Au MPC solution then dried), and determined that the presence of hydrophobic anions like nitrate allowed the observation of quantized charging phenomena previously unobservable in dropcast Au MPCs. Further exploring the interactions between Au MPC film, water, and counterion, Wang and Murray¹⁰⁷ observed a decrease in contact angle of a sessile ionic liquid droplet upon oxidation of the Au MPC film from Au_{144}^0 to Au_{144}^{+1} . This was attributed to the increasing hydrophilicity of the film.

There is some debate in the field on the nature of ion permeation through films of Au MPCs contacted by an aqueous electrolyte and the cause of rectifying charge transfer. Quinn, et

al.¹⁰⁸ suggest that an ion permeation rate-limited model should replace the ion rectified model of charge transfer for Au MPCs in water. Instead of assuming that an association between Au clusters and the counterion leads to rectification, the ion-limited model suggests that the observed rectification effect is due to the polarizability of the film-water interface. This would also explain rectifying effects in organic solvents and shifts in redox potentials with different counterions.

SECM was also used to determine the conductance of dropcast MPC assemblies at certain potentials using an electrochemical gating mechanism. In this experiment, a redox species in solution is reduced or oxidized at the SECM tip, then re-oxidized or re-reduced at the dropcast MPC film surface. The resulting approach curves can be fitted to calculate the electrical conductance of the film. The potential of the film is set by the relative amounts of reduced and oxidized forms of redox mediator, so different potentials can be effected by switching between different types and different proportions of redox mediators in solution. For a dropcast film of 0.81 nm hexanethiolate-protected Au MPCs, the conductance ranged between 0.05 to 0.13 $\text{G}\Omega^{-1}$ between 0.1 to 0.5 V vs. Ag/AgCl.¹⁰⁹

Murray, et al.¹¹⁰ demonstrated that ET reactions of solution species are inhibited by a film of molecule-like Au MPCs dropcast on the electrode surface if the formal potential of the redox species falls within the energy gap of the clusters. A noble metal electrode has a continuum of energy levels, so there is always overlap at their surfaces with the formal potential of the redox species. However, molecular MPCs possess distinct energy levels and a band gap. In 4% $\text{CH}_3\text{CN}/\text{H}_2\text{O}$ solution, the redox reaction of methyl viologen is completely inhibited because its formal potential lies within the band gap of Au_{25} . In addition, Li, et al.¹¹¹ studied superlattices of highly monodisperse 4.3 nm and found that the superlattice structure opened up an artificial

forbidden gap where ET is prohibited. Taking advantage of the band gap of Au MPCs in films might lead to development of selective redox sensors or transistors in the future.

1.3.4 ET of Au MPCs in dry films

ET in dry films of Au MPCs is more directly applicable to real world electronic devices than in solutions. Early studies of ET in dropcast Au MPC films demonstrated the effect of ligand length and interparticle spacing on electronic conductivity.⁴ Electron self-exchange, a bimolecular process, is typically used to describe the ET process between Au MPCs in a dry film. The reaction mechanism is taken to be



and is depicted in Figure 1.7. Saveant¹¹² proposed using a cubic lattice structure as an approximate but convenient model to describe ET in a film with fixed redox sites. White and White¹¹³ later developed a theory to describe electron hopping within a film as a random walk process, i.e. variable distance ET, which is a more accurate reflection of the highly disordered film structure.

Electron transport rates within an MPC film become maximized when the concentration of MPC^Z becomes equal to that of MPC^{Z+1} , due to the bimolecularity of the reaction. The notion of a bimolecular mechanism for ET is found in experiments of network polymer films with fixed charge gradient redox sites¹¹⁴ and mixed valent osmium bipyridine clusters.¹¹⁵ Later, it was shown that MPCs with a specific charge state in the solution retain that same charge when dried, allowing the experimenter to select specific relative proportions of donors and acceptors within a dry film.⁸³ Rate constants of ET in mixed-valent Au MPC films can therefore be expressed as¹¹²

$$k_{EX} = \frac{6(10^3)RT\sigma_{EL}}{F^2\delta^2[\text{MPC}^{Z+1}][\text{MPC}^Z]} \quad (1.6)$$

where δ is the core-to-core edge separation (cm), and relative values of $[MPC^{Z+1}]$ and $[MPC^Z]$ are calculated from the Nernst equation. Once again, rate constants of this type are typically expressed in units of $M^{-1} s^{-1}$, reflecting the bimolecularity of the reaction. σ_{EL} of solid state films is for the most part measured using IDA electrodes and calculated by obtaining a i-V curve and applying the geometric cell constant of the IDA film.

In an early study, Murray, et al. calculated σ_{EL} , E_A , and k_{EX} for films of mixed valent alkanethiolate¹¹⁶ and arenethiolate¹¹⁷ protected Au MPC films that were dropcast on IDA electrodes. It was determined that the rate of electron hopping is controlled by the tunneling transport of charge along ligand chains and by the degree of mixed valency of the clusters. For alkanethiolates, the electronic coupling coefficient (β) was 0.15 nm^{-1} per CH_2 unit of the chain, yielding a rate constant of $4 \times 10^{10} \text{ M}^{-1} \text{ s}^{-1}$ for mixed-valent hexanethiolate-protected $\text{Au}_{144}^{+1/0}$. E_A increased approximately threefold from C_6 to C_{12} . Higher rates of ET were observed for Au MPCs with aromatic ligands presumably due to enhanced electron transport within and between the overlapping, conjugated bonds.

Choi and Murray⁵⁶ discovered a significant dependence of Au MPC electron transport rate on nanoparticle core size, finding that k_{EX} for transport in $\text{Au}_{25}(\text{SC}_2\text{Ph})_{18}^{0/-1}$ films was approximately three orders of magnitude smaller than that in $\text{Au}_{144}(\text{SC}_6\text{H}_{13})_{60}^{+1/0}$ films and E_A approximately three-fold larger (20.3 vs. $\sim 6 \text{ kJ mol}^{-1}$), despite Au_{25} having an aromatic ligand. They recalculated k_{EX} for hexanethiolate-protected Au_{144} ($3 \times 10^9 \text{ M}^{-1} \text{ s}^{-1}$) due to their finding that electronic conductivity is independent of film height after $1 \mu\text{m}$. Exploiting improved monodispersity of synthesis and IDA cleaning methods, Carducci and Murray¹¹⁸ later reported k_{EX} of for the hexanethiolate-protected Au_{144} ($1 \times 10^8 \text{ M}^{-1} \text{ s}^{-1}$) and phenyl C_2 -protected Au_{25} ($2 \times 10^6 \text{ M}^{-1} \text{ s}^{-1}$). They additionally looked at the $+1/0$ charge couple of Au_{25} and found that ET was

slower by about an order of magnitude in comparison to the 0/-1 charge couple, possibly due to change in electronic structure and/or magnetism.

In dropcast MPC films, only linear, featureless, current-potential profiles can be observed in electronic conductivity measurements. However, following thermal annealing at temperatures above 300 K, well-defined staircase features of single ET can emerge, indicating lateral ET is occurring through the film.¹¹⁹ Solid state quantized charging in annealed films of $\sim\text{Au}_{314}(\text{SC}_6)_{91}$ was observed only in a narrow temperature range (300-320 K), presumably where film structure is optimized to promote interparticle ET. It is unclear what effect annealing has on the chemical structures of the MPCs and films, but lateral ET is an indication that there is some kind of structural change.¹²⁰ For quantifying ET parameters of atomically precise Au MPCs, films are typically not annealed to avoid possible thermal damage to the particles, films, and IDA electrodes. However, annealed films could potentially be very useful in novel electronic devices given their staircase charging effects.

1.3.5 ET of Au MPCs in dry, chemically-linked films

There are many reports of electron transport in dry Au MPC films that are chemically linked, i.e., carboxylate- Cu^{2+} -carboxylate bridged films or Au MPCs connected via dithiol bridges forming a tunnel junction. Covalent Au-S bonds link the Au MPCs into a network and onto gold electrode surfaces. A comparison of electron transport within solid state films of linked (dithiol-protected Au MPCs) versus unlinked (thiol) on gold electrodes revealed an increase in current by three orders of magnitude for the linked as compared to the unlinked film.¹²¹ Linked and unlinked films are discussed separately due to this large increase in electronic conductivity that this tunnel junction gives to the film.

Murray, et al.¹²² examined ET parameters for dry, carboxylate-Cu²⁺-carboxylate bridged films via atomic force microscopy. Like unlinked MPC films, σ_{EL} is exponentially dependent on the cluster spacing. β for transport between MPCs was 1.2 \AA^{-1} , which is comparable to values obtained for hydrocarbon chains, and yielded values of k_{ET} between 10^5 s^{-1} and 10^7 s^{-1} for C₄/MUA to C₁₂/MUA. The film's electronic conductivity decreases in the presence of organic vapors, possibly due to film swelling that alters the distance between clusters over which ET occurs. The change in film mass due to swelling could be monitored concurrently using QCM.⁹³ In comparison to unlinked films, the electronic conductivity of the carboxylate-Cu²⁺-carboxylate bridged films is actually lower. The metal ion/carboxylate linkers hold the MPC network polymer film together, but electronic conductivity of the film is dominated by electron transport through the non-linking alkanethiolate ligands. Thus, replacement of alkanethiolate ligands with linking MUA ligands lowers the overall electronic conductivity by providing fewer non-bonded pathways for ET.¹²³

The most common type of chemically linked film in the literature is dithiol-linked. An early report¹²⁴ found that Au MPC dithiol linked films are photoconductive and that E_A for ET within the films is strongly dependent on linker length. When films are heated at 175 °C under nitrogen atmosphere, the electronic conductivity of the film increased to close to that of bulk gold. Film thickness effects on ET, also called percolation phenomena, are often studied in dithiol linked films. Film thickness seems to have a large effect on electronic conductivity near the metal-insulator transition. In a series of experiments by Dhirani, et al.¹²⁵ using films of dithiol-linked >15 nm Au MPCs, films with fewer than six layers exhibit electron hopping conductivity while thicker films transition to metallic conductive behavior. Thinner films also

exhibit current suppression below a threshold voltage, possibly due to Coulomb blockade effects.¹²⁶

In looking at films of smaller Au MPCs (2 or 4 nm) using IDA electrodes, Zhong, et al.¹²⁷ observed trends in ET similar to films of unlinked Au MPCs in this size range. In accordance with the electron-hopping model, the results showed that E_A increases with ligand chain length and decreases with particle size. E_A fell into the range of 22-33 meV for 2 nm Au MPCs and 62-88 meV for 4 nm Au MPCs. β was only slightly larger for these dithiol linked films than unlinked films.

Another interesting and potentially useful difference between dithiol-linked and unlinked films is that the electronic conductivity of unlinked Au MPC films under CO₂ increase with pressure, whereas that of linked films decreases. Plasticization for unlinked films is postulated to increase short-range thermal motion of MPCs, enhancing ET, whereas in linked films, thermal motion is restricted by the dithiol linkages, and CO₂-induced swelling of the film results in slower ET. This report showed that the direction of response to gas sorption can be manipulated by linking the MPCs together.¹²⁸

1.3.6 Low temperature ET of Au MPCs

Some research efforts have focussed on deciphering ET behavior of MPC films at low temperatures. Determining the metal-insulator transition¹²⁹ is important, for example, in future implementation of Au MPC films in electronic devices.¹³⁰ Snow and Wohltjen¹³¹ demonstrated an effect of core size (0.86–3.61 nm) and film thickness on the metal-insulator transition temperature of an Au MPC film. Electronic conductivity increased nearly linearly with film thickness over 0.03-0.7 μm . Between 0 and 20° C, the film ET transitions from semiconductor type (thermally-activated) to metallic type (thermally-deactivated) as the core size of the Au

MPC increases. This transition, which manifests as a maximum in electronic conductivity, occurs at increasingly lower temperatures for clusters with larger core sizes.

In a series of reports from the Dhirani group,¹³² a metal-insulator transition was found to occur for Au MPC dithiol linked films of $n > 5$. They investigated¹³³ the metal-insulator transition in terms of percolation effects. Films below a certain thickness threshold exhibit thermally-activated electronic conductivity and conductance suppression near zero bias, a consequence of a probable Coulomb blockade effect. This transistor-like behavior is tunable with film thickness and temperature and could be useful in electronic device fabrication.

Nair and Kimura¹³⁴ studied the metal-insulator transition in thin films of water-soluble Au MPCs by four-point probe conductivities. For mercaptopropionyl glycine-protected Au clusters of core sizes ~ 1.6 , 3, and 4 nm, electronic conductivity increased with Au core size. Electronic conductivity was metal-like at very low temperatures but crossed over to semiconductor behavior around 60 K. Mercaptosuccinic acid-protected Au clusters of 2, 4, and 7 nm diameter exhibited a linear increase in resistivity with temperature at low temperatures and a *decrease* in resistivity with temperature at high temperatures, a somewhat surprising result. The transition temperature decreased with increasing cluster size.¹³⁵ Wieczorek, et al.¹³⁶ aptly suggest that these transitions between semiconductor-like and metal-like conductive behavior with temperature may not be hallmark of a metal-insulator transition but instead a result of the change in ET distance between neighboring clusters when the films expand thermally. It is fair to say that low temperature electronic conductivity of Au MPC films is not completely understood and remains a fruitful area of research.

The electronic conductivity of a substance exhibiting only thermally activated, or Arrhenius (linear $\ln \sigma_{EL}$ vs T^{-1}) behavior will decrease with temperature until absolute zero is

reached. However, Murray, et al.¹¹⁵ discovered ET behavior indicating the presence of a *minimum* in ETs in mixed-valent osmium bipyridine polymers. An electron tunneling mechanism, i.e., a temperature-independent ET rate, can be observed at very low temperatures where thermal energy is depleted. At ambient temperatures, the greater occupancy of the upper vibrational states allows the reaction to proceed over the classical thermal barrier. With decreasing temperature, the reaction is hypothesized to proceed increasingly by tunneling because of the depletion of the upper vibrational states.¹³⁷ In films of Au MPCs, this behavior has been observed in large, polydisperse Au MPC dithiol linked films. For example, in a two-probe configuration, differential conductance of ~ 5 nm, butanedithiol-linked Au MPC films exhibited temperature independence below 10 K due to a tunneling mechanism.¹³⁸ The variable range hopping model (linear $\ln R$ vs. $T^{-1/2}$) was used to describe the ET, with contributions from both tunneling and activated mechanisms.¹³²

1.3.7 *Observing single ET events of Au MPCs*

A promising research direction in nanoelectrochemistry is measurement of ET events of individual (single) clusters. While some progress has been made, this remains a substantially open area for future efforts. In an early work,⁶ quantized charging of a single Au₁₄₄ MPC adsorbed onto an STM tip was observed—a Coulomb staircase with six charging steps regularly spaced at 0.34 V increments between -1 to 1 V bias. Observing charging events of single clusters not only yields insight into size-dependent properties but may be of utility in miniaturization of electronic devices.

In a report from the Zhang group,¹³⁹ steady-state electrochemical responses were obtained for single, 10-30 nm citrate-stabilized Au MPCs. A single Au MPC was chemically immobilized by an amine-terminated silane onto a SiO₂-encapsulated Pt disk nanoelectrodes tip.

The single-Au MPC electrode was found to greatly enhance ET from the bare Pt electrode to the redox species in solution, as depicted in Figure 1.8. In looking at the electrocatalytic activity of the single Au MPC electrode for the oxygen reduction reaction (ORR) in a solution of KOH, the electrode exhibited good electrocatalytic activity that was tunable based on cluster size. The voltammetric response of electrode depended on the size of the cluster, as $E_{1/2}$ shifted to more positive potentials with increasing size of the Au MPC. The limiting current was higher for the single Au MPC electrode than for the bare Pt electrode and increased with particle size, indicating higher catalytic activity. When considering limiting currents normalized to the radius of the MPC, the 18 nm Au MPC electrode had the best catalytic activity for the ORR. This is an example for ET events not only of a single cluster but of the core size dependent ET properties of Au MPCs.

Another recent area of study involving single MPC ET events is particle-electrode impact electrochemistry. A series of studies from Bard and coworkers¹⁴⁰ have investigated collisions of metal nanoparticles with an inert electrode surface that result in amplification of an electrocatalytic current. A study involving 14 nm citrate-protected Au MPCs, oxidation of BH_4^- was inhibited by forming a layer of Pt oxide on the surface of a Pt ultramicroelectrode (UME). When immersed in a solution of BH_4^- and Au MPCs, current “blips” were observed that were attributed to elastic collisions between individual Au MPCs and the electrode surface. Upon each collision, there was discrete current pulse corresponding to Au MPC-catalyzed oxidation of BH_4^- . The frequency of collisions increased linearly with concentration of Au MPCs.¹⁴¹ These single particle experiments represent significant advances towards harnessing the unique ET properties of Au MPCs on the smallest scale possible and tailoring them towards possibly useful

technologies. A similar experiment was applied to observing single collisions of iridium oxide nanoparticles,¹⁴² which will be discussed further in Section 1.6.

1.4 Synthesis, electronic, and optical properties of Pd, Pt, Ru, Ag, etc. MPCs

Syntheses of MPCs with metal cores other than Au have seen many advances over the years and applications involving these particles have increased as a result. Less is known about their structures but the range of core sizes obtained is similar to that of Au MPCs, i.e., a range from molecule-like particles to larger ones whose ET properties resemble that of the bulk metal. Similar to Au MPCs, MPCs of other core metals have highly modifiable surfaces which can be functionalized with redox ligands or biomolecules to suit a specific application. A discussion of Pd MPCs is followed by another on Pt MPCs and then on less common core metal MPCs.

1.4.1 Palladium MPCs

The synthesis of Pd MPCs most commonly involves a Brust method very similar to that for Au MPCs where a Pd salt and ligand are reduced. In a study comparing the ET rate constants for MPCs (of various core metals) attached to the electrode surface via dodecanethiol SAMs, the Pd cluster exhibited slower ET rates than the Au and Pt clusters.⁸⁹ Differences in MPC electronic conductivity amongst core metals represents yet another opportunity for the design of clusters to serve a desired purpose. Furthermore, Pd clusters can be passivated with either thiol ligands or covalent Pd-C bonds. The latter is unique to Pd and presents a new opportunity for surface functionalization that is distinct from Au clusters.

Chen and Huang¹⁴³ were the first to synthesize and perform electrochemical experiments on Pd MPCs. They synthesized water-soluble Pd nanoclusters coated with a monolayer of N,N,N-trimethyl(8-mercaptooctyl)ammonium chloride (TMMAC) via reduction of PdCl₂ and TMMAC with gaseous H₂. The particles were then further functionalized with viologen moieties

incorporated into the particle protecting monolayers using surface place-exchange reactions. Surface functionalization of nanoclusters with viologen holds promise as another ET sensing platform. The two single-ET steps of the viologen moieties were observed in cyclic voltammetry for both freely diffusing viologen-Pd MPCs and as SAMs. Electrochemical impedance gave estimates of k_{ET} for the particle-bound viologens to be $1.2 \times 10^3 \text{ s}^{-1}$, which is comparable to k_{ET} rates measured for viologen SAMs on an Au electrode.

Ghosh and Chen¹⁴⁴ prepared Pd MPCs passivated by metal–carbon covalent linkages by the reduction of Pd salt with diazonium derivatives. Aliphatic radicals generated from the reduction of diazonium ligands was the proposed mechanism for formation of the stable Pd–C linkages. The group measured the electronic conductivity in solid-state films of Pd MPCs and found that the Pd–C clusters had much higher electronic conductivity than the alkanethiolate-protected Pd MPCs, exhibiting metal-like conductive properties at temperatures below 180 K, whereas alkanethiolate-Pd MPCs maintained semiconductor-like ET over the entire temperature range studied. Metal–ligand linkages are evidently rather important in governing the nature of ET and the metal-insulator transition temperature.

Pd MPCs have also been used in electrocatalytic applications. Chen, et al.¹⁴⁵ synthesized butylphenyl diazonium-protected Pd MPCs in the same manner as the above study, and more recently, the same group synthesized 1-octyne-stabilized Pd MPCs.¹⁴⁶ Single particle electrocatalysis with Pd MPCs has also been studied.^{147,148} Further examples of electrocatalytic applications of MPCs are found in section five.

Pd MPCs have also been synthesized in poly(amido amine) (PAMAM) dendrimers. Similar to dendrimer syntheses of Au MPCs, these syntheses result in relatively monodisperse samples due to reduced agglomeration and can be extracted from the dendrimer template or

immobilized onto surfaces via SAMs for making nanocluster arrays. The Crooks group⁴⁴ synthesized Pd nanoclusters encapsulated in polycationic PAMAM dendrimers that were subsequently linked to an electrode surface via a SAM and were robust enough to withstand electrochemical cycling. The same group utilized PAMAM dendrimers as a template for synthesis of relatively monodisperse Pd clusters, and then extracted the MPCs from the dendrimer into the organic phase with hexanethiol replacing the dendrimer as the passivating ligand shell. They were able to observe QDL voltammetry (without further purification steps) corresponding to Pd MPCs with cores of ca. 40, 80, and 140 Pd atoms.⁵⁰

1.4.2 *Platinum MPCs*

Like Au and Pd MPCs, the most widely used syntheses of Pt MPCs involve co-reduction of a metal salt with the desired ligand, as in the Brust method.¹⁴⁹ An early study by van Kempen, et al.¹⁵⁰ measured via STM the charging steps and Coulomb blockade of a single particle of phenanthroline-protected Pt₃₀₉ MPCs. A claim to fame of Pt MPCs is their good electrocatalytic activity for the ORR, showing an improvement over traditional Pt black catalysts.¹⁴⁹

Dendrimer syntheses have also been developed by the Crooks group⁴⁴ for Pt MPCs extracted from dendrimer templates, as well as seven different core metal ratios of bimetallic dendrimer-encapsulated Pt/Pd¹⁵¹ clusters all with core size distributions at or lower than +/- 0.3 nm. The group found that doping or mixing together one metal with another in the MPC core dramatically alters the electrochemical properties of the cluster. The cluster with a Pd to Pt ratio of 5:1 had the best catalytic activity for the ORR, with a mass activity enhancement of 2.4 compared to monometallic dendrimer-encapsulated Pt clusters. However, a 50-100 mV higher overpotential was required.¹⁵¹ The ligand shells of Pt MPCs can also be functionalized with biomolecules for sensing applications.¹⁵²

1.4.3 Ruthenium MPCs

The majority of synthesized Ru MPCs are protected by ligands through Ru-C bonds. This nanoparticle synthesis involves reaction of an alkyl lithium reagent with a ruthenium chloride salt; the nanoparticles can be further functionalized using a ligand exchange reaction. Chen and coworkers synthesized 2-3 nm octyne-protected Ru MPCs and Ru MPCs with a mixed monolayer of octyne and ethynylferrocene ligands through the formation of Ru-C \equiv bonds. The apparent bond order of the ligand C \equiv C increases upon reduction of the cluster and decreases upon oxidation, indicating that the charge of the cluster is delocalized throughout its ligand shell.¹⁵³ In the voltammetry of the ferrocenated particle, the group observed two peaks corresponding to ET of the Fc moieties, which suggests that the strong Ru-C \equiv bond facilitates intervalence transfer occurs between the Fc groups through the metallic core.¹⁵⁴ The strength of the Ru-C \equiv interaction also results in a metal-like temperature dependence of electronic conductivity for films of this cluster. β for these clusters (0.3-0.5 Å⁻¹) is much smaller than in alkanethiolate-protected Au MPCs (1.2 Å⁻¹), indicating a small contact resistance for electrons transferring between the metallic core and insulating ligand shell, a likely result of the charge delocalization capability.^{155,156}

Chen and coworkers¹⁵⁷ also synthesized pyrene-functionalized Ru MPCs passivated by metal-ligand pi bonds through olefin metathesis reactions. Similar to the Ru-C \equiv clusters, these particles also exhibit intraparticle delocalization, yielding interesting optical fluorescence properties that can be manipulated by chemical linkages. Anthracene-functionalized Ru MPCs stabilized by carbenes had activation energies for ET about one order of magnitude lower than clusters passivated by alkanethiolates due to interparticle delocalization.¹⁵⁸ Ru=N π -bonds in a nitrene-stabilized Ru MPC did not permit interparticle charge delocalization to as great a degree

as in the Ru=C and Ru-C \equiv clusters; the photoluminescence properties were diminished and only one redox peak due to Fc was observed for the ferrocene-nitrene functionalized Ru MPC.¹⁵⁹

1.4.4 Silver MPCs

Ag MPCs represent an attractive target because they have surface plasmon bands with higher extinction coefficients than Au MPCs and can also display quantized double layer charging voltammetry. Focusing first on electronic properties, Wang, et al.,¹⁶⁰ synthesized ~3.3 nm alkyl ammonium-protected Ag clusters by reducing a metal salt in the presence of the desired ligand, in a Brust-like method. They linked the MPCs to a gold electrode through SAMs, and measured the capacitance (modeled after the concentric sphere capacitor-like Au MPCs) to be ca. 0.52 aF, through differential pulse voltammetry. The metal-to-insulator transition of ~14 nm thiolate-protected Ag MPCs was less sharp than that for Au MPCs of comparable size, suggesting that the ligand monolayer of Ag MPCs is more disordered.¹⁶¹ Murray, et al.¹²⁹ synthesized polydisperse butylbenzylthiolate-protected Ag clusters with an average formula of Ag₁₄₀BBT₅₃ that display a surface plasmon in the UV-visible region and quantized double layer charging voltammetry. The room temperature electronic conductivity of these clusters was determined to be about four orders of magnitude smaller than Au₁₄₀ MPCs. Feature-rich voltammetry is difficult to obtain for Ag clusters because of interference by formation of oxide sites on the surface of the particles. Ag clusters have also been electrodeposited on Au MPC templates with different architectures, offering possible platforms for sensing or catalysis.¹⁶² Like, Au, Ag MPCs can be functionalized with biomolecules that have potential for applications in immunosensing.¹⁶³

With regards to optical properties, water soluble ~1.6 nm tiopronin-protected Ag MPCs synthesized by Huang and Murray¹⁶⁴ have luminescent properties that vary with solvent polarity

and pH. Jin and coworkers reported the highly monodisperse synthesis of dimercaptosuccinic acid-protected Ag₇ MPCs¹³⁰ as well as structural studies of a series of silver sulfide cluster ions containing 1-7 Ag atoms.¹⁶⁵ Further insight into the structure and stability of Ag clusters were gained through experiments and computations with the newly synthesized¹⁶⁶ Ag₁₅₂(SCH₂CH₂Ph)₆₀. This cluster is proposed to be comprised of a 92-atom core having icosahedral-dodecahedral symmetry and a shell of 60 Ag atoms and 60 thiolates in a network of six-membered rings. The bandgap was estimated to be ~0.4 eV with absorption at 460 nm and two luminescence peaks, one attributed to the ligated shell and the other to the core.

1.4.5 *Other metal MPCs*

Cu MPCs have been synthesized but performing voltammetry is difficult because, like Ag, Cu is easily oxidized, and the nanoparticles readily gain oxide film surfaces. Chen and Sommers¹⁶⁷ synthesized 1-2 nm Cu MPCs exhibiting quantized double layer charging voltammetry (that disappeared with aging) with capacitances of 0.82 aF. The metal-insulator transition for Cu MPCs occurs at a higher temperature than either Au or Ag, possibly due to a larger Fermi energy of the metal.¹⁶¹ In a larger size regime, 4 nm tridecylamine-protected Rh MPCs synthesized via a Brust method were found to exhibit double layer charging voltammetry with a peak spacing of 80 mV near the E_{PZC}.¹⁶⁸

1.4.6 *Au alloy MPCs*

Many research efforts have probed the structure-dependent properties of Au MPCs, utilizing core doping as a tactic. As with the Pd/Pt bimetallic clusters, doping of the core can result in dramatically different nanoparticle properties inviting further study and understanding. Most known examples of alloyed nanoclusters contain Au.

As early examples of doping of Au clusters, Hg was found to weaken and shift the surface plasmon absorption band to shorter wavelengths; a broad absorption band develops at 360 with increasing amalgamation.¹⁶⁹ In a study by Huang and Murray,¹⁶⁴ replacing atoms in the core of Ag₁₄₀ MPCs with Au via a galvanic metal exchange reaction resulted in the loss of the Ag MPC surface plasmon absorbance and emission and the growth in Au MPC emission with the final product being a bimetallic cluster containing ca. 85 Au and 55 Ag atoms. Cao, Jin, and Mirkin¹⁷⁰ functionalized Ag/Au core-shell clusters with DNA for biorecognition applications. These core-shell clusters are formed by modifying an Ag MPC with a gold salt in the presence of a reducing agent, typically NaBH₄. Bimetallic Ag/Au core-shell clusters such as these hold promise in applications because they retain their surface plasmon absorption features but are more stable than monometallic Ag clusters.

Considerable recent research has focused on the structural details of doped Au MPCs. Kumara and Dass¹³⁸ synthesized (AuAg)₁₄₄(SR)₆₀ alloy MPCs via co-reduction of gold and silver salts. These clusters exhibited enhanced surface plasmons relative to monometallic Au₁₄₄ clusters. Malola and Hakkinen¹⁷¹ deciphered structural details of the alloy cluster using a density functional theory calculation, finding that Ag was likely being incorporated into the 60 atom shell, based on a structural model of the icosahedral Au₁₄₄(SR)₆₀ that features a 114-atom metal core with 60 symmetry-equivalent surface sites and a protecting layer of 30 RS-Au-SR units (Figure 1.9). With increasing Ag content, the optical gap of the alloy cluster was found to decrease from that of the monometallic Au₁₄₄ cluster.⁷⁵

The structural distortion of the Au₂₅ nanoparticle upon atom doping can be a fruitful research endeavor because the crystal structure of Au₂₅ is known. In the CuAu₂₄(SC₂H₄Ph)₁₈ cluster, copper is at the center of the metal core, and provokes shrinking of bond distances in the

contracted core.¹⁷² Doping with Pd produces a core-shell $\text{Pd}_1\text{@Au}_{24}(\text{SC}_{12}\text{H}_{25})_{18}$ structure in which the central Pd atom is surrounded by a frame of $\text{Au}_{24}(\text{SC}_{12}\text{H}_{25})_{18}$.¹⁷³ Pd doping also increases stability of the cluster and accelerates ligand exchange rate.¹⁷⁴ The degree of distortion of geometric structure likely depends on the nature of the metal and/or doping site as this degree of distortion is not seen with Ag.¹⁷²

ET properties of doped Au MPCs have also been studied. The Crooks group⁴⁸ synthesized dendrimer-encapsulated Au/Pd core-shell (Au@Pd) clusters which could then be extracted by dodecanethiol into organic solvent. The dendrimer-encapsulated Au@Pd clusters were found to not catalyze the conversion of resazurin to resorufin, for which monometallic dendrimer-encapsulated Au clusters are catalysts.⁴⁹ The Stevenson group¹⁷⁵ synthesized bimetallic Ni-Au MPCs in dendrimers, followed by extraction with thiol, as catalysts for CO_2 production from CO and O_2 . Incorporation of Ni into the clusters results in improved absorption of O_2 onto the surface of the cluster catalyst. These observations are consistent with the importance of structure in catalytic function. Ibanez and Zamborini¹⁷⁶ found that utilizing films of Ag-doped Au MPCs would be lower in cost than monometallic Au MPC films, but weakened their sensitivity for chemiresistive detection of organic compounds by up to two orders of magnitude, likely due to formation of oxides. In $\text{Cu}_n\text{Au}_{25-n}(\text{SR})_{18}$, Negishi and coworkers¹⁷² found that doping reduces the stability of the MPC in solution and shifts the redox potentials to more negative values. Understanding the structural and electronic properties of doped particles can potentially lead to the optimization of MPC properties, such as the surface plasmon and electronic conductivity, for useful applications.

1.5 Electrochemical Applications of MPCs

The unique electrochemistry of MPCs that has been the focus of this chapter has potential usefulness in applications. The MPCs might serve as electrocatalysts or be incorporated into electrochemical sensing devices. The advantages of atomically precise MPCs (i.e., distinct energy levels, band gaps) can be envisioned in applications in sensors and as electrocatalysts. The unique electrochemistry of specific types of MPC surface functionalization will be discussed first, followed by applications of these and of unmodified Au MPCs in electrocatalytic and sensing applications.

1.5.1 *Unique electrochemistry of surface functionalized MPCs*

The surface ligands of the MPC can influence its electronic structure and voltammetric responses. Modifying the surface of an MPC with ligands that suit a particular application is possible, and incorporating a ligand that contains a redox moiety allows the MPC to be electroactive in a chosen potential region.

In an important early work, Murray, et al.,⁵ showed that functionalization of Au MPCs with a ferrocene (Fc) thiol via a place exchange reaction led to surprising multi-ET reactions for both freely diffusing clusters and for a partial monolayer of electrode-adsorbed clusters. The most highly functionalized Au MPCs were determined via bulk electrolysis, to contain 15 Fc units. They are potential multi-electron donor/acceptor reagents and catalysts; previously, multi-ET reagents were solely electroactive polymers. Murray, et al.⁵⁷ later synthesized fully ferrocenated Au MPCs with core sizes ~ 55, 140, 225, and 314 Au atoms and average ligand numbers of 37, 39, 43, and 58 ferrocenated ligands, respectively. The synthesis followed the Brust method where the amount of Fc thiol relative to Au was varied to produce different sized clusters. The core sizes obtained for the ferrocenated forms are similar to those when non-

ferrocenated thiolate ligands are employed, but the total number of ligands is lower due to the Fc steric bulk. These MPCs have the capacity to transfer many electrons within a small range of potential, up to 60 per Au core for the largest sized MPC.

More recently, Schiffrin and coworkers¹⁷⁷ synthesized 1.8 nm Au MPCs containing 4, 7 or 10 Fc thiolate ligands using a place exchange reaction. The place exchange method incorporates a smaller amount of Fc thiol into the ligand shell. The group was able to distinguish between voltammetric peaks from quantized charging events of the MPC core, from ET events of the Fc moieties. Multi-ET was observed and attributed to fast rotational diffusion of the MPC at the electrode surface, as opposed to electron self-exchange between individual Fc moieties. Fc-labeled Au MPCs can be further functionalized with biomolecules,¹⁷⁸ enhancing current response in biosensor applications.

Films of one to several monolayers of $\text{Au}_{225}(\text{SC}_6\text{Fc})_{43}$ MPCs on Pt electrodes can be formed by applying a potential to oxidize the Fc sites. Their associated electrolyte anions are part of the film structure, forming bridges with the positively charged Fc moieties (Figure 1.10 a). At slow potential scan rates, voltammetric peaks (Figure 1.10 b) due to redox activity of the Fc film are significantly narrowed (35 mV FWHM as compared to ideal 90 mV), likely due to “attractive” interactions between neighboring nanoclusters.¹⁷⁹ Multilayered thin films of Fc Au MPCs prepared in the LB style have also been prepared and studied electrochemically. Films become less conductive with increasing thickness, resulting in an anodic shift of the Fc formal potential.¹⁸⁰

To study ET responses of Fc Au MPCs on more explicitly controlled electrode surfaces, Murray, et al.¹⁸¹ performed voltammetry on $\text{Au}_{225}(\text{SC}_6\text{Fc})_{43}$ adsorbed onto anionic SAMs. From this study, it was concluded that there are three different interactions that can contribute to MPC

adsorption: (i) interaction between MPCs and SAM surfaces (if present), (ii) lateral interactions between MPCs due to bridging electrolyte ions, and (iii) specific adsorption between electrolyte ions and the bare electrode surface. The use of SAMs for Fc MPC attachment therefore yields the strongest absorption, which is important for stable Fc voltammetry. Another study from Murray, et al.¹⁸² incorporated some positively charged tetraethyl ammonium-thiolate ligands into the shell of the Fc MPC to yield a similarly robust adsorption onto the electrode surface, without the use of SAMs. This supports the hypothesis that multiple ion-pair interactions are central in the irreversibility of adsorption.

Fc Au MPCs have also been shown to greatly enhance the capacitance behavior of highly porous electrodes. When carbon “nanofoams,” are loaded with $\text{Au}_{225}(\text{SC}_6\text{Fc})_{43}$, the Fc redox capacity and the double layer capacity of the intercalated clusters give the nanostructured carbon material supercapacitative properties, making it a potent electrochemical charge storage system.¹⁸³ Some other noteworthy examples of Fc-functionalized Au MPCs are as follows. Chang, et al.¹⁸⁴ synthesized Au MPCs functionalized with terpyridyl Fc and bi-Fc ligands through an Ru^{2+} bridge that interact with the electrode surface; reaction of all three redox species can be observed in CV. Au MPCs functionalized with bipyridinium were found via STM to exhibit differences in electronic conductivity as a function of the charge state of the redox moiety and could therefore serve as nanoscale electronic switches.¹⁸⁵ Au MPCs have additionally been functionalized with biferrocene,¹⁸⁶⁻¹⁸⁹ anthraquinone,¹⁹⁰⁻¹⁹² Fe-carbonyl,¹⁹³ phenothiazine,¹⁹⁴ nitrothiophenolate,^{82,195} and viologen¹⁹⁶ ligands.

Bioconjugation is another type of surface modification giving rise to unique designed electrode surfaces and responses. Bioconjugation of MPCs presents an exciting opportunity for

electrochemical detection of biological molecules, an important part of the future of biosensors and clinical diagnostic tools.

Most bioconjugated MPCs have been synthesized through place exchange reactions. The Maran group¹⁹⁷ studied the electrochemistry of Au₂₅ and Au₁₄₀ nanoparticles modified by ligand place exchanges with thiolated peptides and found that the substitution of electron-withdrawing peptide ligand(s) for phenylethanethiolate caused positive shifts in oxidation potentials by as much as 0.8 V. These shifts were attributed to the orientation of the peptide ligand dipole, which would increase the work function of the metal core if its ligand is electron-withdrawing.

Another class of bioconjugated MPCs acts by binding redox-active biological molecules. The Rotello group¹⁹⁸ showed that flavins can be bound to Au MPCs via noncovalent interactions with aminopyridine surface ligands, and the binding be detected voltammetrically due to binding-induced changes in cluster redox potential. Factors such as charge and length of the receptor ligand and redox state of the flavin influence the cluster redox potentials and binding strengths of flavin to the MPCs.¹⁹⁹ The same group also used trimethylammonium-functionalized Au MPCs to provide a high-affinity binding surface for anionic flavin mononucleotide. The surface charges of mixed monolayer Au MPCs effectively modulated the flavin reduction potential, mimicking flavoenzymes. Binding events were measured voltammetrically using these shifts in redox potential.²⁰⁰ The implications of these studies are that bioconjugation of an MPC surface can be fine-tuned for electrochemical applications such as sensors, and that MPCs could potentially serve as model systems for the study of redox-active enzymes that are otherwise difficult to isolate and manipulate.

Another potential advantage of binding MPCs to redox-active biomolecules is current amplification. The Schiffrin group²⁰¹ used MPCs as a linker between the Cu metal center of

glucose oxidase and the electrode surface, enabling electrochemical detection and study of the metalloenzyme. They were able to quantify the rate of ET between the electrode and the metal center, as well as the pH dependence of the formal potentials of the two processes involved, which are oxidation/reduction of the tyrosyl radical and the $\text{Cu}^{+2/+1}$ redox couple. The metalloenzyme-Au MPC complex showed effective electrocatalysis for O_2 reduction as well. The possibilities for bioconjugated MPCs are evidently quite extensive and will be discussed further in the sensors section.

1.5.2 Catalysis

The electrocatalytic properties of MPCs are highly tunable based on core size, capping ligand, and even the method of anchoring of the clusters onto a support within a device. Numerous opportunities for MPCs to be used as catalysts have arisen and recently the field has pointed towards optimizing MPC catalyst systems by choosing “atomically precise” clusters that best suit the specific application.⁶

In an early work, it was shown¹⁹⁰ that electrocatalytic currents can be enhanced by utilizing MPCs. The electrocatalytic reduction of 1,1-dinitrocyclohexane by electrogenerated anthraquinone radical anions incorporated into the ligand shell of a ~ 2 nm Au MPC was compared to the reactivity of monomeric anthraquinone. ET rates of MPC-bound anthraquinone were nearly identical to the monomeric rates but catalytic current was higher for the anthraquinone-MPC catalysts, which was attributed to its smaller diffusion coefficient and compressed reaction layer. This represents an example of decorating the surface of the MPC with catalytically active moieties, but the core-shell structure of a non-redox ligand modified MPC can be exploited for its electrocatalytic properties as well.

There is an abundance of potential redox catalysis applications of large clusters, aided by the ease of synthesis and fast ET kinetics. As an example, Mirkhalaf and Schiffrin²⁰² studied the electrocatalytic reduction of oxygen, which is important in the design of fuel cells, on films of ~ 7 nm 4-diazoniumdecylbenzene fluoroborate-protected Au MPCs on decylphenyl-coated glassy carbon electrodes. Electrons hop from the electrode surface to the nanocluster metal centers to participate in ET reactions. The choice of a hydrophobic ligand provides an apt environment for stabilization of reactive superoxide and peroxide intermediates.

Towards the trend of utilizing smaller and core-size specific clusters, the Maran group²⁰ has reported the electrocatalytic reduction of benzoyl peroxides by highly monodisperse $\text{Au}_{25}(\text{SC}_2\text{Ph})_{18}$. Recall that the Au_{25} nanoparticle is molecule-like and has a HOMO-LUMO energy gap. The gap improves the charge separation ability of the MPC catalyst, in turn making precise control over the charge state of the MPC very important. Electron donation occurs from the HOMO of the Au_{25} cluster over a distance of approximately the length of the ligand monolayer, suggesting that varying the length of the ligand will also alter the rate of ET. The rate constants of dissociative ET of the peroxides were determined to be on the order of $1 \text{ M}^{-1} \text{ s}^{-1}$ using $\text{Au}_{25}^{0/-1}$ and $\text{Au}_{25}^{+1/0}$ redox couples electron donors, with Au_{25}^{-1} being a slightly more effective electron donor catalyst than the neutral species. The use of freely diffusing MPCs as electrocatalysts represents an improvement over traditional catalytic surfaces (i.e., redox species attached to a metal electrode through SAMs), because reaction encounters can occur with higher frequency in three-dimension space in the solution. Atomically precise $\text{Au}_{25}\text{L}_{18}$ was demonstrated to have good catalytic activity and high selectivity for hydrogenation of α,β -unsaturated ketones and aldehydes to unsaturated alcohols. The electron-deficient Au_{12} shell and electron-rich Au_{13} core structure of Au_{25} is hypothesized to aid the catalysis in two ways. The

low coordination number of outer Au atoms favors adsorption and activation of H₂, while the core activates the C=O bond by donating charge.²⁰³ Another possible factor influencing electrocatalytic capabilities of small clusters is co-adsorption. In a theoretical study, co-adsorption of C₂H₄ onto MPCs of 1-9 Au atoms promoted charge transfers from the cluster to O₂ when otherwise they do not occur favorably.²⁰⁴

In regards to the effect of core size on electrocatalytic activity, a DFT study dissecting the catalytic mechanism of C=O oxidation by “Au₅₅” at low temperatures has revealed how tremendously complex the interplay is between energy levels of MPCs and substrate bond activation.²⁰⁵ Another advantage of using small clusters is achieving better catalyst loading capacities. Larger surface area:volume ratio allows a higher total quantity of active sites as compared to conventional methods with less loading, which is especially important for photocatalytic systems.²⁰⁶ Therefore, small, atomically precise clusters show potential for utility optimizing rate, selectivity, and efficiency of catalysis.

The possibilities for tailoring an MPC catalyst are substantially enlarged by synthesis of bioconjugated MPCs. Prins, et al.,²⁰⁷ for example, found that peptide-Au MPC complexes facilitate trans-esterification rates by more than 2 orders of magnitude. They attribute the catalytic activity to the “multivalent scaffold” nature of the Au MPC, which mimicks an enzyme by bringing the catalyst and substrate into close proximity and creating a favorable local environment. Catalytic applications of MPCs of different core metals have also been studied. Highly monodisperse butylphenyl-protected Pd MPCs were found to be good catalysts for formic acid oxidation, giving 4-fold rate increase over the typical Pd black catalyst.¹⁴⁵ Also, alkyne functionalized Pd MPCs exhibited a 2-fold increase in catalytic activity for oxidation of ethylene glycol over typical Pt/C catalysts.¹⁴⁶ The oxygen reduction catalytic activity of para-substituted

phenol-protected ~2 nm Pt clusters was shown to be highly influenced by the electron-withdrawing ability of the ligand substituent.¹⁴⁹

There has also been progress in characterizing electrocatalysis on single clusters. Observing reaction kinetics at the single particle level has the potential to yield elusive information about catalytic mechanism and to push increases in the sensitivity of measurement capabilities, the basis of many sensor technologies. Novo, Funston, and Mulvaney²⁰⁸ measured the rate of oxidation of ascorbic acid on the surface of single ~50 nm Au nanocrystals using surface plasmon spectroscopy. As mentioned previously, the Bard group²⁰⁹ has observed electrocatalysis at single cluster upon collision with an electrode surface. For Pt MPCs, ET rate, and subsequent catalytic rate, was dependent on the ligand length.^{209,210} The observed current transients accompanying MPC collisions with the electrode could be used to estimate the particle size; larger clusters showed higher catalytic currents for oxidation of hydrazine.²¹¹ Electrocatalysis of NaBH₄ oxidation by single ~14 nm Au MPCs was also measured by the particle-electrode impact method.¹⁴¹

1.5.3 *Electrochemical sensors*

The electroactive properties of MPCs and highly modifiable surfaces present an attractive target for electrochemical sensing platforms. A “sensing platform” has two meanings; it can be the carrier or support of the sensor and/or the mechanism by which sensing occurs. As films, MPCs can provide a physical surface upon which a sensing device can be built. As electroactive species, sensing occurs through detection of analytes via current amplification. The ability to be tailored for selective and sensitive detection of specific analytes, either through core size and/or ligand functionalization, is broad, which can lead to many possibilities for detection of various biomarkers. Three main types of analytes account for the majority of analytes targeted through

MPC sensors: vapors, small redox-active molecules, and biomolecules. The majority of sensing supports involve a film of MPCs either physically adsorbed or chemically linked to a metal electrode. Other examples of platforms include MPC-decorated microspheres²¹² and even kimwipes.²¹³

We begin discussion of specific sensors that utilize MPCs with sensors for the detection of volatile organic compounds (VOCs). The organization is by analyte, noting recent progress for each area and important trends in sensing platforms. Au MPCs represent a good sensing platform for organic vapors because σ_{EL} can be altered reversibly in the presence of adsorbed gases. Flexible carboxylate- Cu^{2+} -linked polymer MPC films swell with organic vapors, altering interparticle distance, decreasing σ_{EL} .⁹³ Xu and Chen²¹⁴ found that core size influences MPC response to organic vapors. They tested a series of single hexanethiolate-protected Au MPCs of various core sizes for changes in electronic conductivity in the presence of hexane, toluene, THF, etc. using STM and found 4.9 nm MPCs gave the best sensitivity in measurement at room temperature. Larger and smaller clusters did not exhibit as discernable changes in electronic conductivity, due to reduced or increased Coulomb blockade effects, respectively.

A trend in sensor technology is miniaturization. An early report from Shao and Mirkin²¹⁵ established the potential of extremely small electrodes as sensor platforms. The advantage of micro and even nanoscale level sensing platforms include precise position resolution and low detection and quantification limits.²¹⁵ Merging the research areas of micro- and nanoelectrodes with MPCs has led to some interesting advances in analyte detection, especially of organic vapors. There is a class of organic vapor sensors called chemiresistors that employ MPC films atop microband interdigitated array (IDA) electrodes called. Wohltjen and Snow²¹⁶ were the pioneers of this area, first utilizing films of 2 nm octanethiol-protected Au MPCs on IDA

electrodes for detection and quantification of VOCs. In another early work in the development of chemiresistors, the Zellers group²¹⁷ fabricated devices made from IDAs with 50 pairs of electrodes, gaps of 7-30 μm , and either ~ 8 nm octanethiolate or ~ 6 nm phenylC₂ thiolate-protected Au MPC films (Figure 1.11, left), exposed the film to vapors, and measured the resistance of the film between the two sets of fingers. The limits of detections achieved were between 0.1-10 ppb depending on the specific analyte and gave an improvement over surface acoustic wave (SAW) sensors. They also saw a ligand effect, as C₈ MPC films were slightly more sensitive than the phenyl-C₂ films.²¹⁷ More recently, they derived a model to predict the response of chemiresistors taking into various factors such as core size and ligand of MPCs, vapor-film partition coefficients, and analyte densities.²¹⁸ The importance of ET characterization and utilizing clusters of definite core and ligand compositions again comes into play.

Chemiresistors have also been adapted for sensing of organics dissolved in aqueous solutions, a possible test for safe drinking water. A problem associated with solution measurements is the interference from double layer charging current (large C_{DL}) on the voltammetric response. Wieczorek, et al.²¹⁹ found that by inkjet printing a thin film of hexanethiolate-protected Au MPCs onto 5 μm IDA electrodes, the charging current was reduced significantly, allowing highly sensitive measurements via electrochemical impedance, ~ 0.1 ppm for toluene, as an example.

In a departure from IDA electrodes, the Zamborini group²²⁰ designed a method for printing micro-contact patterned films of 1.6 nm hexanethiolate-protected Au MPCs across two Au electrodes separated by a 1 μm gap (Figure 1.11, right). Upon heating and crosslinking with dithiol vapor, the films become like flexible wires and can be lifted, transported, and reattached to new electrodes for multiple measurements, achieving $S/N = 22$. While IDA electrodes are

small, they are typically not low cost or widely available. These workers found that film flexibility was the key for sensitivity to organic vapors to allow for swelling which alters the electronic conductivity. They also stressed the importance of high portability, high throughput, and simultaneous detection of multiple analytes in the future of sensor development. The group has also had success with sensing using Au MPC films containing tetraoctylammonium as the surfactant, which are more stable over time and more highly sensitive to VOCs than thiolate-protected MPCs, an improvement from ~100 to 10 ppm. Another interesting finding was that the sensitivity of the MPC sensor also depended on the metal content of the core; doping the Au core with Ag lowers the sensitivity.¹⁷⁶

Biomolecules are important target analytes for many reasons, with most relating back to the primary goal of disease diagnosis/prognosis. Sensors utilizing the ET properties of Au MPCs have been designed for small redox-active molecules important in biological systems and both redox active and inactive biomolecules. These sensors are sometimes in combination with another redox-active label for current amplification. There is also a large class of sensors for analytes not necessarily limited to biological molecules made using bioconjugated MPCs that will be discussed in the subsequent section. A major challenge in sensing is to overcome interference from other analytes in complex matrices such as human serum, and electrochemical detection could yield improvements in selectivity.

Here are a few examples of detection of small redox-active molecules that are highly relevant in living things. Lee, et al.²²¹ was able to detect ascorbic acid and uric acid down to concentrations of 70 nM by enlisting Au₂₅ in a sol-gel framework (Figure 1.12 a) as an electrocatalyst. As discussed previously in the electrocatalysis section, the electron rich core and electron poor shell of Au₂₅ allows it to function as a redox mediator, separating charge and thus

lowering the oxidation potential of the analytes. Because Au₂₅ is not only a good redox mediator, but a fairly conductive species, there is fast ET between the analyte through the sol-gel film to the electrode surface. Good current response is obtained, with sensitivities around 1.5 uA/uM (Figure 1.12 b and c). Many MPC sensors utilize their electrocatalytic properties, blurring the line between electrocatalytic applications of Au MPCs and sensing applications.

Another biologically-relevant small molecule target is the free radical. Oxidative stress, the imbalance of reactive oxygen species (ROS), including superoxide anions ($\bullet\text{O}^{2-}$), hydroxyl radical ($\bullet\text{HO}$), singlet oxygen ($^1\text{O}_2$), and hydrogen peroxide (H_2O_2), can occur as a response to injury and in the progression of some diseases, like cancer, making monitoring of the concentrations of these species in ill patients very important. Tian, et al.²²² designed an electrochemical detection method for $\bullet\text{HO}$ using a Fc-labelled Au MPC-modified electrode. Typically, electron spin resonance is used to monitor $\bullet\text{HO}$, but an electrochemical method of detection such as this could conceivably be adapted to *in vivo* monitoring of ROS with sufficient miniaturization of the sensor and cost. An LOD of 0.37 nM and linear range of 5 – 45 nM were achieved for $\bullet\text{HO}$ released from living cells, signifying some promise of this sensing platform over traditional methods.

The development of sensors that do not require extensive pretreatment of blood samples is also highly desirable. Concentrations of lysine, an amino acid, in the body are often used to determine the nutrition level of an individual, as in a sensor that utilizes citrate-capped Au MPCs on a carbon nanotube-decorated Au electrode surface.²²³ A layer of lysine oxidase is physisorbed onto the surface of the Au MPCs and carbon nanotubes. The other purpose of the Au MPCs is to relay the charge transfer from the lysine oxidase to the electrode surface during cyclic voltammetry and electrochemical impedance measurements. These sensors achieved good

quantification of ~ 200 uM lysine in human serum samples (+/- 5 uM) and were washable and reusable.

Larger biomolecules are also important target analytes but present substantial challenges due to their low concentrations. A relatively complex immunosensor for carcinoembryonic antigen (CEA) was designed utilizing the increased HRP-electrocatalyzed reduction of hydrogen peroxide, which was locally generated by the glucose oxidase. The large surface area of the dendrimer is advantageous for immobilizing the CEA, aiding in the low concentration problem. The encapsulation of Au MPCs in the interior of the dendrimer accelerated the ET between the enzymes and the electrode surface, enhancing the immunosensor's response. The limit of quantification in human serum samples was around 10 pg/mL, much lower than the typical enzyme-linked immunosorbent assay (ELISA) method.²²⁴ ELISA methods, which are typically used for detection of antigens, involve many wash steps, and electrochemical sensing platforms could conceivably evolve into the point of care diagnostics area, with further miniaturization and reduction of cost.

A specific category of protein sensing, termed protein monolayer electrochemistry (PME) by the Leopold group, allows for measuring ET rates of redox active proteins via current amplification. Steric bulkiness and low biological concentrations of certain redox active proteins make studying their ET kinetics difficult due to low sensitivity. Using dithiol linked films of Au₂₂₅ to immobilize cytochrome C²²⁵ and azurin (Az)^{226,227} at the electrode, ET rates for each of these proteins could be quantified via cyclic voltammetry. The hydrophilic dithiol linked MPC film creates a uniform surface for effective binding of the protein and facilitates rapid ET to/from the electrode surface, thus amplifying signal. Also, recall that dithiol linkages between clusters increase the electronic conductivity of the film. Multilayer film structure (i.e. dropcast) is

preferred over SAMs because it results in more uniform voltammetric peaks and more surface coverage by the protein of interest. In addition, the rate of ET calculated for proteins adhered to film assemblies is not necessarily distance dependent as is with attachment through SAMs.²²⁷ Pulse techniques and electrochemical impedance were also utilized to quantify the ET characteristics of azurin to minimize the influence of charging current in ET rate measurements and better estimate surface coverage.²²⁸

Lastly, we delve into electrochemical sensors based on bioconjugated MPCs, grouping these applications by their type of bioconjugation. It is important to note that while the target analyte for a bioconjugated MPC biosensor is not necessarily a biological molecule, that is most often the case, and detection is mostly indirect, measuring signal from another redox species. The versatility of syntheses of MPCs modified with biomolecules- neurotransmitters, nucleic acids, antibodies, enzymes, etc. gives a wide realm of possibilities for target analytes and sensor designs. This has created an abundance of publications in the recent literature describing advances in sensing technology. Some key studies will be highlighted.

Beginning with Au MPCs modified with small biomolecules, Liu, et al.²²⁹ recently synthesized dopamine-capped Au MPCs and incorporated them into a sandwich-type sensor for the capture of glycoproteins with avidin and prostate specific antigen as model analytes. Sandwich-type sensors are based on specific affinity of the sensor to the target (dopamine to glycoprotein in this case) and are thus highly selective. “Dual amplification” was achieved by decorating the surface of the electrode with 4-mercaptophenylboronic acid-capped Au MPCs, which provided multiple binding sites per cluster for the dopamine-capped Au MPCs and more surface area for analyte binding. The sensitivity of this type of sensor was outstanding, with LODs below the pM level.

As an example of an aptasensor, a specific type of sensor where a DNA sequence is the target analyte, Pt MPCs bioconjugated with short DNA sequences complementary to the target analyte sequence allow indirect target detection via the electrocatalytic reduction of H_2O_2 . Thrombin bound to its aptamer was also detected by this method using thrombin aptamer-functionalized Pt MPCs. MPCs are ideal for use in sensors due to fast ET kinetics, electrocatalytic activity, and functionalizable surfaces; this sensor makes use of all three. The limits of detection of thrombin were 100-fold better than traditional aptasensors not utilizing MPCs, demonstrating their significant role in the sensing platform.¹⁵²

MPCs functionalized with large biomolecules including proteins, enzymes, and antibodies (immunosensors) are also abundant in the literature. A TiO_2 nanotube array was decorated with antibody-labeled Au MPCs to allow for binding with a target analyte and amperometric detection. Typically, sensors must achieve detection limits of at least ng/mL to be a viable sensing platform for low-abundance proteins, and this sensor could lead to detection limits as low as 0.01 ng/mL. Similar to the vast improvement in sensitivity for the chemiresistor that IDA electrodes made, miniaturization of electrodes into high aspect ratio arrays for this sensor led to enhanced electrochemical detection in comparison to flat electrode surfaces by ten-fold.²³⁰

Progress towards the specific binding of antibodies to the surface of atomically precise MPCs has been made as well. Kornberg, et al.²³¹ designed a method for controlled addition of MPCs to proteins at sulfhydryl groups. In addition to use of a single core size of MPCs to optimize performance, controlling the reactivity of sulfhydryl groups on target analytes minimizes interference from functional groups on other species in complex matrices. Exactly four glutathione-capped Au_{71} MPCs are added to the single chain Fv antibody fragment. This

was accomplished by oxidation of the MPC using permanganate for addition of Au₇₁ followed by reduction by tiopronin for deactivation to stop further addition of Au₇₁.

Perhaps practical implementation of highly sensitive MPC biosensors could be facilitated by moving towards a cheaper and more automated system. A study utilizing low-cost and highly automated screen printed carbon electrodes examined the core size effect on voltammetric response for sterically-hindered antibody-Au MPCs, finding that a large core size yields higher current due to reduced Brownian motion.²³² The Polsky group conducted a study of sensing target DNA with streptavidin-Au MPCs using single-use thick film carbon electrodes.²³³ MPC-based electrochemical sensors and biosensors make a strong case as the forefront of analyte detection research due to their synthetic diversity, selectivity, low LODs/LOQs, rapid analysis times, and potential for miniaturization. However, challenges remain. They include issues of stability, which is helped somewhat by the addition of electrolyte to and/or crosslinking of films, and high cost, making them relatively impractical for current use in industry and clinical settings at this point in time. Inexpensive, easy to use electrode materials are going to be paramount for the transition of these technologies from the bench to bedside.

1.6 Introduction to Iridium Oxide Nanoparticles

Switching gears to a type of nanoparticle that is much less fully characterized from an analytical chemistry perspective than gold, ~ 1.6 nm diameter iridium oxide nanoparticles (IrOx NPs) are an interesting material because they catalyze water oxidation at relatively low overpotentials (~0.25 V at 0.5 mA/cm² regardless of pH with 100% current efficiency).²³⁴ They are the first example of freely diffusing, electroactive nanoparticles for electrocatalysis.²³⁵ Furthermore, mesoporous films of IrOx NPs can easily be made by applying a potential sufficient to initiate water oxidation to a Au, Pt, glassy carbon, or ITO electrode.²³⁴ This

process, called electroflocculation, proceeds through an induction period during which a significant amount of charge is passed but no nanoparticles deposit.²³⁶ It is thought that proton release accompanying nanoparticle oxidation triggers subsequent precipitation of the nanoparticles. Chemical flocculation by the addition of a chemical oxidant such as Ce (IV) is also possible. CVs of the electroflocculated IrOx at different pH as well as AFM and SEM images are presented in Figure 1.13.

Electron transfer kinetics of IrOx for the first time were quantified in SAMs of carboxylated *n*-alkanethiolates.²³⁷ Apparent electron transfer rate constants for *n* = 12 and 16 are 9.8 and 0.12 s⁻¹. The water oxidation overpotential was also found to shift to more positive potentials with increasing SAMs length. These series of experiments also suggested participation of all of the iridium redox sites in the nanoparticle (~130). All iridium species were shown to be redox-active in freely diffusion nanoparticles in solution²³⁸ as well.

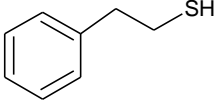
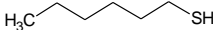
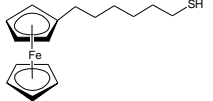
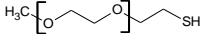
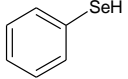
While their full catalytic capabilities have likely not yet been fully unlocked, IrOx NPs coated on glassy carbon have also been shown to catalyze the ORR²³⁹ and reduction of iodate and periodate.²⁴⁰ A recent study probed the mechanism of IrOx NP catalysis of the oxygen evolution reaction (OER).²⁴¹ Ambient-pressure x-ray photoelectron spectroscopy performed *in situ* under OER conditions revealed Ir changes oxidation state from Ir^{IV} to Ir^V predominantly at the catalyst surface. A decrease in surface hydroxide is simultaneously observed, suggesting IrOx NP-mediated OER occurs through an OOH-mediated deprotonation mechanism. In another interesting experiment, single IrOx nanoparticle collisions with a Pt UME could be observed due to current enhancement of the water oxidation reaction by electrocatalytic redox cycling.¹⁴²

Future directions of research on IrOx NPs include examining their sensing roles or catalytic properties in freely diffusion solution and in films towards oxidation of liquid and/or

solar fuels such as formic acid. Moreover, observing electrocatalysis *in situ* through high-resolution x-ray spectroscopies in combination with electrochemical methods or even at the single nanoparticle level has potential to yield high-sensitivity information pertinent to mechanistic understanding. Finally, improving monodispersity to achieve discrete chemical formulas could enable studies akin to those of gold nanoparticles that examine how very specific analytical properties such as core size affect electron transfer rate between nanoparticles.

1.7 Tables and figures

Table 1.1. Known MPC nanoparticles and their ligands.

Core and ligand	 -SC ₂ H ₄ Ph	 -SC ₆ H ₁₃	 -SRFc	 -SPEG	 -SeR
Au ₂₅	Synthesis, MS, voltammetry ^{242,243} Crystal structure ⁹	Synthesis, voltammetry ⁷⁹		Synthesis, voltammetry ^{54,80}	Synthesis, MS ²⁴⁴⁻²⁴⁶
Au ₃₈	Synthesis ²⁴⁷ Crystal structure ⁴¹	Synthesis ^{17,67} MS ²⁴⁸			
Au ₆₇	Synthesis, MS, voltammetry ⁶⁸	Synthesis, MS, voltammetry ⁶⁸			
Au ₇₅		Synthesis, MS, voltammetry ⁶⁹			
Au ₁₄₄	Synthesis, MS ⁴³	Synthesis, MS, voltammetry ^{70,118,249}	Synthesis, voltammetry ¹⁷⁷		
Au ₂₂₅		Synthesis, voltammetry ⁵¹	Synthesis, voltammetry ^{57,179}		

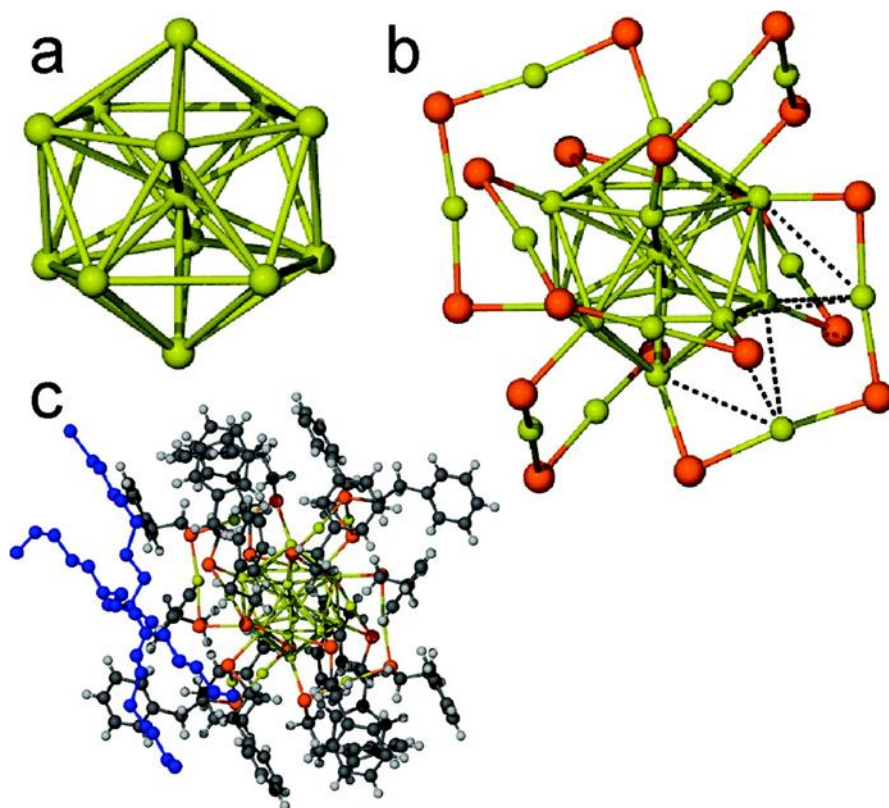


Figure 1.1. Breakdown of X-ray crystal structure of $[\text{TOA}^+][\text{Au}_{25}(\text{SCH}_2\text{CH}_2\text{Ph})_{18}^-]$ as seen from $[001]$. (a) Arrangement of the Au_{13} core with 12 atoms on the vertices of an icosahedron and one in the center. (b) Depiction of gold and sulfur atoms, showing six orthogonal $-\text{Au}_2(\text{SCH}_2\text{CH}_2\text{Ph})_3-$ “staples” surrounding the Au_{13} core (two examples of possible aurophilic bonding shown as dashed lines). (c) $[\text{TOA}^+][\text{Au}_{25}(\text{SCH}_2\text{CH}_2\text{Ph})_{18}^-]$ structure with the ligands and TOA⁺ cation (depicted in blue) (Legend: Gold = yellow; Sulfur = orange; Carbon = gray; Hydrogen = off-white; the TOA⁺ counterion is over two positions with one removed for clarity). Reprinted with permission from Heaven, M. W.; Dass, A.; White, P. S.; Holt, K. M.; Murray, R. W. *J Am Chem Soc* **2008**, *130*, 3754. Copyright 2008 American Chemical Society.

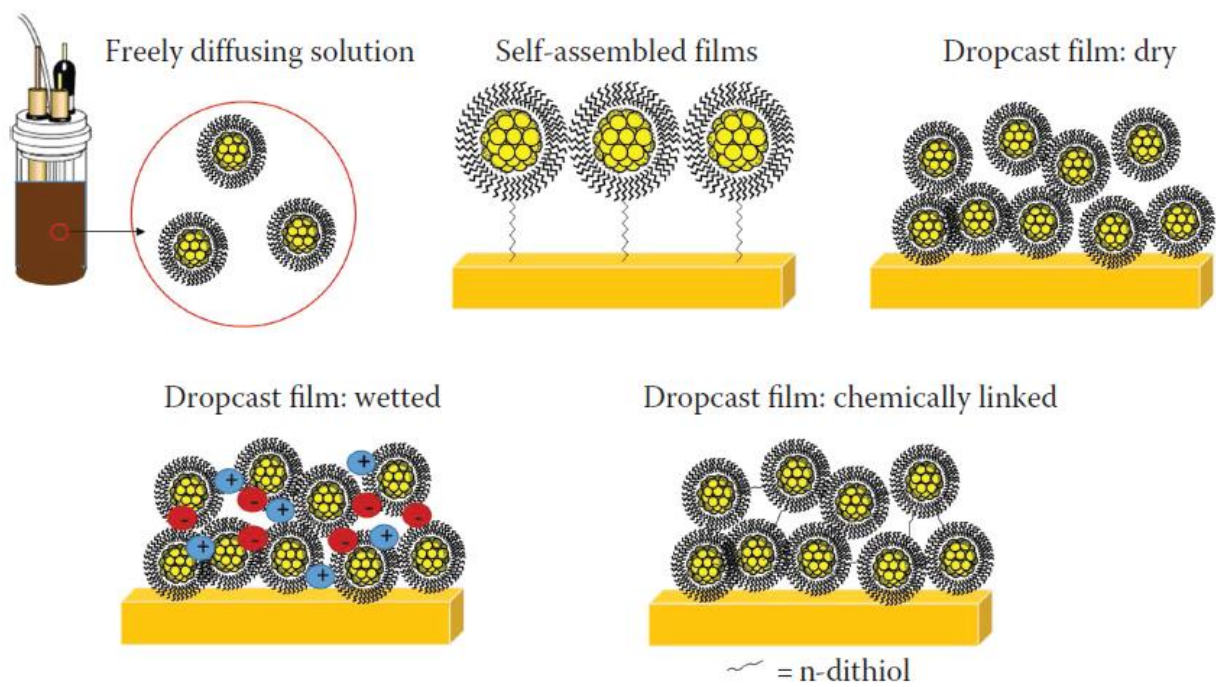


Figure 1.2. Different physical states of monolayer-protected Au nanoparticles.

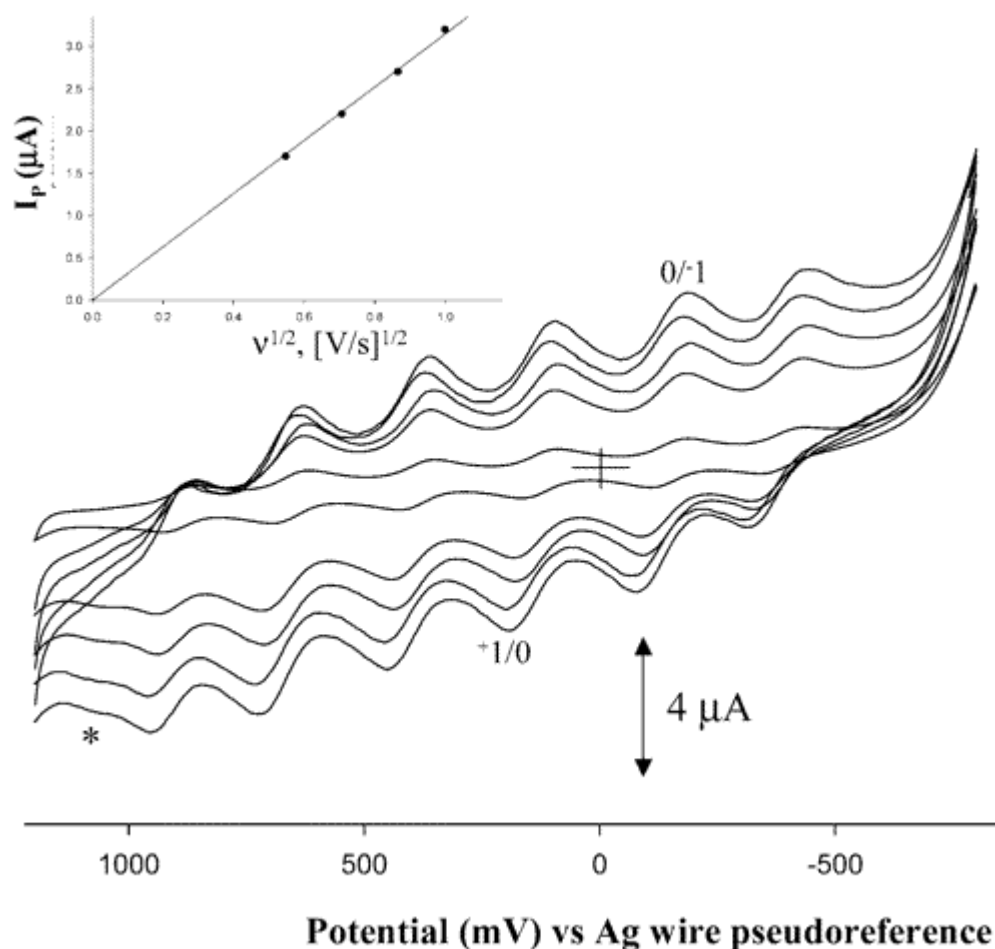


Figure 1.3. Cyclic voltammetry of Au₁₄₄ at a 0.02 cm² Pt working electrode, of 200 μM annealed EtOH soluble C₆ MPCs (annealed with C₁₆SH thiol) in 0.1M Bu₄NPF₆/CH₂Cl₂; voltammograms at potential sweep rates (v) of 50, 300, 500, 700, and 1000 mV/s, potentials vs. Ag wire pseudo-reference, Pt flag counter electrode. Inset shows variation of peak current with $v^{1/2}$ for the MPC^{0/+1} wave. The solution was not degassed; the rising current at negative potential is oxygen reduction. Reprinted with permission from Hicks, J. F.; Miles, D. T.; Murray, R. W. *J Am Chem Soc* **2002**, 124, 13322. Copyright 2002 American Chemical Society.

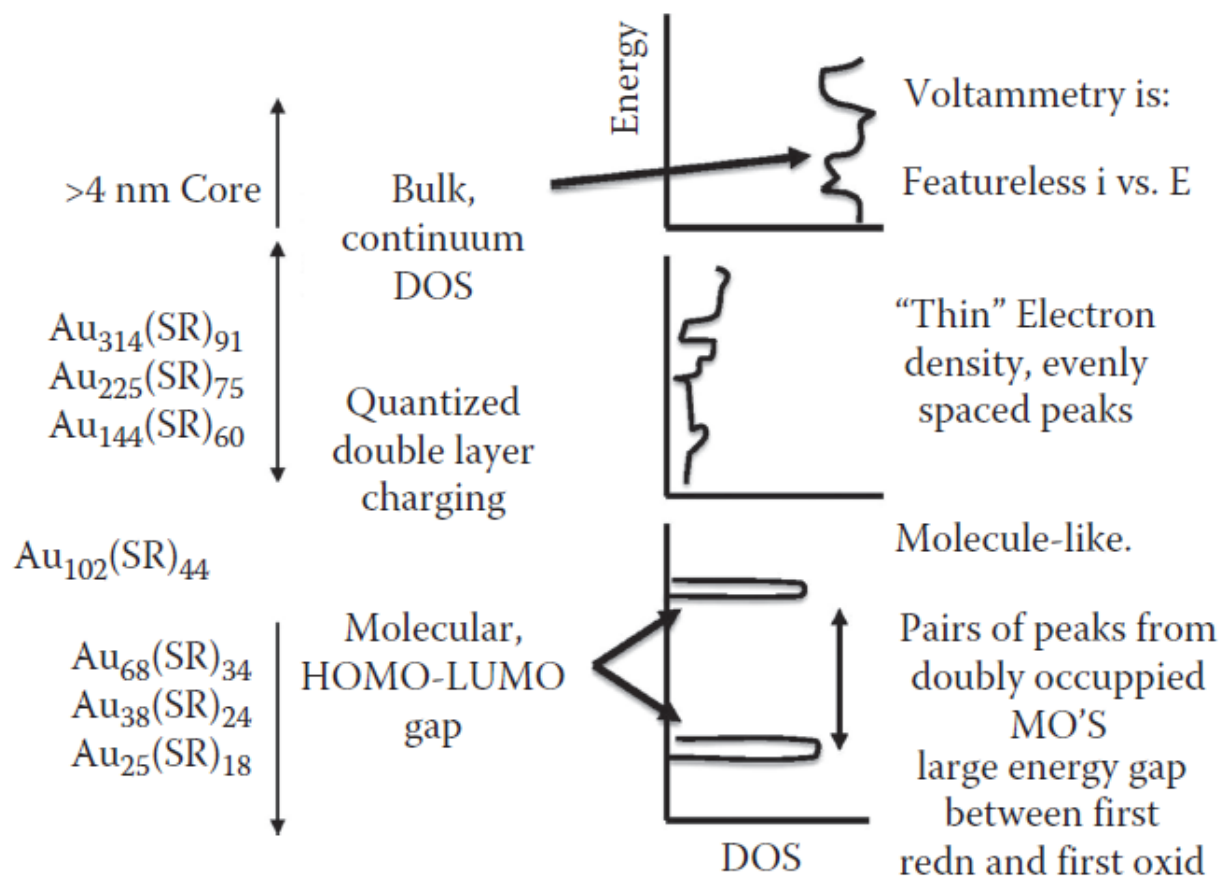


Figure 1.4. General classification of MPC voltammetries.

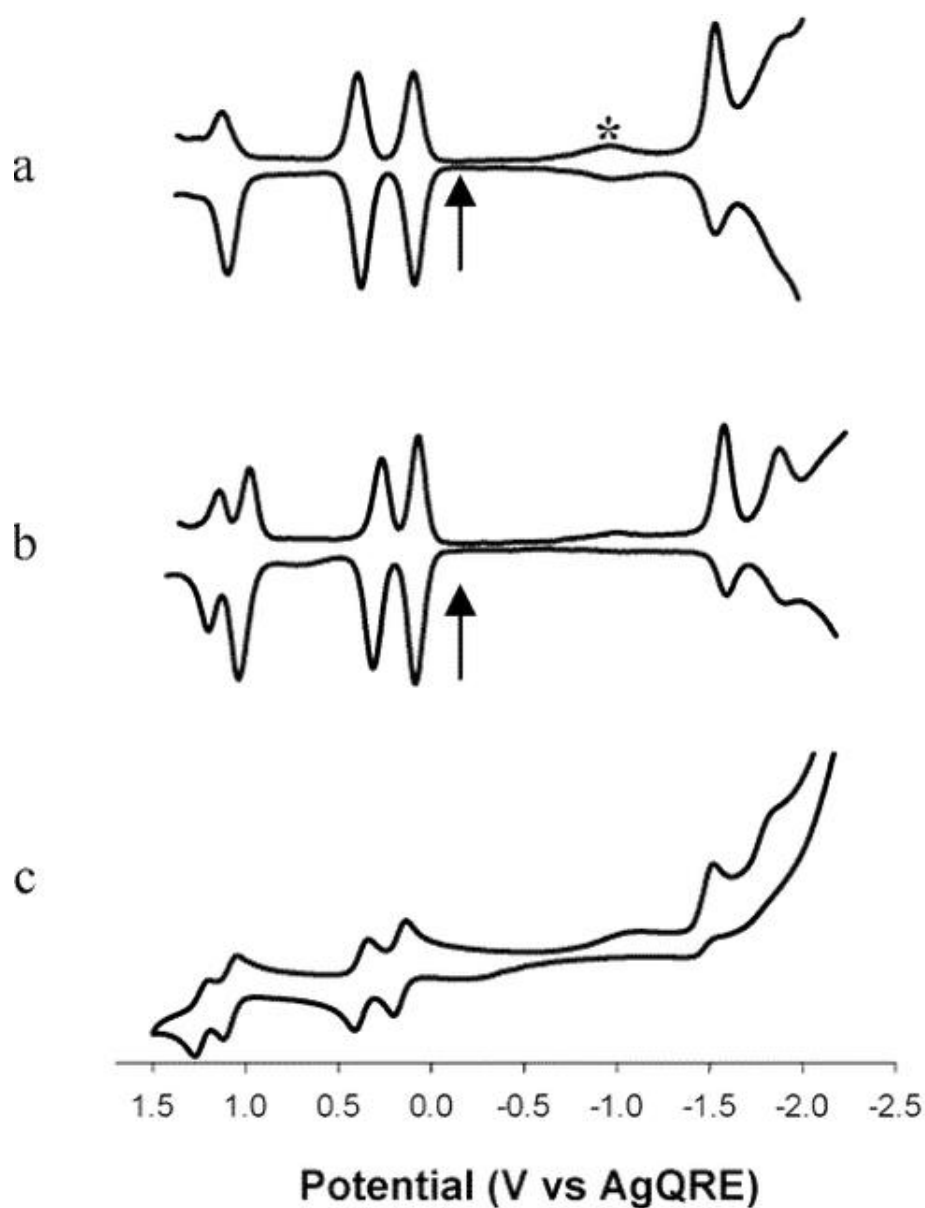


Figure 1.5. (a) 25°C and (b) -70°C differential pulse voltammograms (DPVs) at 0.02 V/s , and (c) -70°C cyclic voltammogram (0.1 V/s) of $\text{Au}_{25}(\text{PhC}_2\text{S})_{24}$ in $0.1 \text{ M Bu}_4\text{NPF}_6$ in degassed CH_2Cl_2 at 0.4 mm diameter Pt working, Ag wire quasireference (AgQRE), and Pt wire counter electrode. Arrows indicate solution rest potentials, and * indicates wave for incompletely removed O_2 , which varied. Reprinted with permission from Lee, D.; Donkers, R. L.; Wang, G.; Harper, A. S.; Murray, R. W. *J Am Chem Soc* **2004**, *126*, 6193. Copyright 2004 American Chemical Society.

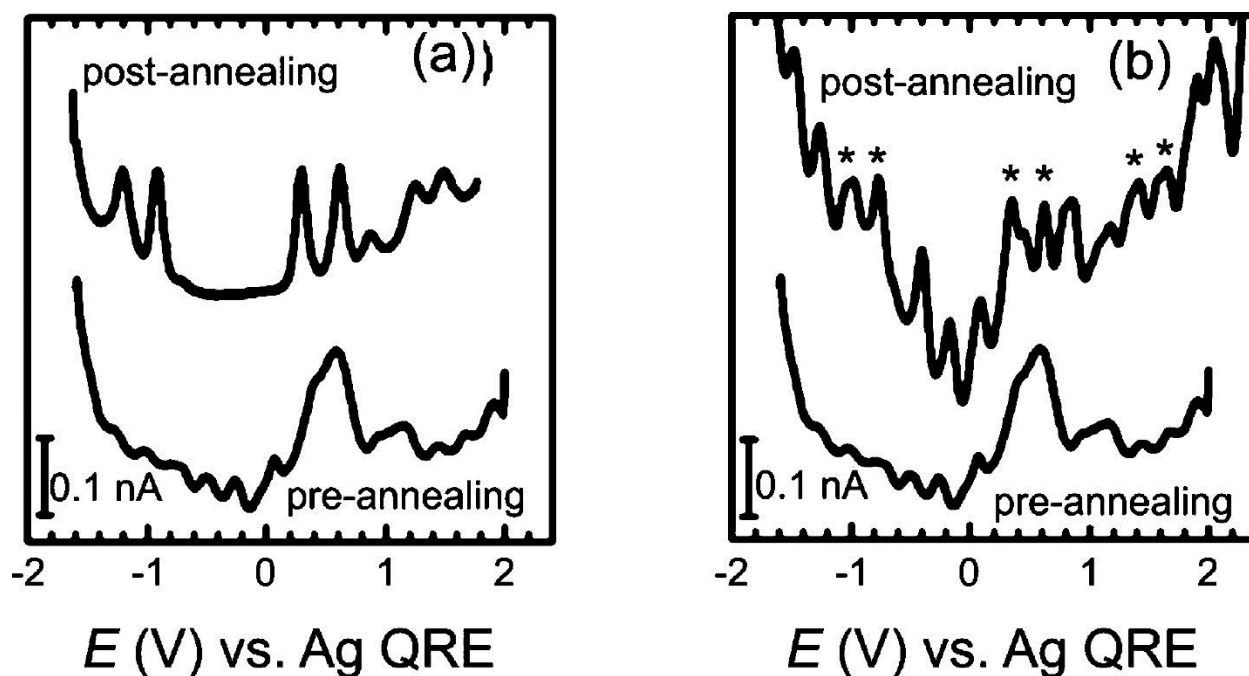


Figure 1.6. Microelectrode SWVs for particles postannealing (upper traces) in either (a) DCE or (b) CB compared with the response preannealing (lower trace in both plots). All SWVs were recorded in DCE solution containing 10 mM base electrolyte. In (b), the peaks ascribable to Au₃₈ are marked with asterisks. Reprinted with permission from Toikkanen, O.; Carlsson, S.; Dass, A.; Rönnholm, G.; Kalkkinen, N.; Quinn, B. M. *The Journal of Physical Chemistry Letters* **2010**, *1*, 32. Copyright 2010 American Chemical Society.

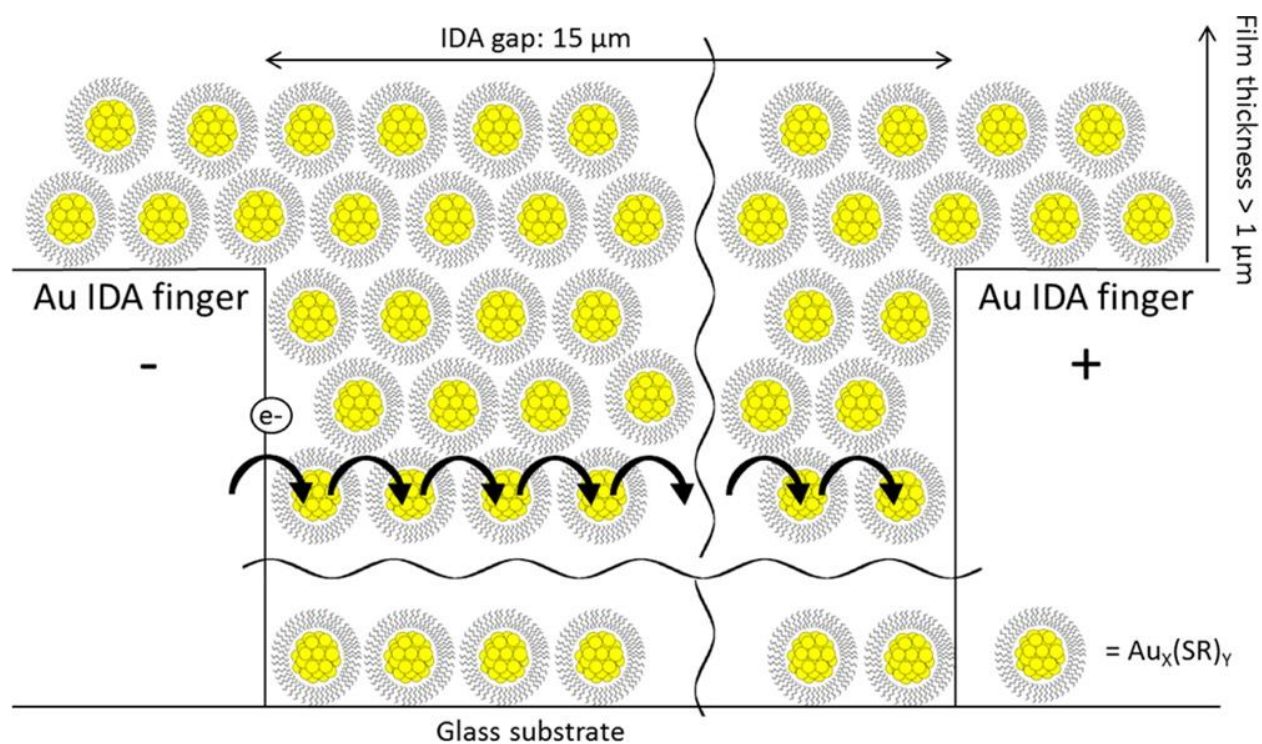


Figure 1.7. Cartoon of electron hopping conductivity in mixed-valent Au MPC film on an IDA electrode. Reprinted with permission from Carducci, T. M.; Murray, R. W. *J Am Chem Soc* **2013**, *135*, 11351. Copyright 2013 American Chemical Society.

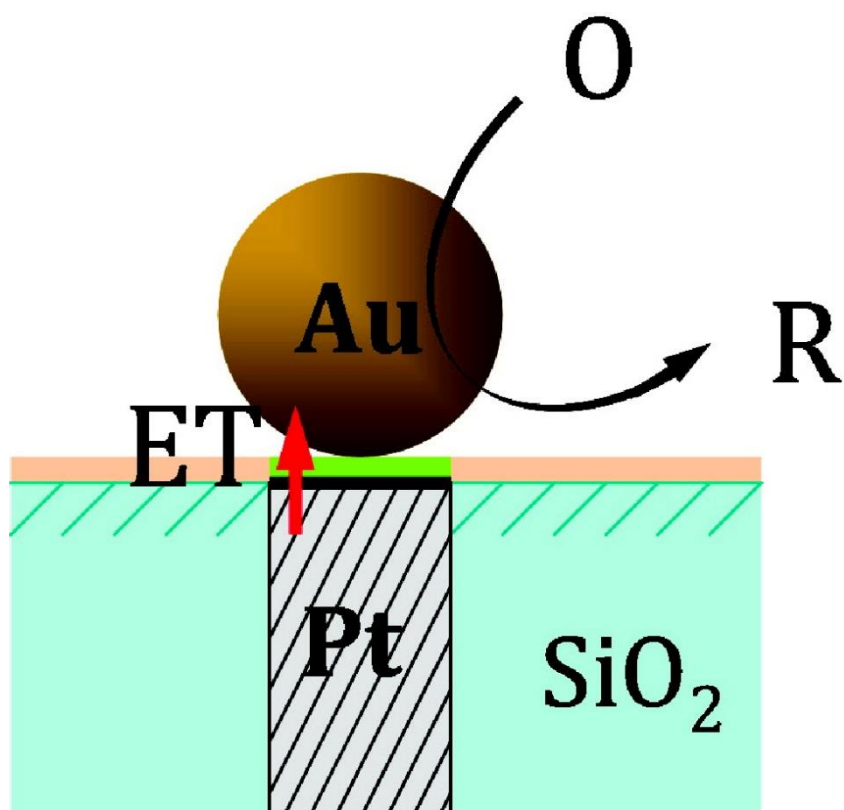


Figure 1.8. Schematic drawing of a Au SNPE. Reprinted with permission from Li, Y.; Cox, J. T.; Zhang, B. *Journal of the American Chemical Society* **2010**, 132, 3047. Copyright 2010 American Chemical Society.

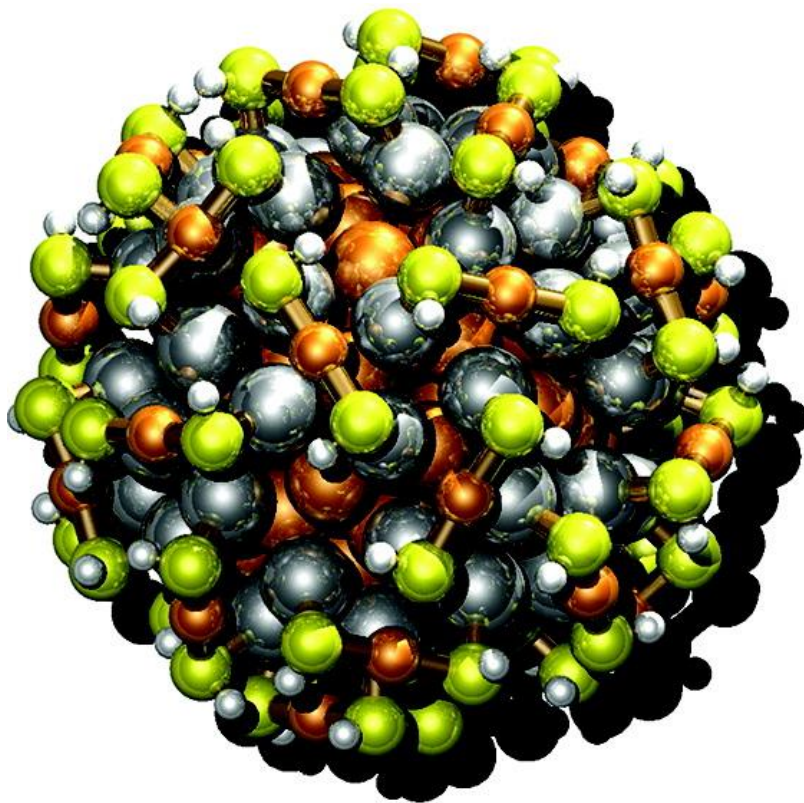


Figure 1.9. Optimized structure of cluster of composition $\text{Au}_{54}\text{Ag}_{60}(\text{RSAuSR})_{30}$. Brown = gold; shiny gray = silver; yellow = sulfur. The hydrogen atoms are not shown for clarity. Reprinted with permission from Malola, S. and Hakkinen, H., *J. Phys. Chem. Lett.*, 2, 2316, 2011. Copyright 2011 American Chemical Society.

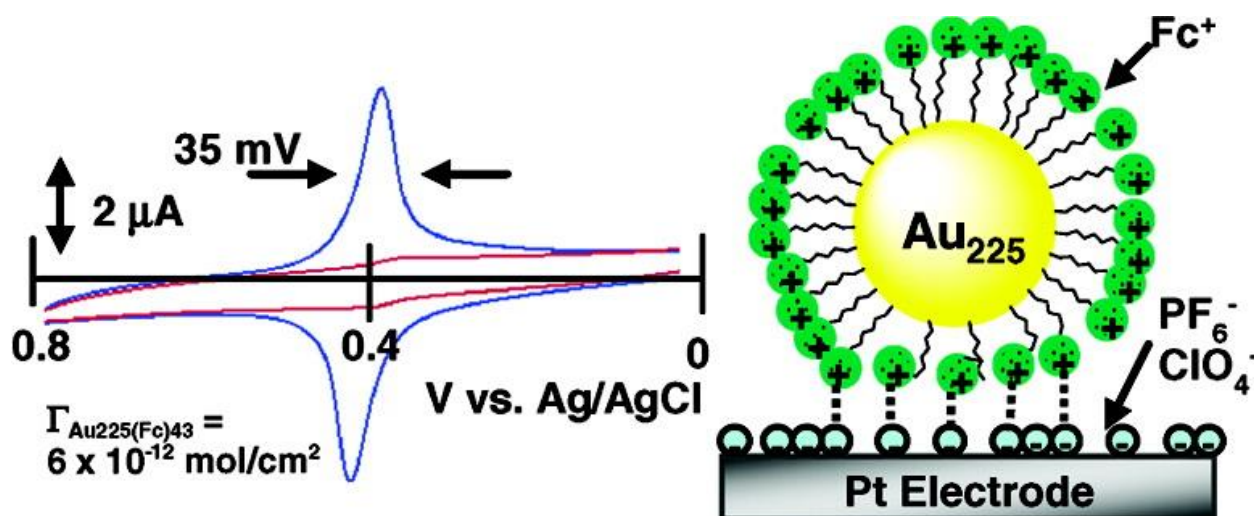


Figure 1.10. (A) Cartoon of ion-induced adsorption, where ferrocenium cations on the MPC form ion-pair bridges with electrolyte anions specifically adsorbed to the Pt electrode. It can be imagined that the ligand shell may become deformed to form ion-pair bridges of similar dimensions. Formation of ion-pair bridges stabilizes successive ion-pair bridges and can cause a shift in Fc/Fc^+ formal potentials. (B) Cyclic voltammetry (blue, 0.20 V s^{-1}) of an adsorbed $\text{Au}_{225}(\text{SC}_6\text{Fc})_{43}$ film formed on a clean Pt electrode from 0.1 mM MPC , $1.0 \text{ M Bu}_4\text{NPF}_6/\text{CH}_2\text{Cl}_2$ solution and transferred to an MPC-free $1.0 \text{ M Bu}_4\text{NPF}_6/\text{CH}_2\text{Cl}_2$ solution. The blue curve is cyclic voltammetry (0.20 V s^{-1}) of an identically treated Pt electrode, except that the Pt electrode was first coated with a dodecanethiolate self-assembled monolayer (SAM). Reprinted with permission from Stiles, R. L.; Balasubramanian, R.; Feldberg, S. W.; Murray, R. W. *J Am Chem Soc* **2008**, *130*, 1856. Copyright 2008 American Chemical Society.

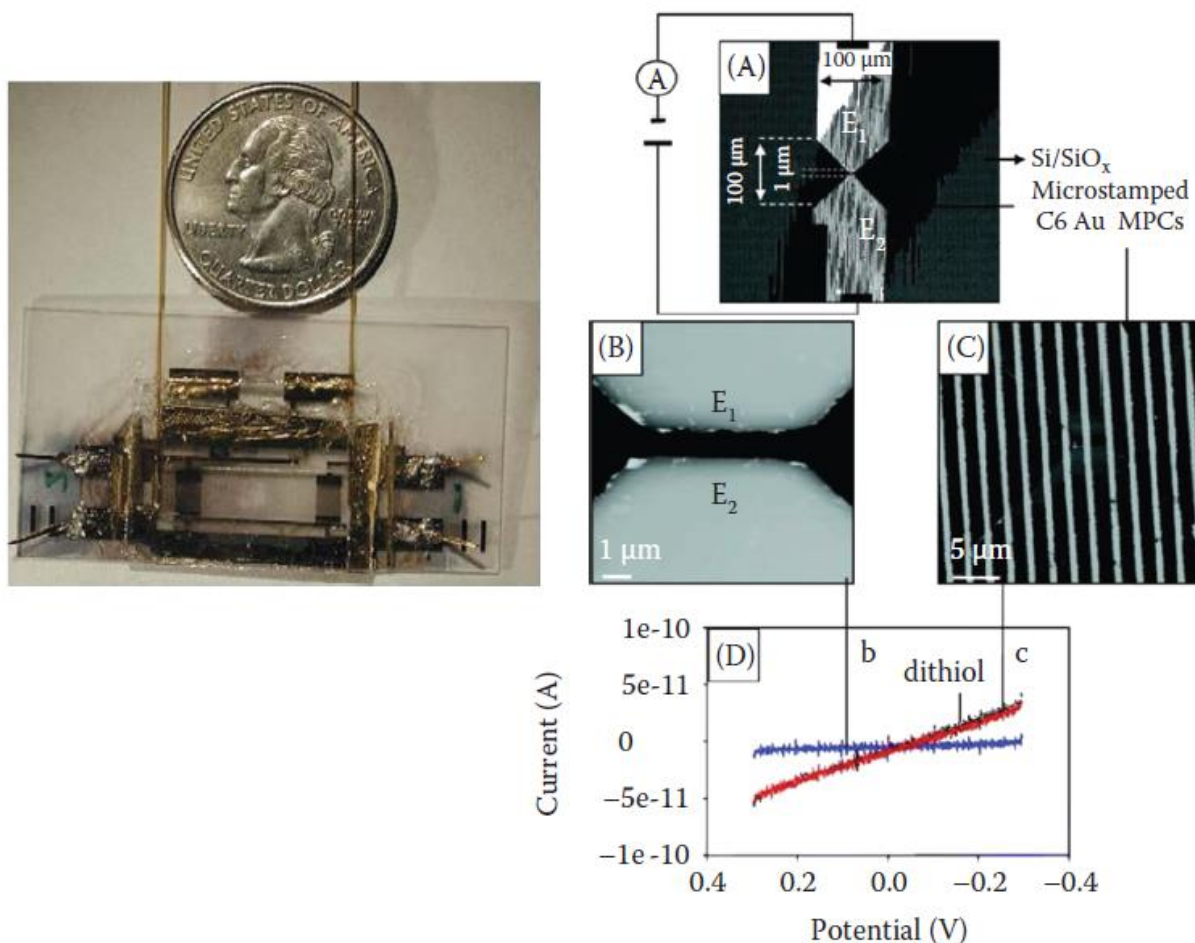


Figure 1.11. Left: Dual-chemiresistor array housed in a 60 μL detector cell. Reproduced with permission from Cai, Q.-Y. and Zellers, E.T., *Anal. Chem.*, 74, 3533, 2002. Copyright 2002 American Chemical Society. Right: (A) Optical image of microscale lines of C6 Au MPCs stamped across two Au electrodes separated by a 1 μm gap at the shortest point. AFM images of the electrodes (B) before and (C) after stamping the C6 Au MPCs across them. (D) I - V curves of the (B, blue) bare electrodes, (C, red) electrodes bridged with stamped C6 Au MPCs, and (dithiol, green) electrodes bridged with C6 Au MPCs and exposed to hexanedithiol for 30 min. Reproduced with permission from Ibanez, F.J. et al., *Anal. Chem.*, 78, 753, 2006. Copyright American Chemical Society 2006.

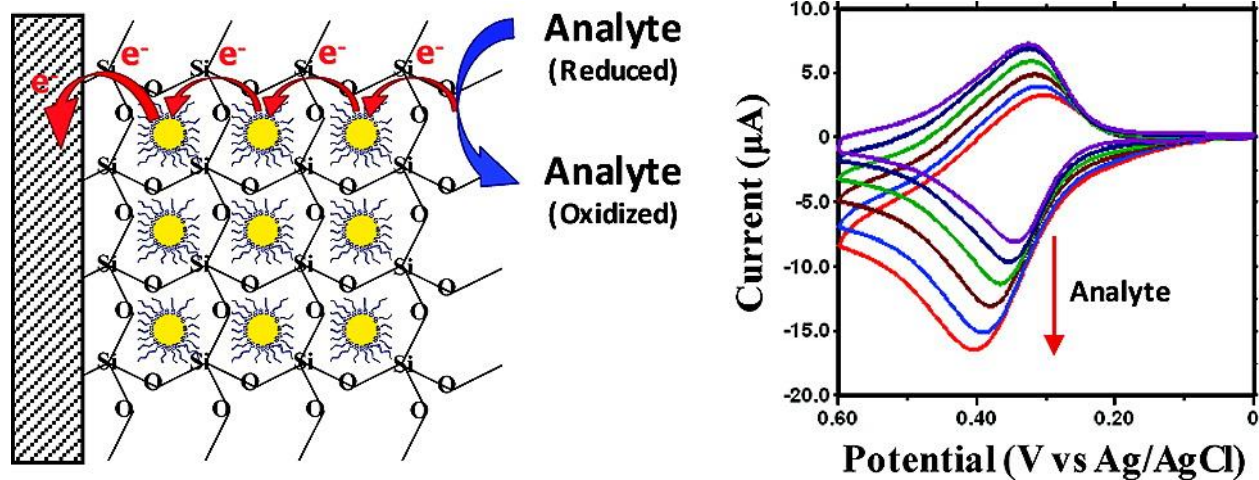


Figure 1.12. Left: Mechanism depicting the mediated electrocatalytic oxidation and ensuing electron transport across entrapped Au_{25} in the sol-gel framework (Au_{25}SGE). Right: Voltammograms showing the electrocatalytic oxidation of ascorbic acid or uric acid in 0.1 M KCl at 20 mV s^{-1} . Reproduced with permission from Kumar, S.S. et al., *Anal. Chem.* 83, 3244, 2011. Copyright 2011 American Chemical Society.

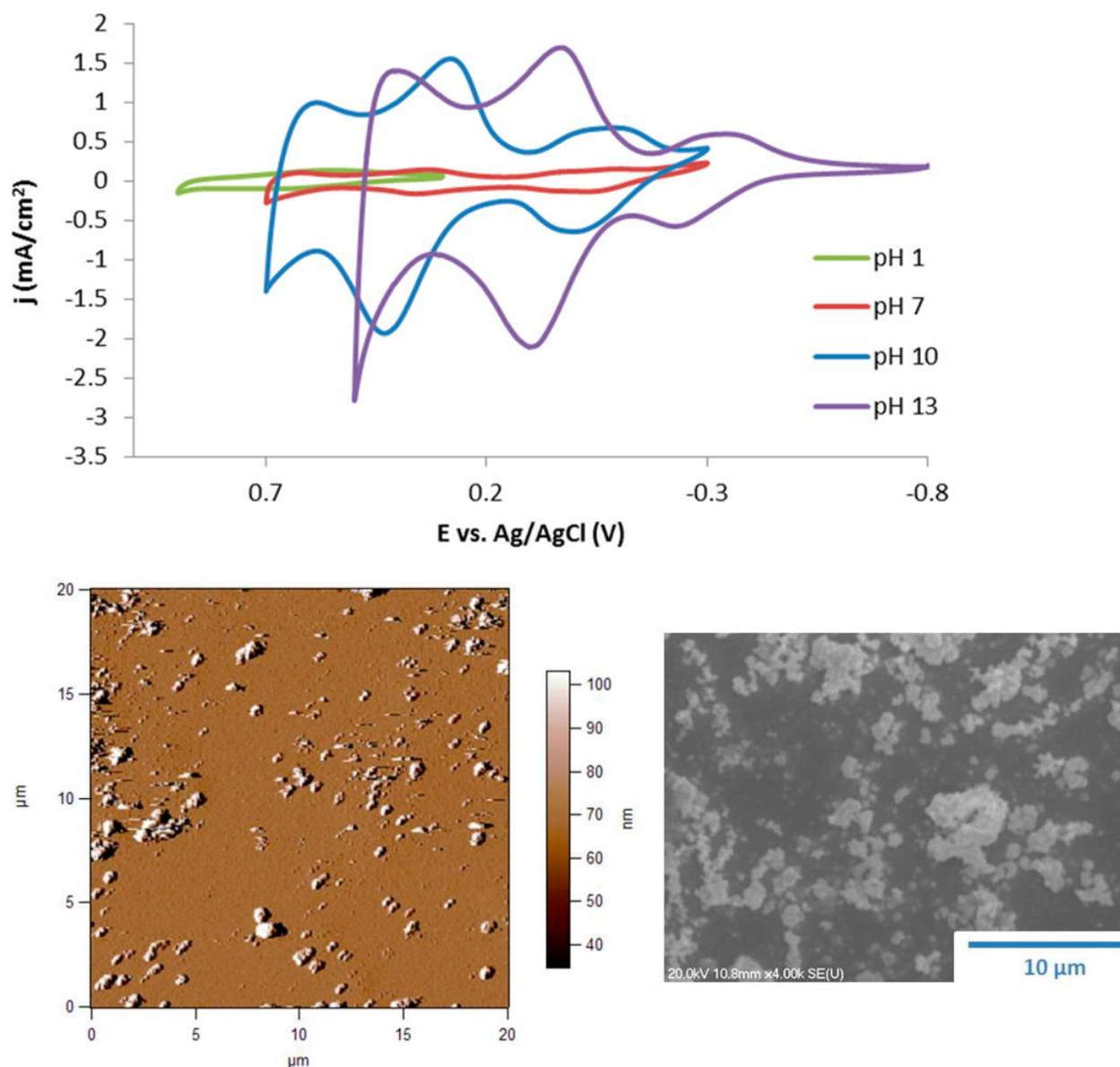


Figure 1.13. Top: Cyclic voltammetry after electroflocculation onto Au-coated slides of different pH IrOx NPs performed in pH 1 phosphate buffer (pH 1 NPs), pH 10 phosphate buffer (pH 7 and 10 NPs), and 0.1 M NaOH (pH 13 NPs). AFM (bottom left) and SEM (bottom right) images of electroflocculated IrOx NP films depicting the “islands” of NPs that form initially on the electrode surface. Reproduced with permission from Michaux, K. E.; Murray, R. W.

Langmuir **2013**, 29, 12254. Copyright 2013 American Chemical Society.

CHAPTER 2: KINETICS AND LOW TEMPERATURE STUDIES OF ELECTRON TRANSFERS IN FILMS OF SMALL (< 2 NM) AU MONOLAYER PROTECTED CLUSTERS²

2.1 Introduction

Understanding the physical and chemical properties of nanoscale materials is a contemporary part of nanoparticle science. The appearance of altered properties when the dimensions of a material is diminished from the macro- to the nanoscale is sometimes referred to as the quantum confinement effect, and at its lower limit, characteristics arise that are associated with molecules, such as HOMO-LUMO gaps.⁷⁶ Nanoparticle properties are additionally influenced by capping ligands, such as Au nanoparticles coated with thiolate monolayers, called monolayer protected clusters (MPCs).³⁷ In special cases, intermediate sizes of MPCs can exhibit electrochemical properties called quantized double layer charging (QDL).^{12,70,77}

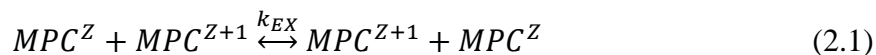
Among research reports on electron transfers (ET) between Au MPCs, most have dealt with MPCs in a solvent-wetted state,^{59,78,85,91,92,101,103,104,250} and fewer with Au MPC ETs in a solvent-dry state^{54,56,80,93,116,117,119,120,122,123,127,251-256} or at temperatures below 200 K.^{125,126,133,136,257-263} The present work departs from most previous studies of ETs by using highly monodisperse samples of Au MPCs of, or approaching, molecular size⁷⁶ and characterizing their ET kinetics in dry (solvent-free) amorphous films containing set proportions of donors and acceptors. Utilizing the core-charging voltammetry of highly monodisperse small

² This chapter is reproduced in part with permission from Carducci, T. M. and Murray, R. W. *J Am Chem Soc* **2013**, *135*, 11351. Copyright 2013 American Chemical Society.

Au MPC solutions, solid state films containing known states of electronic charging of the MPC cores can be prepared. In such dry films, ET reactions between MPCs can be induced under mild applied voltage gradients to exhibit linear current-voltage characteristics. Such measurements effectively yield solid state MPC film conductivities sensitive to their mixed valent state (such as a 1:1 mixed valent state, abbrev. $\text{MPC}^{\text{Z}+1/\text{Z}}$). The corresponding solid state electron self-exchange rates are the experimental topic of the present paper, with special emphasis on how their rates change over a wide span of temperature, e.g., from room temperature down to 77 K.

For this work, we select two size-purified 1-2 nm diameter Au MPCs: $\text{Au}_{144}(\text{SR})_{60}$ ($d_{\text{core}} = 1.6 \text{ nm}$)¹¹⁶ and $\text{Au}_{25}(\text{SR})_{18}$ ($d_{\text{core}} = 1.0 \text{ nm}$)⁹ that were prepared in roughly 1:1 mixed valent states of core charging, e.g., $\text{Au}_{144}(\text{SR})_{60}^{+1/0}$, $\text{Au}_{25}(\text{SR})_{18}^{0/-1}$, and $\text{Au}_{25}(\text{SR})_{18}^{+1/0}$. For the Au_{144} nanoparticle, SR is $-\text{S}(\text{CH}_2)_5\text{CH}_3$, and for the Au_{25} nanoparticle, SR is $-\text{S}(\text{CH}_2)_2\text{Ph}$. The mixed valent nanoparticle films were prepared by drop-casting of their deaerated mixed valent solutions onto interdigitated array electrodes (IDA) so that the MPC film thicknesses exceed the IDA finger heights. Voltage biases applied to the IDA finger pairs supply the voltage gradient impetus for electron hopping within the dry, mixed valent nanoparticle films. For notational simplicity, the MPCs will be referred to as $\text{Au}_{25}^{0/-1}$, $\text{Au}_{25}^{+1/0}$, and $\text{Au}_{144}^{+1/0}$.

Previous electronic conductivity studies of Au MPC films of small, but not highly monodisperse, core sizes ($\text{Au}_{25}^{12,21}$ to Au_{976}) with alkanethiol ligand shells^{4,56,116,131,264} were suggested to involve an ET pathway along the ligand chain to progress from Au core to core.⁴ This process, illustrated in Figure 2.1, is equivalent to a bimolecular electron “self-exchange” between MPCs according to¹¹⁶



where k_{EX} is the bimolecular nanoparticle electron self-exchange rate constant ($M^{-1} s^{-1}$). As with any bimolecular process, the ET rate and corresponding electronic conductivity, $\sigma_{EL}(\Omega^{-1} cm^{-1})$, are maximized when $[MPC^{Z+1}] = [MPC^Z]$. Electronic conductivity in a sample of univalent MPCs (say, containing 100% of the neutral species, MPC^0) would proceed via self-exchange between charge carriers thermally generated by disproportionation. The disproportionation pathway is relatively unimportant for Au MPCs having a significant potential spacing between sequential charge state couples,⁵⁶ as in Au_{144} and Au_{25} .

This study expands on previous work at ambient temperatures by using more monodisperse syntheses of $Au_{144}^{+1/0}$ and $Au_{25}^{0/-1}$ nanoparticles and by looking at ET kinetics in the $Au_{25}^{+1/0}$ redox couple in addition to $Au_{25}^{0/-1}$. Most importantly, we further examine electronic conductivity in Au MPC films at cryogenic temperatures. Non-Arrhenius ET behavior at low temperatures was previously observed by our group¹¹⁵ in films of mixed-valent osmium bipyridine polymers and by the Dhirani^{132,258-260,263} group in much larger, polydisperse Au nanoparticles, as examples. At ambient temperatures, the greater occupancy of the upper vibrational states allows the reaction to proceed over the classical thermal barrier, whereas with decreasing temperature, the reaction is hypothesized to proceed increasingly by tunneling because of the depletion of the upper vibrational states.^{137,265} In the present case, highly monodisperse, small Au MPC ETs in mixed-valent films at low temperatures unsurprisingly do not conform to a vibronic model and are instead treated simply as a transition from ET occurring predominantly over the classical thermal activation energy barriers to temperature-independent rates for electron tunneling at low temperatures.

2.2 Experimental

2.2.1 Materials.

Hydrogen tetrachloroaurate(III) trihydrate ($\text{HAuCl}_4 \cdot 3\text{H}_2\text{O}$) was synthesized according to the literature.^{266,267} 1-Hexanethiol ($\text{C}_6\text{H}_{13}\text{SH}$, 95%), 2-phenylethanethiol ($\text{HSPH}(\text{CH}_2)_2\text{SH}$ 98%), sodium borohydride (NaBH_4 , 99%), and tetraoctylammonium bromide (Oct_4NBr , 98%) were purchased from Sigma-Aldrich (St. Louis, MO), tetrabutylammonium perchlorate (Bu_4NClO_4 , 99.0%) from Fisher Scientific (Suwanee, GA) or Fluka (Milwaukee, WI), and toluene (certified ACS reagent), methanol (optima grade), acetonitrile (CH_3CN , optima grade), and dichloromethane (CH_2Cl_2 , optima grade) from Fisher Scientific. Ethanol (absolute, i.e., 200 proof) was purchased from Pharmco-Aaper (Shelbyville, KY) or Decon Laboratories, Inc. (King of Prussia, PA). All chemicals were used without further purification. Nanopure water (resistance $> 18 \text{ M}\Omega$) was prepared with a Thermo Scientific Barnstead Nanopure ultrapure water purification system.

2.2.2 Synthesis of Au MPCs.

The syntheses^{70,242} of $\text{Au}_{144}(\text{SC}_6\text{H}_{13})_{60}$ and $\text{Au}_{25}(\text{SC}_2\text{Ph})_{18}$ as monodisperse nanoparticles are described in Appendix A in greater detail than previously reported.

2.2.3 Characterization of Au MPCs.

The monodispersity of synthesized Au_{144} and Au_{25} nanoparticles were confirmed through voltammetry using a Pine WaveNano Potentiostat as illustrated by the differential pulse voltammetry patterns of Figure 2.2. QDL charging with uniformly spaced peaks is observed in the voltammetry for Au_{144} ⁷⁰ while Au_{25} ²⁶⁸ nanoparticles display their known HOMO level doublet of peaks. The UV-visible spectrum (data not shown) of $\text{Au}_{25}(\text{SC}_2\text{Ph})_{18}$ was obtained

using a Thermo Evolution Array UV-Visible Spectrophotometer. All expected characteristic spectral features²⁴² were observed.

2.2.4 Preparation of Mixed-Valent Au MPCs.

Bulk electrolysis of Au MPCs was performed in a fine frit-separated three-compartment cell using a Pine WaveNow Potentiostat. The electrolysis was aimed to acquire Au MPC samples with known mixed valencies especially near 1:1 mole ratios, e.g., Au₁₄₄^{+1/0}, Au₂₅^{0/-1}, and Au₂₅^{+1/0}. Electrolysis potentials (E_{Elec}) were chosen based on the Nernst equation^{63,83} with reference to known MPC voltammetry

$$E_{Elec} - E^{Z+1/Z} = 0.059 \log \frac{[MPC^{Z+1}]}{[MPC^Z]} \quad (2.2)$$

where $E^{Z+1/Z}$ was determined by DPV of the Au MPCs. The working electrode was a Pt gauze (Sigma-Aldrich) and was placed with the reference electrode in cell compartment 1, with the Pt counter electrode in compartment 3. In preparing mixed-valent samples of Au₁₄₄, compartment 1 contained ~10 mL of 1 mM Au₁₄₄ in CH₂Cl₂ plus 10 mM Bu₄NClO₄ as supporting electrolyte; compartments 2 and 3 contained only 10 mM Bu₄NClO₄/CH₂Cl₂. In preparing mixed-valent Au₂₅ nanoparticles, compartment 1 contained ~10 mL of 1 mM Au₂₅ plus 1 mM Bu₄NClO₄ in CH₂Cl₂ while compartments 2 and 3 contained only 1 mM Bu₄NClO₄/CH₂Cl₂. All cells were stirred and degassed with dichloromethane-saturated Ar. When the electrolysis current dropped to ~ 1% of the initial value, the electrolysis was stopped and the open circuit potential was checked.

Following bulk electrolysis, the Au MPC sample solution was thoroughly degassed again and its open circuit potential vs. Ag/AgCl reference determined at a clean Pt wire, using a Keithley Instruments 610C solid-state electrometer (input impedance > 10⁸ MΩ). The MPC

charge state distribution was calculated from the rest potential and the DPV-determined formal potentials according to Equation 2.

Mixed-valent samples of Au₁₄₄ were washed twice with CH₃CN following bulk electrolysis to remove excess electrolyte. The wash steps did not alter the open circuit potential. Samples of Au₂₅ were not washed because the electrolyte concentration was only 1 mM.

2.2.5 *Film Preparation on Interdigitated Array Electrodes.*

IDAs (microfabricated in-house by the Chapel Hill Analytical and Nuclear Laboratory, CHANL) had 50 interdigitated Au fingers on a glass substrate. IDAs made for Au₁₄₄ measurements had 0.298 cm long fingers spaced 15 μ m apart. IDAs made for Au₂₅ samples had 50 interdigitated fingers (0.298 cm long) spaced 10 μ m apart; the smaller IDA gap was chosen to increase currents in the conductivity scans. Connections to finger sets were made with soldered wire leads covered with epoxy resin. Films of Au MPCs were drop-cast onto the IDA electrodes from concentrated Au MPC toluene solutions, ~ 10 mg in one small drop. Au₁₄₄ MPC concentrations in the solid-state films were 0.07 M based on pycnometry. Au₂₅ was 0.17 M as determined previously⁵⁶ by UV-visible spectroscopy. IDA electrodes were rinsed thoroughly but gently with CH₂Cl₂ and plasma-cleaned between uses.

2.2.6 *Low Temperature Conductivities of Solid-State Au MPC Films.*

Temperatures of Au MPC films were controlled using a Janus VPF 100 liquid nitrogen cryostat system and Lakeshore 331S temperature controller. IDAs with drop-cast Au MPC films were secured to the heat-conducting sample stage of the cryostat using double sided tape. The cryostat chamber was evacuated overnight using an Edwards RV8 rotary vane pump, which is required for proper function of the temperature controls and to ensure complete drying of the MPC films. The cryostat cooling chamber was filled with liquid nitrogen and allowed to cool to

the minimum temperature (~ 77 K) prior to initiation of electronic conductivity measurements of solid-state mixed-valent Au MPC films. Measurements were done using a home-built two-electrode circuit designed for applying a voltage ramp and measuring currents as low as 10^{-10} A (controlled by LabView software). Capacitance was minimized by connecting the circuit directly to the cryostat. Electronic conductivities were calculated from the slopes of current-potential plots in the linear potential bias interval between -0.25 to 0.25 V (initial and final voltage is 0 V). The scan rate was 10 V/s, a rate aimed at avoiding ion migration within the film. As an additional caution against electrostatic migration of counterions of the mixed valent film and its consequent electrolysis, conductivity measurements were not performed above 300K. Conductivity scans were performed at temperature intervals between 2 and 10 K as the IDA electrode was heated in a controlled manner from 77 to 300 K. Temperature was always varied from low to high due to constraints of the cryostat. Repeat experiments on a given MPC film and IDA showed no significant differences. All data reported are averages from different IDAs with different MPC films.

The mixed valent MPC film electronic conductivity, σ_{EL} , was calculated from the slopes of the current-potential plots according to^{56,116}

$$\sigma_{EL} = \left(\frac{d}{A_{Total}} \right) \frac{\Delta i}{\Delta E} \quad (2.3)$$

where d is IDA gap, A_{Total} is area of the walls of facing parallel plate finger electrodes, A_{Finger} , times height taken as the maximum conductive MPC film thickness (*ca.* 1 μm), and length equal to the finger length times $N - 1$ where N is the total number of fingers (50). (Note that the current of each interior finger is double that of an end finger.) The ratio $\frac{d}{A_{Total}}$ comprises the geometric cell constant, C_{Cell} , which for the IDAs used for Au₁₄₄ films was 1.021 cm^{-1} and for Au₂₅ films was 0.685 cm^{-1} .

2.3 Results and discussion

2.3.1 Electronic Conductivity of Au MPC Films from 77 to 300 K Temperatures.

Electronic conductivity results for Au MPC films from 77 to 300 K are presented in Figures 2.3 and 2.4 as Arrhenius plots. The data can be divided into two regimes of behavior; higher temperatures display thermally activated ET (electron hopping) and strongly temperature-dependent rates, while at lower temperatures the ET conductivity becomes temperature-independent, which is characteristic of electron tunneling. To our knowledge, the latter is the first report of nanoparticle-to-nanoparticle electron tunneling in 1-2 nm Au MPCs.

In the thermally activated ET region at higher temperatures, the relevant relation is⁴

$$\ln(\sigma_{EL}) = \frac{-E_A}{RT} - r_0\beta + \ln\sigma_0 \quad (2.4)$$

where β (cm⁻¹) is an electronic coupling term⁴ for ET tunneling through the MPC organothiolate ligand shell, and r_0 (cm) is the average edge-to-edge distance between neighboring MPC Au cores. The y-intercept represents the equivalent of an infinite-temperature electronic conductivity.^{4,116} The activation energy barrier (E_A) to ET in the Au MPC films was taken from the best-fit slopes over the data points taken at temperatures from 265 to 300 K.

Figures 2.3 and 2.4 show that the transition between thermally activated and tunneling ET behavior is gradual.^{115,137} In any redox system, the current measured at any given temperature can be expressed as the sum of currents arising from all ET pathways.¹³⁷ In the flattened, low temperature regions of the Arrhenius plots of Figures 2.3 and 2.4, the ET conductivity arises solely through the mechanism of tunneling. The tunneling current dominates at low temperatures as energy-activated states become irrelevant; thermal energy is depleted and electron hopping diminished. In the thermally activated region, the electron hopping mechanism

dominates, and tunneling current becomes a minor contributor since it retains its small value regardless of temperature.

In a previous study,¹¹⁵ we assessed tunneling parameters for low temperature ET in mixed-valent osmium bipyridine polymers using the Holstein²⁶⁵ equation. In the present case, we were unable to produce satisfactory fits to the data in Figures 2.3 and 2.4. We conclude that the vibronic Holstein model is not an appropriate one for the present experiments, and use instead simply a classical tunneling description.

The limiting values of the temperature independent conductivities (near 77 K) were not very reproducible (uncertainty *ca.* $\pm 67\%$), but some semi-quantitative observations about the efficacy of electron tunneling for the different Au MPC samples are possible. From Figure 2.3, the electron tunneling current appears to be core size-dependent; that for Au₁₄₄ MPCs is $>$ Au₂₅. This difference occurs in spite of the difference in nanoparticle ligand; those of the Au₂₅ nanoparticles are partly aromatic. Secondly, the Au₂₅L₁₈^{1+/0} data in Figure 2.4 indicate that the tunneling currents are largest for MPC samples with mixed valency nearest 1:1. Thirdly, the effect of core size is larger than that of mixed valent proportions within a given redox couple (Figure 2.3). Finally, the low temperature tunneling currents for mixed-valent Au₂₅^{0/-1} exceed those for Au₂₅^{+1/0}. Normalizing for proportions of mixed valency beings the conductivity data together for high but not low temperatures. These trends in the tunneling currents largely mimic those of conductivities at higher temperatures, as discussed further in the next section.

2.3.2 E_A and σ_{EL} Measurements in the Thermally-Activated Region.

Table 2.1 presents values of E_A and σ_{EL} (at $T = 298$ K) for the different Au MPC redox couples; these values are averages from three different films with the same mixed valent composition. As noted in the introduction, a significant difference in E_A and σ_{EL} for Au₁₄₄ and

Au₂₅ has previously been reported.⁵⁶ This core size effect is also seen in the present data, which are for more highly monodisperse MPCs; E_A for Au₂₅ is more than 2-fold larger than for Au₁₄₄, and σ_{EL} is about one order of magnitude larger for Au₁₄₄^{+1/0} than Au₂₅^{0/-1}. Possible origins of increase in E_A and decrease in σ_{EL} for smaller core sizes of metal-based MPCs are an increase in density of states for larger particles²⁶⁹ requiring a smaller Marcus inner-sphere reorganizational energy⁵⁶ and increased consequences of any Coulomb blockade-like phenomena.²⁷⁰

Previously reported^{56,116} values of σ_{EL} for Au₁₄₄ and Au₂₅^{0/-1} MPCs were *ca.* $10^{-5} \Omega^{-1} \text{cm}^{-1}$ and $10^{-7} \Omega^{-1} \text{cm}^{-1}$, respectively. Differences in the present data are possibly related to differences in the degree of MPC monodispersity or to our improved method of cleaning of electrodes. Cleaning of IDA electrodes with piranha solution in previous studies produces some scattered damage to the Au fingers. The present cleaning procedure did not produce changes due to surface conductivity of the glass bottom of the IDA channels, as shown by a control experiment of an “empty” (no nanoparticle film) IDA; see the “blank” IDA result of Figure 2.4.

The present room temperature E_A and σ_{EL} data allow a comparison of the electronic conductivities of solid-state films of Au₂₅ nanoparticles to the rates of electron transfers between dissolved Au₂₅ nanoparticle couples. Solution voltammetry⁵⁸ of freely diffusing Au₂₅ nanoparticles disclosed that ET was slower for the Au₂₅^{+1/0} than that for the Au₂₅^{0/-1}, by about half an order of magnitude. This kinetic difference is also seen for the solid state materials; the electronic conductivity in the solid state Au₂₅^{+1/0} couple was slower than that for the Au₂₅^{0/-1} couple by about one order of magnitude.

The role of the counterion is a potentially significant component of the electronic conductivities of samples of mixed valent Au₂₅^{+1/0} MPCs relative to those of Au₂₅^{0/-1} MPCs. Films of Au₂₅^{0/-1} contain a counterion (Bu₄N⁺ in the present case), while those of Au₂₅^{+1/0} MPCs

contain the counterion ClO_4^- . What role(s) the choice of solid state counterion play are unknown, whether benign observers or active participants in some way. Differences in the electrolyte may be responsible for example for the variation in E_A between the two redox state pairs. Direct evidence, such as a study comparing $\text{Au}_{25}^{+1/0}$ and $\text{Au}_{25}^{0/-1}$ with varying electrolytes species present, is lacking at present and so this issue is unresolved.

2.3.3 Expression of Conductivity as Electron Self-exchange Rate Constants.

We have previously expressed electronic conductivities of mixed valent Au MPCs as bimolecular electron self-exchange rate constants (k_{EX}) by assuming a cubic lattice film structure^{56,92,112,116,117}

$$k_{EX} = \frac{6(10^3)RT\sigma_{EL}}{F^2\delta^2[MPC^{Z+1}][MPC^Z]} \quad (2.5)$$

where δ is the core-to-core edge separation (cm), and $[MPC^{Z+1}]$ and $[MPC^Z]$ are calculated from the Nernst equation. δ for Au_{144} was previously estimated as 2.5 nm, from TEM images showing a core diameter of 1.6 nm,²⁷¹ to which was added 0.15 nm per $-\text{CH}_2$ of the hexanethiolate ligand.¹¹⁶ For Au_{25} , δ was estimated⁵⁶ as 2.4 nm based on the model

$$\delta_{\text{Au}_{25}} = 2r_{\text{Core}} + l_{\text{Eff}} = 2 \left(\frac{(0.7)(10^3)}{\frac{4}{3}\pi C_{\text{Film}} N_{\text{Avo}}} \right)^{\frac{1}{3}} \quad (2.6)$$

where r_{Core} is Au_{25} MPC core radius, l_{Eff} is the ligand-separated distance between two cores, C_{Film} is the mol/cm^3 MPC concentration, and 0.7 is a hexagonal packing fill factor. C_{Film} was taken as 0.17 M for Au_{25} , as determined through UV-visible absorption spectroscopy⁵⁶ and 0.07 M for Au_{144} determined through pycnometry (see Experimental). The value of δ estimated for Au_{144} suggests almost complete interdigitation of the ligands of neighboring particles, while the calculated value for Au_{25} suggests no ligand interdigitation. Lopez-Acevedo, et al.,⁷³ in density functional theory calculations recently estimated the Au_{144} core radius as 8 Å, in agreement with

TEM measurements. Heaven, et al.⁹ reported the crystal structure of the Au₂₅ MPC and the diameter was 2.39 nm, which is close to the above result from a cubic lattice model. Thus, while the two diameters are nominally close, the data background indicates that $\delta_{Au_{144}} = 2.5$ nm and $\delta_{Au_{25}} = 2.4$ nm.

Our previous studies^{56,116} showed that k_{EX} is maximized in films where $[MPC^{Z+1}] = [MPC^Z]$ in Au₁₄₄ and Au₂₅^{-1/0}. The data in Table 2.1 (r.h. column) for mixed valent Au₂₅^{+1/0} are consistent with these observations, and also show that k_{EX} for mixed valent Au₂₅^{+1/0} is ca. 10-fold smaller than that for the Au₂₅^{+1/0} couple (like the σ_{EL} difference). We use the same value of δ for Au₂₅^{0/-1} and Au₂₅^{+1/0} to calculate k_{EX} , having no basis to assume a difference from Au₂₅^{0/-1}.

In summary, we find that electron transfer rates in mixed valent films of monodisperse Au₂₅(SC₂Ph)₁₈ and Au₁₄₄(SC₆H₁₃)₆₀ nanoparticles can be observed over a complete range of thermal activation of electron hopping to temperature-independent rates of electron hopping at lowered temperatures. The electron hopping rates at lowered temperatures fall in the order Au₁₄₄^{+1/0} > Au₂₅^{0/-1} > Au₂₅^{+1/0}.

2.4 Acknowledgements

The authors thank Stephen W. Feldberg and Norman Sutin of Brookhaven National Laboratories for insightful comments during the course of this work, Collin McKinney and Matt Verber of the UNC Electronics Facility for conductivity circuit design, and Bob Geil of CHANL for microfabricating IDA electrodes. This work was supported by the Office of Naval Research. Tessa Carducci acknowledges support from a National Defense Science & Engineering Graduate (NDSEG) Fellowship, from the Department of Defense.

2.5 Tables and figures

Table 2.1. Thermally-activated ET parameters: Activation energy barriers (E_A), electron hopping conductivities (σ_{EL}), and self-exchange rate constant (k_{EX}) at 298 K of solid-state, mixed valent Au MPC films

MPC	[MPC ^{Z+1}]	E_A	σ_{EL}	k_{EX}
	(%)	(eV)	($\Omega^{-1} \text{ cm}^{-1}$)	($\text{M}^{-1} \text{ s}^{-1}$)
Au ₁₄₄ ^{+1/0}	55 ^a	0.17 ± 0.02	$5.9 \pm 0.9 \times 10^{-6}$	$1.24 \pm 0.19 \times 10^8$
Au ₂₅ ^{0/-1}	53	0.38 ± 0.03	$6.3 \pm 2.2 \times 10^{-7}$	$2.44 \pm 0.86 \times 10^6$
	< 1 ^b	0.46 ± 0.02	$1.6 \pm 0.7 \times 10^{-8}$	N/A
Au ₂₅ ^{+1/0}	45	0.34 ± 0.09	$6.4 \pm 1.2 \times 10^{-8}$	$2.50 \pm 0.47 \times 10^5$
	64	0.47 ± 0.07	$4.4 \pm 3.1 \times 10^{-8}$	$1.8 \pm 1.3 \times 10^5$
	7 ^b	0.7 ± 0.1	$1.7 \pm 1.2 \times 10^{-9}$	$2.6 \pm 1.8 \times 10^4$

^a Avg. of four different films having the same mixed valent composition

^b Avg. of two different films having the same mixed valent composition

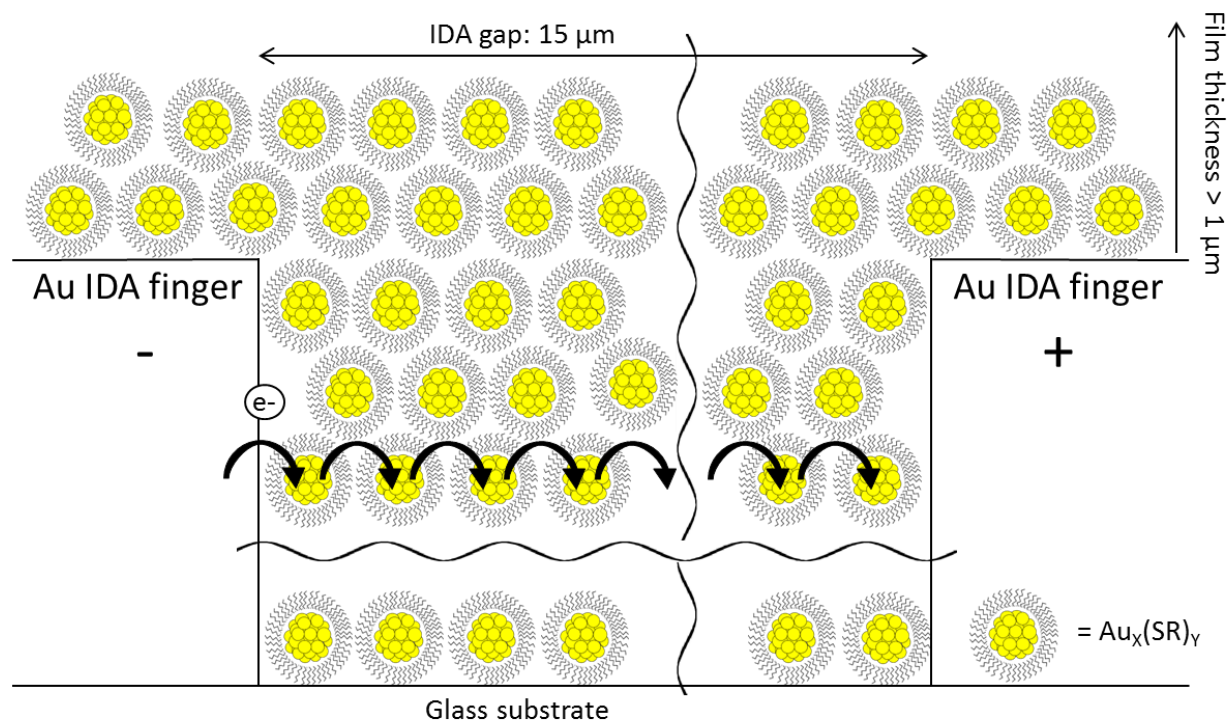


Figure 2.1. Cartoon of electron hopping conductivity in mixed-valent Au MPC film on an IDA electrode

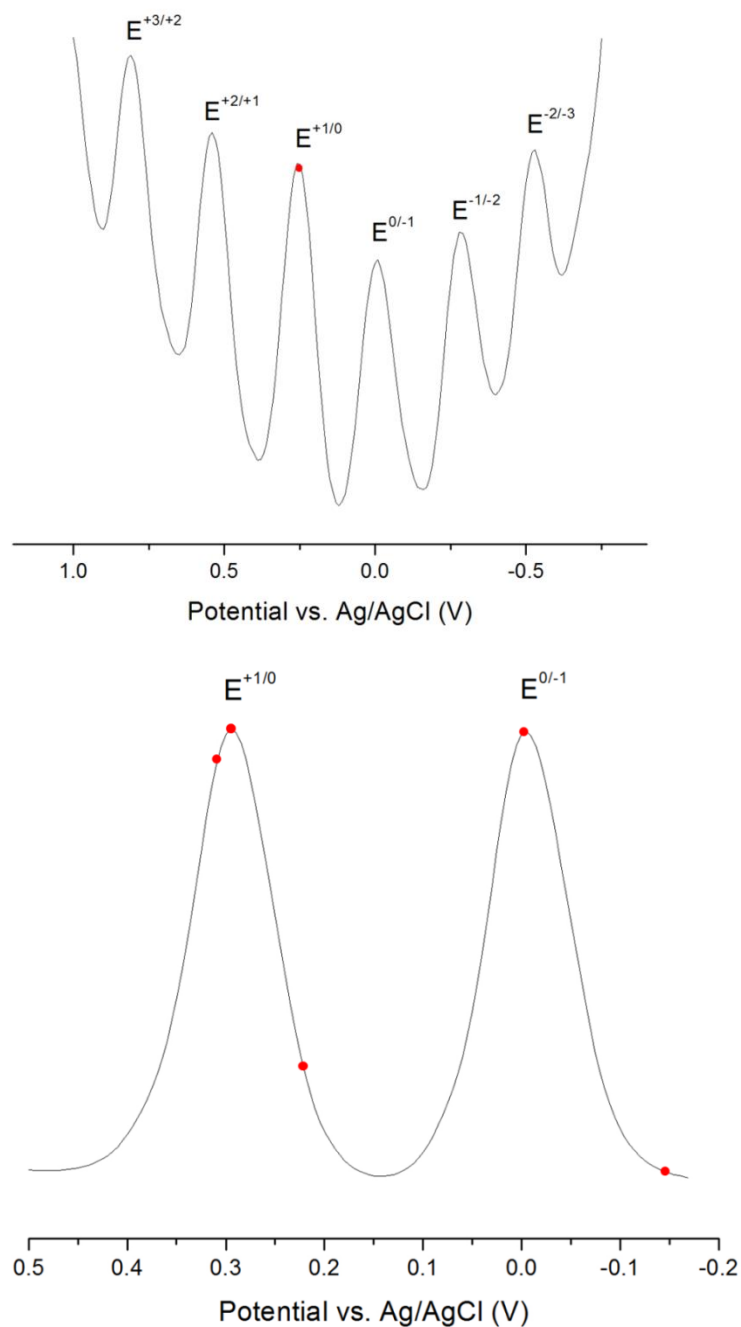


Figure 2.2. Differential pulse voltammetry of Au_{144} and Au_{25} MPCs: (Top) ~ 1 mM $\text{Au}_{144}(\text{SC}_6\text{H}_{13})_{60}$ in 0.1 M $\text{Bu}_4\text{NClO}_4/\text{CH}_2\text{Cl}_2$ at 0.020 cm^2 Pt disk. Points in red are rest potentials of solutions from which mixed valent MPC samples were isolated. (Bottom) ~ 1 mM $\text{Au}_{25}(\text{SC}_2\text{Ph})_{18}$ in 0.1 M Bu_4NClO_4 in CH_2Cl_2 . Data taken with a Pine WaveNano Potentiostat.

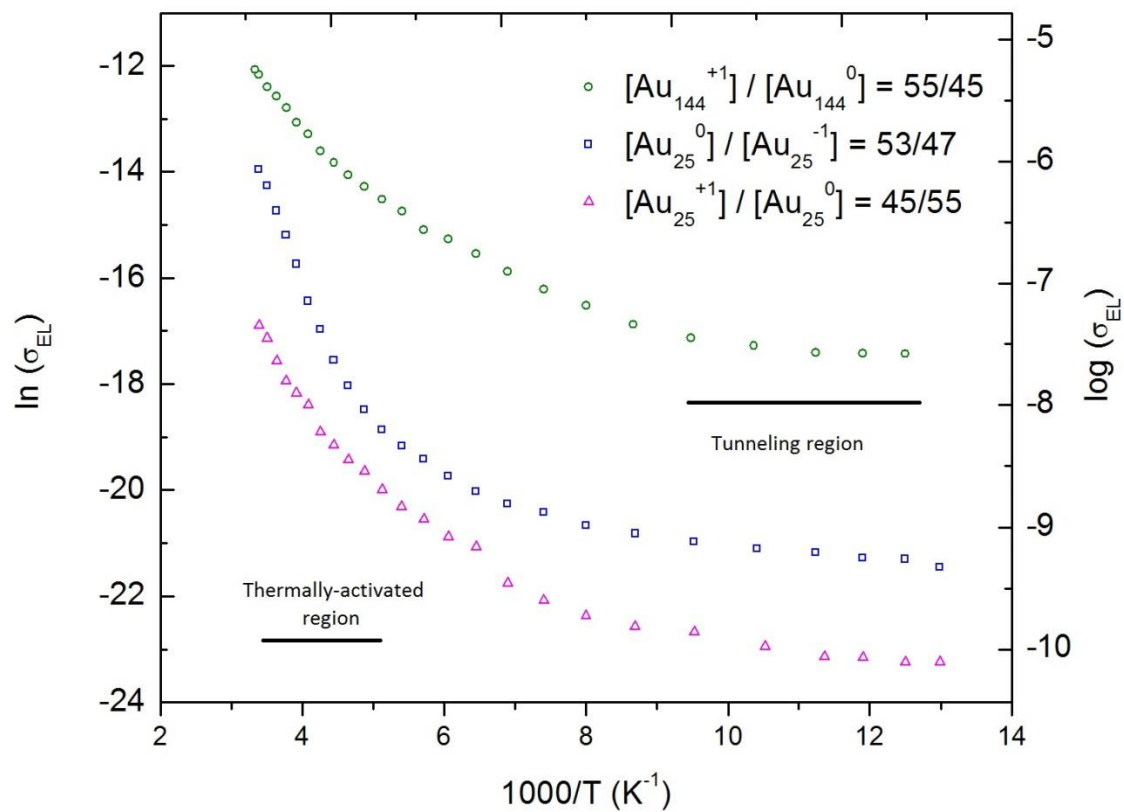


Figure 2.3. Arrhenius plot of mixed valent solid state Au MPC films containing indicated molar proportions of each MPC charge state.

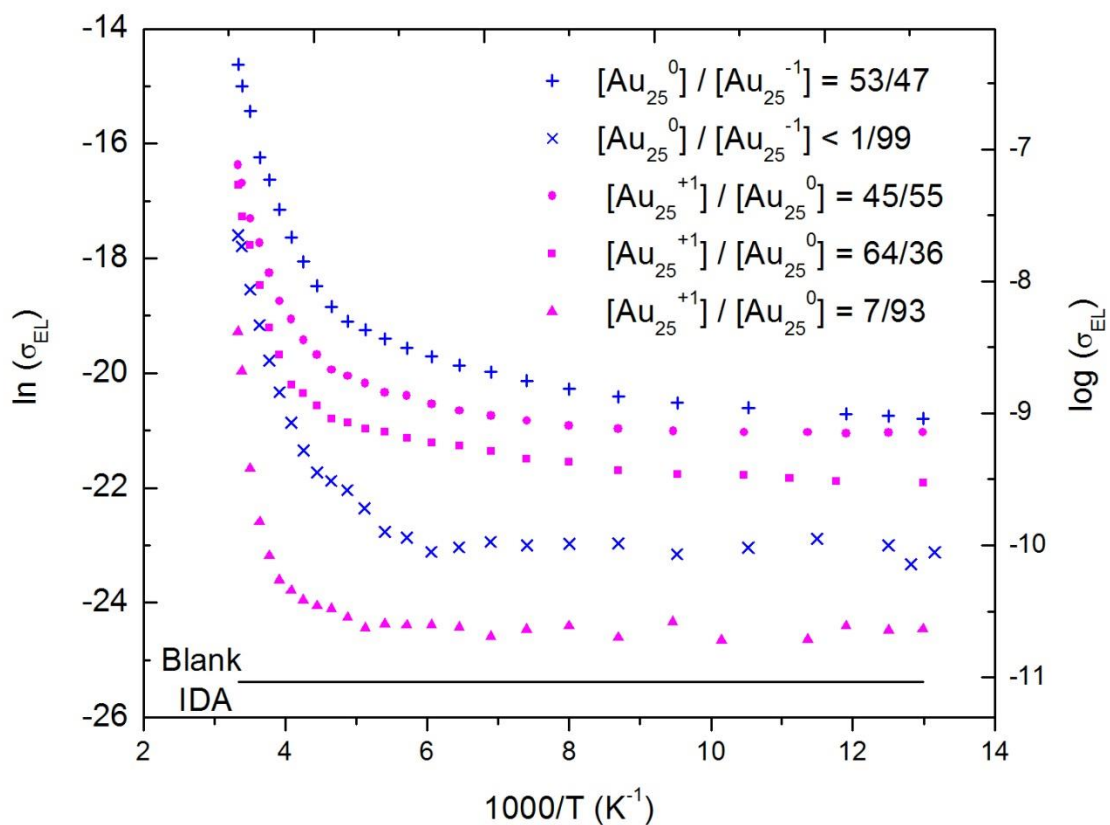


Figure 2.4. Arrhenius plots of mixed valent solid state Au_{25} MPC films containing the indicated proportions of the 0/-1 or +1/0 charge states. The blank IDA line is for an IDA electrode bearing no MPC film

CHAPTER 3: TEMPERATURE DEPENDENCE OF SOLID STATE ELECTRON EXCHANGES OF MIXED VALENT FERROCENATED AU MONOLAYER PROTECTED CLUSTERS³

3.1 Introduction

A fundamental understanding of nanoparticles is the foundation for applications of devices made from them. Nanoparticles of varied size can display a wide range of properties. Au monolayer protected clusters (MPCs) in the 1-2 nm size regime exhibit distinctive electrochemical behaviors. The smallest MPCs—e.g., Au₂₅ nanoparticles—are molecule-like, having HOMO-LUMO energy gaps⁷⁶ which can be observed in their voltammetry. Slightly larger ones—e.g., Au₁₄₄ and Au₂₂₅—display electrochemical properties called quantized double layer charging (QDL).^{12,70,77} These electrochemical features, and solubilities and spectra, are further moderated by the thiolate ligands that can be used to coat the Au MPC core surfaces.^{12,37} Inclusion of thiolate ligands with redox or bio-active groups opens the door to further customization of nanoparticles towards specific applications.^{12,37,178}

Functionalization of MPCs with multiple redox ligands, such as ferrocenes, increases the nanoparticle redox capacity to transfer multiple electrons within a small range of potential. Ferrocenes can be added to the MPC ligand shells either by a post-synthesis ligand exchange reaction^{6,14,15} or be fully ferrocenated when synthesized *de novo*.⁵⁷ Early work⁵ showed that functionalization of Au MPCs with a ferrocene (Fc) thiol can lead to multi-ET reactions for both

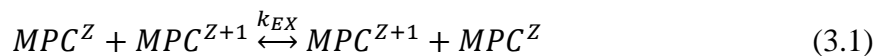
³ This chapter is reproduced in part with permission from Carducci, T. M.; Blackwell, R. E.; Murray, R. W. *J Am Chem Soc* **2014**, *136*, 11182. Copyright 2014 American Chemical Society.

freely diffusing nanoparticles and for electrode-adsorbed clusters. More recently, Schiffrin and coworkers¹⁷⁷ synthesized 1.8 nm (dia.) Au MPCs containing 4, 7 or 10 Fc thiolate ligands, using ligand exchanges, and observed their electron transfer reactions.

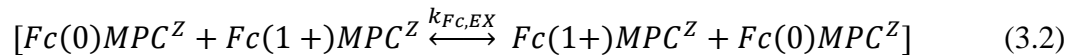
Most studies of electron transfers (ETs) of ferrocenated Au MPCs have focused on solution-wetted films on electrode surfaces¹⁷⁹⁻¹⁸¹ and their charge storage capabilities.¹⁸³ Ferrocene labels have also been used in combination with Au nanoparticles to enhance current response in sensors.^{178,272, as examples} Little is known, however, about how the Fc group might affect electron exchanges of Au clusters as solid state samples, including their ET behavior at low temperatures.

The present study is of highly monodisperse Au MPCs containing small numbers of ferrocene sites in their ligand shells. In solvent-free dry films, ET reactions between neighbor MPCs and their ferrocene substituents can be induced by mild applied voltage gradients, exhibiting thereby linear current-voltage characteristics.¹¹⁸ Such studies show that these solid state conductivities of MPC films are sensitive to the film's mixed valent state. The corresponding solid state electron self-exchange rates are the experimental topic of the present paper, with special emphasis on how their rates change over a wide span of temperature, e.g., from room temperature down to 77 K.

Previous electronic conductivity studies of Au MPC films of small, highly monodisperse, core sizes were suggested to involve an ET pathway along the ligand chain to progress from Au core to core.⁴ This process has been described as a bimolecular electron “self-exchange” between MPCs according to¹¹⁶



where k_{EX} is the bimolecular nanoparticle electron self-exchange rate constant ($M^{-1} s^{-1}$). In the present study, the MPCs bear multiple ferrocene thiolate ligands, in mixed valent $Fc^{0/+}$ form, and the ferrocene $^{0/1+}$ couple supports multiple electron exchanges so that MPC-MPC electron transfers become less prominent in the voltammetry, e.g.,



In this reaction, $k_{Fc,EX}$ is the rate constant of interest. As with any bimolecular process, the contributions of ferrocene electron transfers to the nanoparticle sample's electronic conductivity, $\sigma_{EL}(\Omega^{-1} cm^{-1})$, becomes maximized when the $Fc(0)$ and $Fc(1+)$ populations on the MPCs are equal.

The experiments presented examine electron-hopping conductivities in films of ferrocene-containing Au_{225} , Au_{144} , and Au_{25} nanoparticles, from room temperature to cryogenic temperatures. Like non-ferrocenated Au_{144} and Au_{25} MPCs, non-Arrhenius (temperature-independent) ET behavior is observed at low temperatures —indicative of an electron tunneling mechanism.^{118,137} For these studies, we select three size-purified 1-2 nm diameter Au MPCs: $Au_{225}(SR)_{75}$, $Au_{144}(SR)_{60}$ and $Au_{25}(SR)_{18}$. For the Au_{225} and Au_{144} nanoparticles, the thiolate ligand SR is $-S(CH_2)_5CH_3$, and for the Au_{25} nanoparticle, SR is $-S(CH_2)_2Ph$. Partial ferrocenation of the thiolate ligand shell was accomplished via ligand exchanges with 6-(ferrocenyl)hexanethiol. Fc-Au MPCs were electrolytically made mixed valent with respect to the $Fc^{+1/0}$ redox couple. The mixed-valent nanoparticle films were dropcast from their deaerated, mixed-valent solutions onto interdigitated array electrodes (IDA) so that the MPC film thicknesses exceed the IDA finger heights. Voltage biases applied to the IDA finger pairs supply the voltage gradient impetus for electron hopping within the dry, mixed-valent nanoparticle

films. For notational simplicity, the non-ferrocenated MPCs will be referred to as Au₂₅, Au₁₄₄, and Au₂₂₅ and the ferrocenated versions as Au₂₅Fc, Au₁₄₄Fc, and Au₂₂₅Fc.

3.2 Experimental

3.2.1 Materials.

Hydrogen tetrachloroaurate(III) trihydrate (HAuCl₄·3H₂O) was synthesized according to the literature.^{266,267} 1-Hexanethiol (C₆H₁₃SH, 95%), 2-phenylethanethiol (HSPH(CH₂)₂SH 98%), 6-(ferrocenyl)hexanethiol (C₁₆H₂₁FeSH), sodium borohydride (NaBH₄, 99%), and tetraoctylammonium bromide (Oct₄NBr, 98%) were purchased from Sigma-Aldrich (St. Louis, MO), tetrabutylammonium perchlorate (Bu₄NClO₄, 99.0%) from Fisher Scientific (Suwanee, GA) or Fluka (Milwaukee, WI), and optima grade toluene, methanol (CH₃OH), acetonitrile (CH₃CN), and dichloromethane (CH₂Cl₂) from Fisher Scientific. Ethanol (absolute, i.e., 200 proof) was purchased from Decon Laboratories, Inc. (King of Prussia, PA).

3.2.2 Synthesis of Au MPCs.

The syntheses of Au₂₂₅(SC₆H₁₃)₇₅, Au₁₄₄(SC₆H₁₃)₆₀ and Au₂₅(SC₂Ph)₁₈ as monodisperse nanoparticles were carried out as described previously.¹¹⁸ Partial ferrocenation of the Au₂₂₅, Au₁₄₄, and Au₂₅ nanoparticles' ligand shells was achieved through a post-synthesis ligand exchange reaction.⁵ Briefly, a ~ 1 mM solution of as-synthesized nanoparticles was stirred overnight with 6-(ferrocenyl)hexanethiol in various stoichiometric ratios with the nanoparticle depending on desired level of ferrocenation (1-5 fold excess). Free thiol was removed by nanoparticle precipitation by added CH₃CN for Au₂₂₅Fc and Au₁₄₄Fc and CH₃OH for Au₂₅Fc, recovering the nanoparticles by centrifugation.

3.2.3 *Film Preparation on Interdigitated Array Electrodes.*

The IDAs used (microfabricated in-house by the Chapel Hill Analytical and Nuclear Laboratory, CHANL) had 50 interdigitated Au fingers on a glass substrate. Fingers of IDAs made for Au₂₂₅ and Au₁₄₄ measurements were 0.298 cm long and spaced 15 μm apart. IDAs made for Au₂₅ samples had 50 interdigitated fingers (0.298 cm long) spaced 10 μm apart; the smaller IDA gap was chosen to increase currents in the conductivity scans. Connections to finger sets were made with soldered wire leads covered with epoxy resin. Films of Au MPCs were dropcast onto the IDA electrodes from concentrated Au MPC toluene solutions, ~ 10 mg in one small drop.

3.3. **Results and discussion**

3.3.1 *Characterization of Au MPCs.*

The differential pulse voltammetry (DPV) of synthesized Au₂₅Fc, Au₁₄₄Fc, and Au₂₂₅Fc is shown in Figure 3.1 A-C. Patterns of quantized double layer charging, with uniformly spaced one-electron DPV peaks, are observed for Au₂₂₅⁵¹ and Au₁₄₄⁷⁰ and Au₂₅²⁶⁸ nanoparticles display their known HOMO level doublet of peaks. Superimposed on this characteristic nanoparticle voltammetry is the larger Fc^{+1/0} redox wave for the ferrocenated nanoparticles Au₂₂₅Fc, Au₁₄₄Fc, and Au₂₅Fc.

The number of ferrocene-containing ligands per nanoparticle was determined from the difference in charge passed in bulk electrolyses (BE) at potentials spanning the Fc^{+1/0} wave. (BE of ferrocenated Au MPCs was done under Ar in a fine frit-separated three-compartment cell using a Pine WaveNow Potentiostat and Pt gauze working and reference electrodes in cell compartment #1 and Pt counter electrode in compartment #3. Compartment #1 contained ~ 10 mL of 1 mM ferrocenated Au nanoparticles in CH₂Cl₂ and 50 mM Bu₄NClO₄ supporting

electrolyte; compartments #2 and 3 contained only 50 mM Bu₄NClO₄/CH₂Cl₂. The electrolysis was halted when the electrolysis current dropped to ~ 1% of its initial value. The overlap of the redox peak for the Au₂₅^{+1/0} core with that for Fc^{+1/0} was avoided by using double the charge under the more positive half of its' peak.

3.3.2 Preparation of Mixed-Valent Au MPCs.

Bulk electrolysis was used to prepare mixed valent nanoparticle samples of known ca. 1:1 mole ratio for Au₂₂₅^{+1/0}, Au₂₂₅Fc^{+1/0}, Au₁₄₄Fc^{+1/0}, and Au₂₅Fc^{+1/0}. Mixed-valent Au₁₄₄^{+1/0}, Au₂₅^{+1/0}, and Au₂₅^{0/-1} samples were similarly prepared.¹¹⁸ Mixed valency of non-ferrocenated Au nanoparticles Au₂₂₅^{+1/0}, Au₁₄₄^{+1/0}, Au₂₅^{+1/0}, and Au₂₅^{0/-1} refers to the charge state of the nanoparticle core. Electrolysis potentials (E_{Elec}) were chosen based on the Nernst equation^{63,83}

$$E_{Elec} - E^{Z+1/Z} = 0.059 \log \frac{[MPC^{Z+1}]}{[MPC^Z]} \quad (3.3)$$

where $E^{Z+1/Z}$ was determined by DPV of the Au MPCs. For the ferrocenated Au nanoparticles Au₂₂₅Fc, Au₁₄₄Fc, and Au₂₅Fc, mixed-valency refers to the charge state of the nanoparticle's ferrocene ligand(s) and E_{Elec} was chosen with reference to the DPV-determined redox potential wave $E^{+1/0}$ of the ferrocene couple

$$E_{Elec} - E^{+1/0} = 0.059 \log \frac{[AuFc^{+1}]}{[AuFc^0]} \quad (3.4)$$

where AuFc^{+1/0} refers to the Fc^{+1/0} redox wave of the ferrocene-containing Au₂₂₅, Au₁₄₄, or Au₂₅ nanoparticle. Following bulk electrolysis, the nanoparticle solution was degassed again and its open circuit rest potential (vs. Ag/AgCl) measured at a clean Pt wire (Keithley Instruments 610C solid-state electrometer, input impedance > 10⁸ MΩ). The actual MPC^{Z+1/Z} or AuFc^{+1/0} population ratios were calculated from the rest potential after BE and the DPV-determined formal potentials according to Eqn. 3 (non-ferrocenated samples) or 4 (ferrocenated samples).

Mixed-valent samples of Au₂₂₅, Au₂₂₅Fc, Au₁₄₄, and Au₁₄₄Fc MPCs were washed twice with CH₃CN following bulk electrolysis to remove excess electrolyte. Au₂₅ and Au₂₅Fc were washed twice with CH₃OH. The wash steps did not alter the open circuit potentials.

3.3.3 Low Temperature Electronic Conductivities of Solid-State Au MPC Films.

Temperatures of Au MPC films were controlled using a Janus VPF 100 liquid nitrogen cryostat and Lakeshore 331S temperature controller. IDAs bearing dropcast nanoparticle films were secured to the heat-conducting sample stage of the cryostat using double sided tape. The cryostat chamber was evacuated overnight using an Edwards RV8 rotary vane pump, which is required for proper function of the temperature controls and to ensure complete drying of the MPC films. The cryostat cooling chamber was filled with liquid nitrogen and allowed to cool to the minimum temperature (~75 K) prior to initiation of film electronic conductivities.

Measurements were done using a home-built two-electrode circuit designed for applying a voltage ramp and measuring currents as low as 10⁻¹⁰ A (controlled by LabView software). Capacitance was minimized by connecting the circuit directly to the cryostat. Electronic conductivities were calculated from the slopes of linear current-potential plots in a triangular potential scan between 0.25 and -0.25 V with 0 V initial and final voltages. The 10 V/s scan rate was aimed at avoiding electrostatic counterion migration within the film as was avoidance of temperatures above 300 K. Conductivity scans were performed at temperature intervals between 2 and 10 K as the IDA electrode temperature was raised in a controlled manner from 77 to 300 K.

The mixed valent MPC film's electronic conductivity, σ_{EL} , was calculated from the slopes of the current-potential plots according to^{116,117}

$$\sigma_{EL} = \left(\frac{d}{A_{Total}} \right) \frac{\Delta i}{\Delta E} \quad (3.5)$$

where d is IDA gap, A_{Total} is area of the walls (A_{Finger}) of facing parallel plate finger electrodes, of height taken as the maximum conductive MPC film thickness (*ca.* 1 μm), and length equal to the finger length times $N - 1$ where N is the total number of fingers (50). Note that the current of each interior finger is double that of an end finger. The ratio $\frac{d}{A_{Total}}$ comprises the geometric cell constant, C_{Cell} , which for the IDAs used for Au₂₂₅ and Au₁₄₄ films was 1.021 cm^{-1} and for Au₂₅ films was 0.685 cm^{-1} .

The conductivities of the Au₂₅Fc films were too low to be measured with the home-built circuit, so the resistance at 298 K was measured with a Keithley Instruments 610C solid-state electrometer and multiplied by C_{Cell} to estimate values of the same form as σ_{EL} for comparison with other films.

3.3.4 Electronic Conductivity of MPC Films from 77 to 300 K.

Electronic conductivity (σ_{EL}) results for the Au MPC films from 77 to 300 K are presented in Figures 3.2 and 3.3 as Arrhenius plots. Two regimes of behavior can be observed. At higher temperatures conductivities reflect a thermally activated ET process and strongly temperature-dependent rates. At the lowest temperatures, the ET conductivity becomes temperature-independent, characteristic of electron tunneling.¹¹⁸ In the thermally activated ET region, the Arrhenius plot is linear such that⁴

$$\ln(\sigma_{EL}) = \frac{-E_A}{RT} - r_0\beta + \ln \sigma_0 \quad (3.6)$$

where β (cm^{-1}) is an electronic coupling term⁴ for ET tunneling through the MPC ligand shell, and r_0 (cm) is the average edge-to-edge distance between neighboring MPC Au cores. The y-intercept represents an infinite-temperature electronic conductivity.^{4,116}

Like previous observations¹¹⁸ for non-ferrocenated, mixed-valent Au₁₄₄ and Au₂₅, the transition between thermally activated and tunneling ET behavior for mixed-valent, Fc-Au MPCs

is gradual (Figures 3.2 and 3.3). The total current measured at any given temperature represents the summation of currents arising from all ET processes.¹³⁷ In the flattened, lowest temperature regions of the Arrhenius plots of Figures 3.2 and 3.3, the ET conductivity is solely through the mechanism of tunneling. Tunneling currents dominate at low temperatures as energy-activated states are emptied, thermal energy is depleted and electron hopping diminished. At higher temperatures, in the thermally activated region, the electron hopping mechanism dominates, and tunneling current becomes a minor contributor, retaining its small value regardless of temperature.

It was previously found^{56,118} in non-ferrocenated Au MPCs, that the magnitudes of both thermally activated electron hopping and electron tunneling currents depend on the mixed-valency of the particle and on the core size of the particle, those for Au₁₄₄ being larger than Au₂₅ (see Figure B.1 in Appendix B). The current study further reveals the substantial effects of mixed-valent ferrocene-containing ligands on the nanoparticle ET behavior. The values of electron hopping conductivity σ_{EL} for mixed valent ferrocene-containing nanoparticles are substantially smaller than those of corresponding non-ferrocenated mixed-valent nanoparticles. Obliging ET to occur through the $\text{Fc}^{+1/0}$ redox couple seems to help drive the ET behavior into the tunneling regime, suggesting that the ferrocene sites act as kinetic pot-holes (traps) in the serial electron hopping process.

Consistent with this suggestion, Figure 3.2 shows that the electron tunneling current varies with the number of ferrocenes in the nanoparticle ligand shell. See also the Au₁₄₄Fc data in Figure 3.3 and in data for Au₂₅Fc (Table 3.2). Conversely, activated electron transfers are little changed (e.g., E_A) by the presence or amount of ferrocene ligands, primarily depending on

core size. This suggests that the ET conductivity depends on contribution from the conductivity of the Au core as well as the mixed-valent ferrocene sites.

Translation of the ET conductivity data into rate constants requires a model for average electron hopping distances (δ) in the mixed valent film. Solid-state densities of nanoparticle samples were determined via pycnometry (Table 3.1), and core-to-core edge separations (δ) were calculated according to

$$\delta_{Au_{25}} = 2r_{Core} + l_{Eff} = 2 \left(\frac{(0.7)(10^3)}{\frac{4}{3}\pi C_{Film} N_{Avo}} \right)^{\frac{1}{3}} \quad (3.7)$$

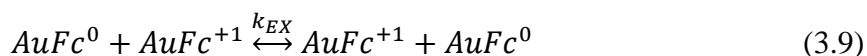
Note that the nanoparticle separation δ is increased for ferrocenated Au₂₂₅ and Au₁₄₄ nanoparticle films but not measurably for Au₂₅ films. Using pycnometric distances to estimate δ for Au₁₄₄ and Au₂₅ rather than earlier used crystal structure,⁹ TEM,^{116,271} and/or DFT⁷³ calculations, favored since the solid-state density includes all factors affecting the average distance between particles, including packing irregularities in the dropcast films. More importantly, using a single method for calculating δ permits more direct comparison between ferrocenated and the previously reported non-ferrocenated Au MPC films.

The density information is used with the electron conductivity information in Table 3.2, where bimolecular electron self-exchange rate constants (k_{EX}) for current and previously studied¹⁸ Au MPC films are compared. Translating density and electronic conductivity into bimolecular electron self-exchange rate constants (k_{EX}) is based on assumption of a cubic lattice film structure (as in previous studies)^{56,92,116-118}

$$k_{EX} = \frac{6(10^3)RT\sigma_{EL}}{F^2\delta^2[MPC^{Z+1}][MPC^Z]} \quad (3.8)$$

where δ is the core edge to core edge separation (cm), and $[MPC^{Z+1}]$ and $[MPC^Z]$ are calculated from the Nernst equation.

We have shown previously¹¹⁸ that k_{EX} for $\text{Au}_{144}^{+1/0}$, $\text{Au}_{25}^{0/-1}$, and $\text{Au}_{25}^{+1/0}$ films is maximized when $[\text{MPC}^{Z+1}] = [\text{MPC}^Z]$. A further aim here was to determine whether adding ferrocenes to the nanoparticle ligand shell could direct ET to occur via the $\text{Fc}^{+1/0}$ redox couple. The data show that indeed the mechanism of ET in mixed-valent, ferrocenated MPCs differs from non-ferrocenated MPCs. Converting the ferrocene-containing nanoparticle film in a mixed-valent state (with regards to $\text{Fc}^{+1/0}$) appears to allow ET via a ferrocene-dependent mechanism such that



where $\text{AuFc}^{+1/0}$ refers to the $\text{Fc}^{+1/0}$ redox wave of the ferrocene-containing Au_{225} , Au_{144} , or Au_{25} nanoparticle. The expression for k_{EX} that follows is also bimolecular,

$$k_{EX} = \frac{6(10^3)RT\sigma_{EL}}{F^2\delta^2[\text{AuFc}^{+1}][\text{AuFc}^0]} \quad (3.10)$$

where $[\text{AuFc}^{+1}]$ and $[\text{AuFc}^0]$ are also calculated from the Nernst equation. Evidence for this mechanism involving ferrocene is found in the dependence—for all three core sizes studied, 225, 144, and 25—of ET rate constant on the number of ferrocenes present on the nanoparticle. For instance, the rate constant of ET in $\text{Au}_{225}\text{Fc}_7$ is larger by over an order of magnitude than $\text{Au}_{225}\text{Fc}_2$. The increase in k_{EX} with number of ferrocenes present in the ligand shell suggests two possibilities—that ET is accelerated by the higher probability of adjacency and favorable orbital overlap^{131,269} of ferrocenes on neighboring nanoparticles. Multiple ET in solutions¹² of hexanethiolate-protected Au nanoparticles has been previously observed to increase with larger populations of ferrocenes in their ligand shells. Rotational diffusion would be slowed in the solid state but multiple ferrocene sites equally distributed between Fc^{+1} and Fc^0 should still permit multiple ET pathways between neighboring particles. Since the electron transfer E_A does not change with the numbers of ferrocene-containing ligands, the latter explanation is more

likely. The core still plays a role in the ET process, since the E_A for electron transfer responds to the core size of the particle. It is unfortunately not possible to independently the mixed-valency of the MPC core and the $\text{Fc}^{+1/0}$ redox couple.

In summary, we show that $\text{Fc}^{+1/0}$ electron transfer rates in mixed valent films of Au_{225}Fc , Au_{25}Fc and Au_{144}Fc nanoparticles can be observed over a complete range of thermal activation of electron hopping to temperature-independent rates of ET at lowered temperatures. The ET rates at lowered temperatures mimic the trend at ambient temperatures and increase with degree of ferrocenation. By adding ferrocene to the ligand shell, the mechanism of ET is likely altered, from following the form of Equation 1 to that of Equation 8, thus varying both the thermally activated electron hopping and tunneling current in response to an applied a potential bias across the film. The degree of ferrocenation also impacts the rate of ET.

3.4 Acknowledgements

The authors thank Drs. Collin McKinney and Matt Verber of the UNC Electronics Facility for conductivity circuit design and Dr. Robert Geil of CHANL for microfabricating IDA electrodes. This work was supported by the Office of Naval Research. Tessa Carducci acknowledges support from a National Defense Science & Engineering Graduate (NDSEG) Fellowship, from the Department of Defense.

3.5 Tables and figures

Table 3.1. Densities obtained through pycnometry and core-to-core edge separation distances

(δ) calculated for ferrocenated and non-ferrocenated Au MPC solid-state films.

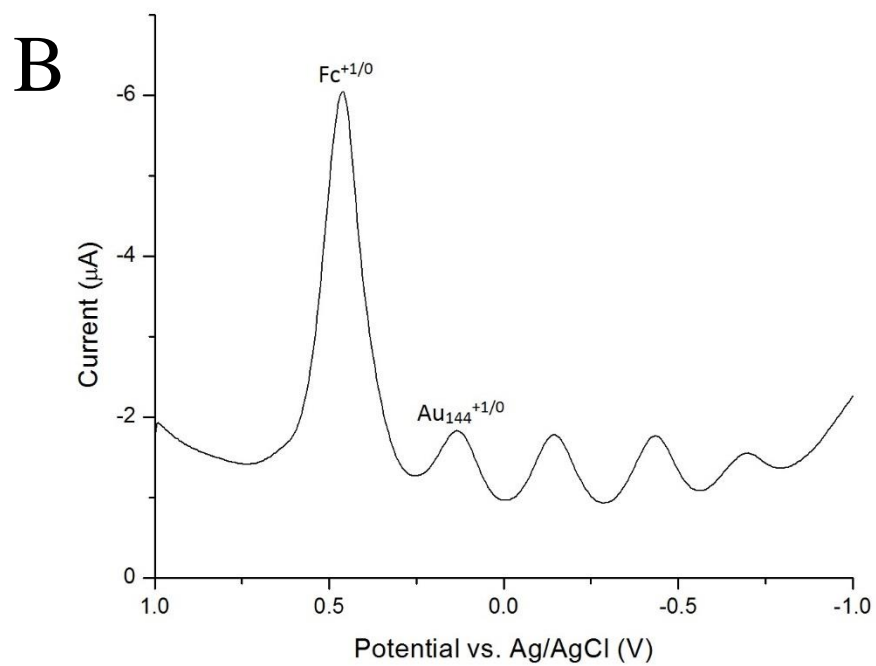
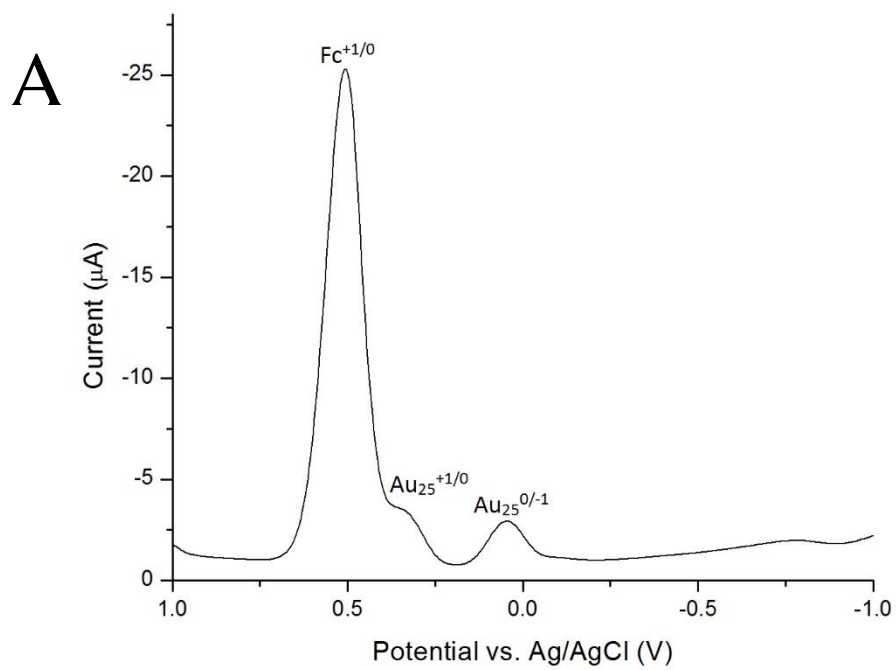
MPC	Density (g mL ⁻¹)	Density (mM)	δ (nm)
Au ₂₂₅	4.51	84.4	2.97
Au ₂₂₅ Fc ₂	4.25	79.6	3.03
Au ₁₄₄	3.18	89.8	2.91
Au ₁₄₄ Fc ₇	3.08	84.0	2.98
Au ₂₅	1.78	22.7	2.14
Au ₂₅ Fc ₃	1.90	22.8	2.14

Table 3.2. Thermally-activated ET parameters: Activation energy barriers (E_A), electron hopping conductivities (σ_{EL}), and self-exchange rate constant (k_{EX}) at 298 K of mixed valent, ferrocenated Au MPC solid-state films. Data points represent the average of three different films having the same mixed valent composition.

MPC	[MPC ^{Z+1}] or [Fc] ⁺¹ (%)	^a E_A (eV)	σ_{EL} ($\Omega^{-1} \text{ cm}^{-1}$)	k_{EX} (M s^{-1})
Au ₂₂₅	50	0.06 ± 0.007	$(8.0 \pm 6.3) \times 10^{-6}$	$(8.0 \pm 6.2) \times 10^7$
Au ₂₂₅ Fc ₇	46	0.063 ± 0.004	$(3.7 \pm 1.8) \times 10^{-6}$	$(4.0 \pm 1.7) \times 10^7$
Au ₂₂₅ Fc ₂	43	0.08 ± 0.04	$(2.0 \pm 0.8) \times 10^{-7}$	$(2.2 \pm 0.9) \times 10^6$
Au ₁₄₄	55	0.17 ± 0.02	$(5.9 \pm 0.9) \times 10^{-6}$	$(5.6 \pm 0.9) \times 10^7$
Au ₁₄₄ Fc ₇	52	0.17 ± 0.02	$(1.9 \pm 0.3) \times 10^{-7}$	$(1.9 \pm 0.3) \times 10^6$
Au ₁₄₄ Fc ₂	76	0.16 ± 0.06	$(3.8 \pm 1.0) \times 10^{-8}$	$(6.0 \pm 1.6) \times 10^5$
Au ₂₅ ^{0/-1}	53	0.38 ± 0.03	$(6.3 \pm 2.2) \times 10^{-7}$	$(3.8 \pm 1.4) \times 10^6$
Au ₂₅ ^{+1/0}	45	0.34 ± 0.09	$(6.4 \pm 1.2) \times 10^{-8}$	$(3.9 \pm 0.7) \times 10^5$
Au ₂₅ Fc ₃	50	Could not quantify	^b $(1.3 \pm 0.8) \times 10^{-10}$	$(5.0 \pm 3.0) \times 10^2$
Au ₂₅ Fc ₁	52	Could not quantify	^b $(1.4 \pm 0.8) \times 10^{-10}$	$(3.7 \pm 2.2) \times 10^2$

^a Data over the temperature range 265 – 300 K was linearized to determine E_A .

^b For these particularly highly resistive films, the resistance at 298 K was measured with an electrometer, and σ_{EL} was calculated by multiplying the value of resistance by the cell constant of the IDA, C .



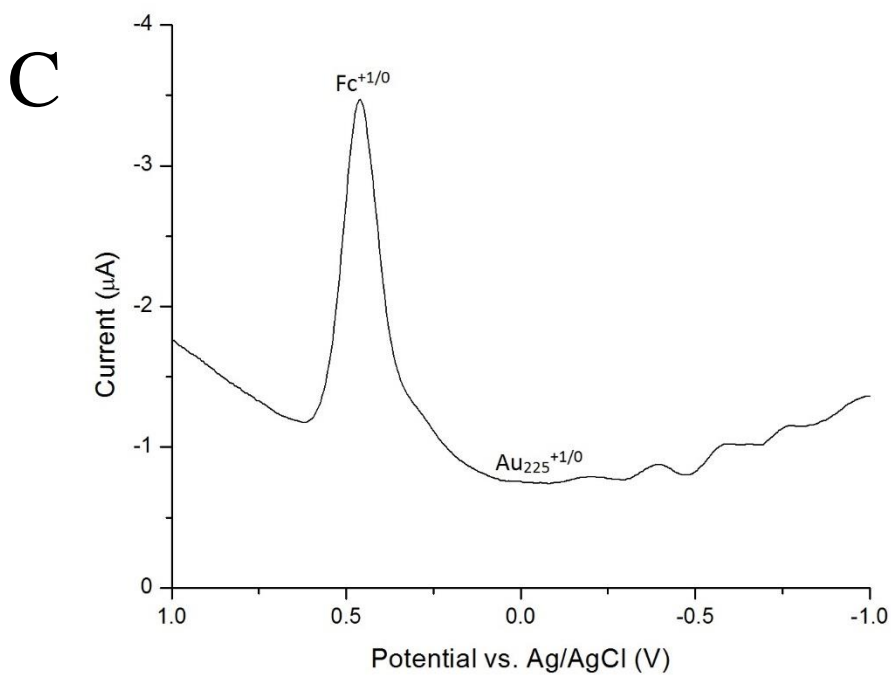


Figure 3.1. Differential pulse voltammetry (DPV) of ferrocenated Au MPCs: $\sim 1\text{mM}$ (A) ferrocenated Au_{25} , (B) ferrocenated Au_{144} or (C) ferrocenated Au_{225} in 50 mM $\text{Bu}_4\text{NClO}_4/\text{CH}_2\text{Cl}_2$ at 0.020 cm^2 Pt disk. Redox potentials of interest are indicated. Data taken with a Pine WaveNano potentiostat.

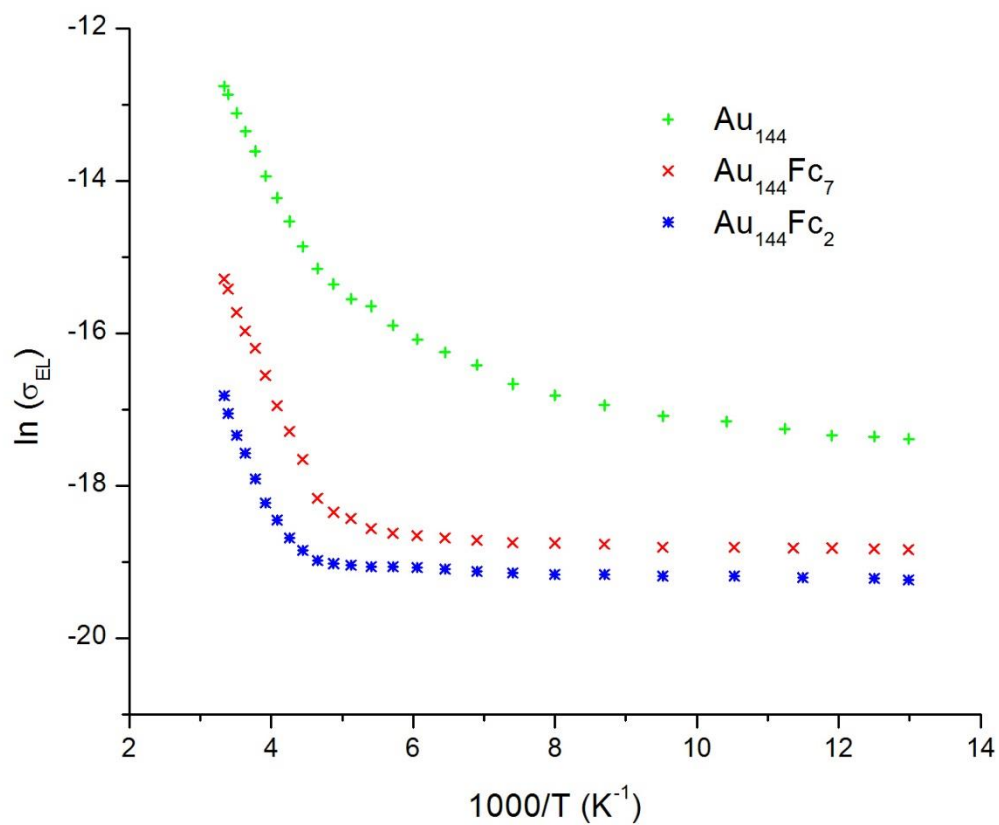


Figure 3.2. Arrhenius plots of solid-state ferrocenated or nonferrocenated Au_{144} MPC films containing mixed valent proportions of the $\text{MPC}^{+1/0}$ (non-ferrocenated) or $\text{Fc}^{1+/0}$ (ferrocenated) charge states.

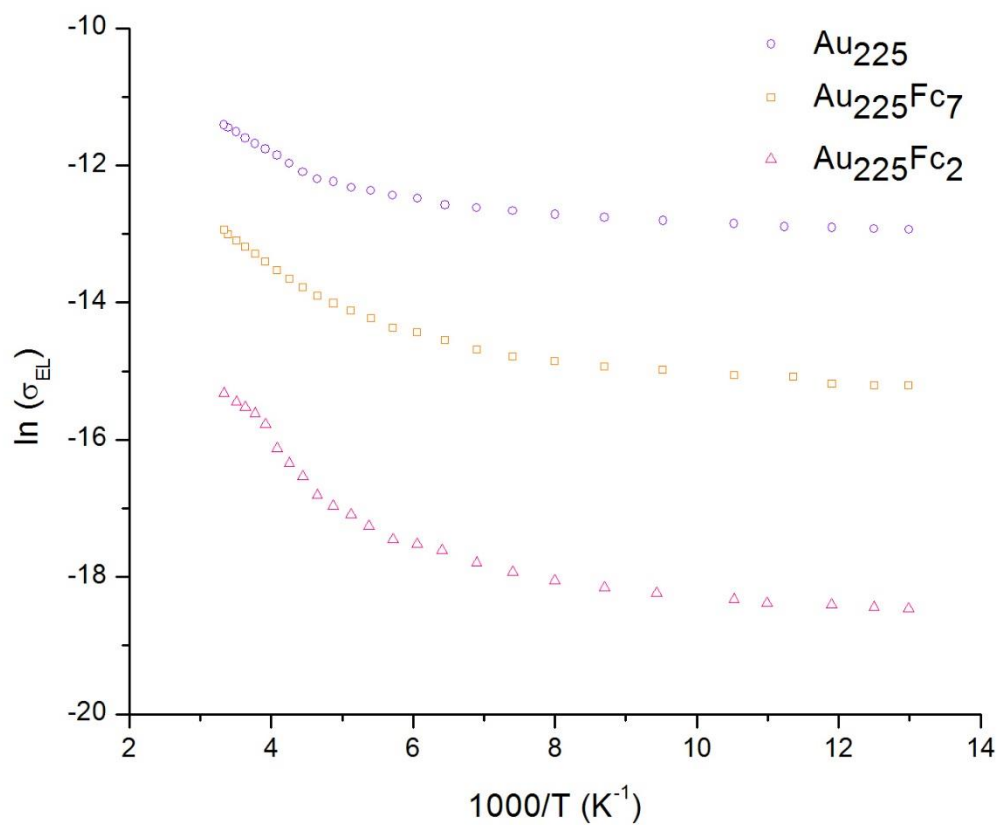


Figure 3.3. Arrhenius plots of solid-state ferrocenated or nonferrocenated Au₂₂₅ MPC films containing mixed valent proportions of the MPC^{+1/0} (non-ferrocenated) or Fc^{1+/0} (ferrocenated) charge states.

CHAPTER 4: ELECTRONIC CONDUCTIVITY OF FILMS OF ELECTROFLOCCULATED ~2 NM IRIIDIUM OXIDE NANOPARTICLES⁴

4.1 Introduction

There is substantial literature on the potential-dependent conductivity of so-called “conducting polymers”, e.g., polypyrroles and polyanilines.²⁷³⁻²⁸¹ The potential dependence of the conductivity of films of very small nanoparticles (NPs) has, in contrast, not been widely explored. Nanoscale materials often have different electrochemical properties than their parent bulk materials. Gold nanoparticles are an excellent example; their electrochemical properties, optical properties, and conductivity differ dramatically from bulk gold.^{12,37}

Ir^{IV}O_x NPs are an interesting material owing in part to their high activity as electrocatalysts for water oxidation. The nanoparticles, with weakly ligating counterions (e.g., phosphate), can be deposited by electroflocculation (without concurrent aggregation) as very thin films from the basic media in which they are hydrolytically prepared.²³⁶ Electrodes coated with their films exhibit overpotentials²³⁴ for the water oxidation reaction that are among the lowest known. Another interesting aspect of IrO_x NPs is that all of the Ir^{IV} sites in an oxide nanoparticle, whether in a film or in solution,^{234,235} can be oxidized to Ir^V and all can be reduced to Ir^{III}, while exhibiting variations of formal potential signaling concurrent proton transfers.²³⁵

⁴ This chapter is reproduced in part with permission from Chow, K.-F.; Carducci, T. M.; Murray, R. W. *Journal of the American Chemical Society* **2014**, 136, 3385. Copyright 2014 American Chemical Society.

We have also reported previously on voltammetry of IrO_x NPs anchored atop self-assembled monolayers.²³⁷

The current study describes how the electronic conductivity of IrO_x films, composed of the 2 nm-diameter IrO_x NPs, changes upon oxidation of the film to the Ir^{IV/V}O_x state and reduction to the Ir^{III/IV}O_x state.

4.2 Experimental

Figure 4.1 a shows an image of a dual Pt working electrode used in this experiment. The electrode was fabricated by sealing two 300 µm-diameter Pt wires in a two compartment glass capillary such that the distance between the edges of the two electrodes is ca. 300 µm apart. An electroflocculated film of IrO_x nanoparticles was formed on the dual electrode by applying 1.2 V vs. Ag/AgCl for 90 min in an IrO_x NP solution. As the film grew thicker, the two electrodes became covered and connected to each other by the film. The electrode assembly was then transferred to an electrolyte solution composed of 0.1 M NaOH and 2.0 M NaNO₃ for conductivity measurements, using the four electrode configuration²⁸² shown in Figure 4.1 b. The two IrO_x NP-coated Pt working electrodes were biased vs. one another at a constant potential difference of 20 mV. The potential of one of them was controlled with respect to a Ag/AgCl reference electrode.

Expressing film conductivities by approximating the electrode configuration as a parallel plate cell is highly approximate, but does facilitate expressing changes in *apparent* conductivity induced by redox state or pH changes. We express the apparent conductivities as

$$\sigma_{APP} = \frac{di}{AV} \quad (4.1)$$

where d is distance (cm) between neighbor edges of the two exposed disks in Figure 4.1, i is current (amperes) flowing between them, A is area in cm^2 of each disk electrode, and V is the imposed 20 mV potential difference between them. The two disk electrodes are labelled “source” and “drain”.

Cyclic voltammetry was performed on an IrO_x electroflocculated onto a 2 mm (dia.) Pt disk electrode (Figure 4.2 a). The film has a dark purple-blue color. The CV covers three film oxidation states: the film is Ir(III) from -0.6 to -0.4 V, Ir(III/IV) from -0.4 to -0.1 V, and Ir(IV/V) from -0.1 to 0.4 V vs. Ag/AgCl.

4.3 Results and discussion

In a static measurement of the conductivity of the solvent-wetted IrO_x film at different potentials, the source electrode was held at a constant potential with respect to a Ag/AgCl reference electrode, with a 20 mV bias applied to the drain electrode. The current (Figure 4.2 b, points) between the two electrodes was measured after reaching a steady state value (ca. 5 min.). The apparent conductivity, σ_{APP} , of the solvent-wetted IrO_x film at different potentials (black points) is given in Figure 4.2 c. The conductivity of the film in the Ir(III) state is ca. $5 \times 10^{-6} \text{ S cm}^{-1}$ and increases to ca. $1.5 \times 10^{-5} \text{ S cm}^{-1}$ in the Ir(III/IV) state. When the film is oxidized to the Ir(IV/V) state, the apparent conductivity of the film increases dramatically, to ca. $1.5 \times 10^{-2} \text{ S cm}^{-1}$. There is a four order of magnitude increase in conductivity between the oxidized and reduced forms of the film; the two redox potentials cross the band edge energy.²⁸³ The film is changed to its highly conductive state over the potential interval of 0.1 to 0.4 V vs. Ag/AgCl.

Figures 4.2 b and c (solid line) show a dynamic conductivity measurement on the solvent-wetted IrO_x film, in which the electrode potentials were swept at 0.1 mV/s between -0.6 and 0.4 V vs. Ag/AgCl (again with a 20.0 mV bias between them). Figure 4.2 b shows the

recorded drain current and Figure 4.2 c shows the corresponding conductivity values. These two experiments together show a clear transition between the resistive and conductive regions of the IrO_x NP film. The IrO_x NP film is stable at potentials ca. 0.4 V vs. Ag/AgCl, but tends to dislodge from the electrode upon scanning to more positive potentials.

The electronic conductivity of an IrO_x film was also measured in the dry state. In this experiment, the oxidation state of the film was first set in the electrolyte solution by applying the same potential to both source and drain electrodes. The electrode was then removed from the solution and dried under a gentle flow of Ar. The bias between the two electrodes was scanned between 0.1 to -0.1 V at 10 V/s, producing a steady state linear *i*-*V* plot, where the slope expresses the film conductivity. When the film oxidation state was set in the reduced state (at -0.6 V vs. Ag/AgCl), the measured dry film conductivity was $1.5 \times 10^{-6} \text{ S cm}^{-1}$, and when the film oxidation state was set at 0.3 V vs. Ag/AgCl, the conductivity was $1.1 \times 10^{-2} \text{ S cm}^{-1}$. These values are close to the conductivity values that were obtained in the above solvent wetted measurements.

The distance between the two working electrodes in the above experiment is much larger than the micron-scale spacings used in interdigitated array (IDA) electrodes. We found that IDA electrodes were not readily suited for the IrO_x film measurements. The positive potentials used for the IrO_x electroflocculation (and possibly the presence of chloride ions in the IrO_x NP solutions) tended to cause detachment of the IDA electrode fingers from the substrate surface. The dual Pt electrode of Figure 4.1, while less elegant than IDA electrodes, withstands the abusive experimental conditions, is easily fabricated, and can be cleaned and used repetitively.

We note that the chosen scan rate used in the dynamic solvent-wetted film conductivity measurements is very low (0.1 mV/s) relative to other film conductivity experiments^{279,280} (for

example, 20 mV/s). This was because of the long distance between the source and drain electrodes, and was the impetus for seeking steady state conductivities.

The overall shape of the Figure 4.2 a cyclic voltammogram differs substantially from that of an ideally behaved redox film; the reduction peak is flattened relative to the oxidation peak, and the capacitive current in the oxidized region is quite large. These observations are consistent with the cyclic voltammograms of conducting polymers like polypyrrole and polythiophene.²⁷⁷ These materials are conductors in the oxidized form and poor conductors in the reduced form. While chemically quite different, the IrO_x films share these same features with those traditional materials. The oxidized IrO_x NP film is quite conductive (from 0.1 to 0.4 V vs. Ag/AgCl), whereas its conductivity is diminished by ca. 10⁴ when the film is reduced. To our knowledge, this report is the first experimental demonstration of < 2 nm IrO_x NPs having such potential-dependent electronic conductivity.

4.4 Acknowledgements

This research was supported in part by the Office of Naval Research and the National Science Foundation. T.M.C. acknowledges support from a National Defense Science & Engineering Graduate (NDSEG) Fellowship from the Department of Defense.

4.5 Tables and figures

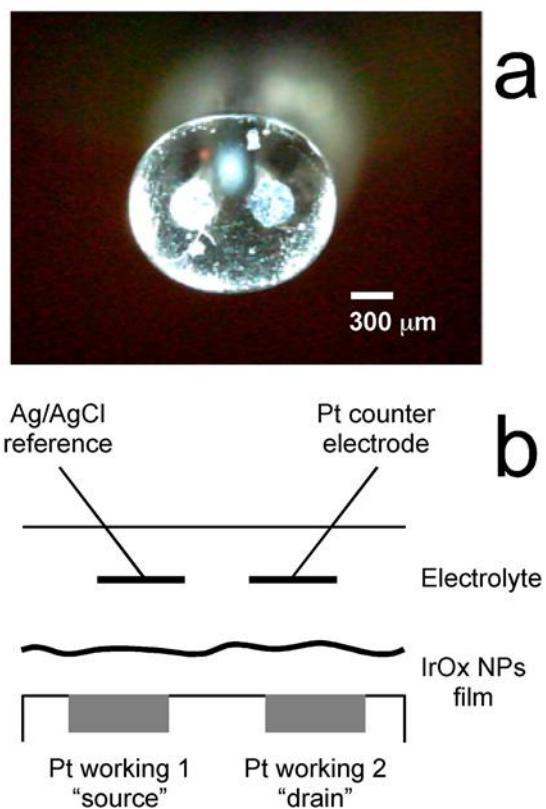


Figure 4.1. Image of a dual Pt working electrode and schematic four electrode configuration used for conductivity measurements of a IrOx NP film.

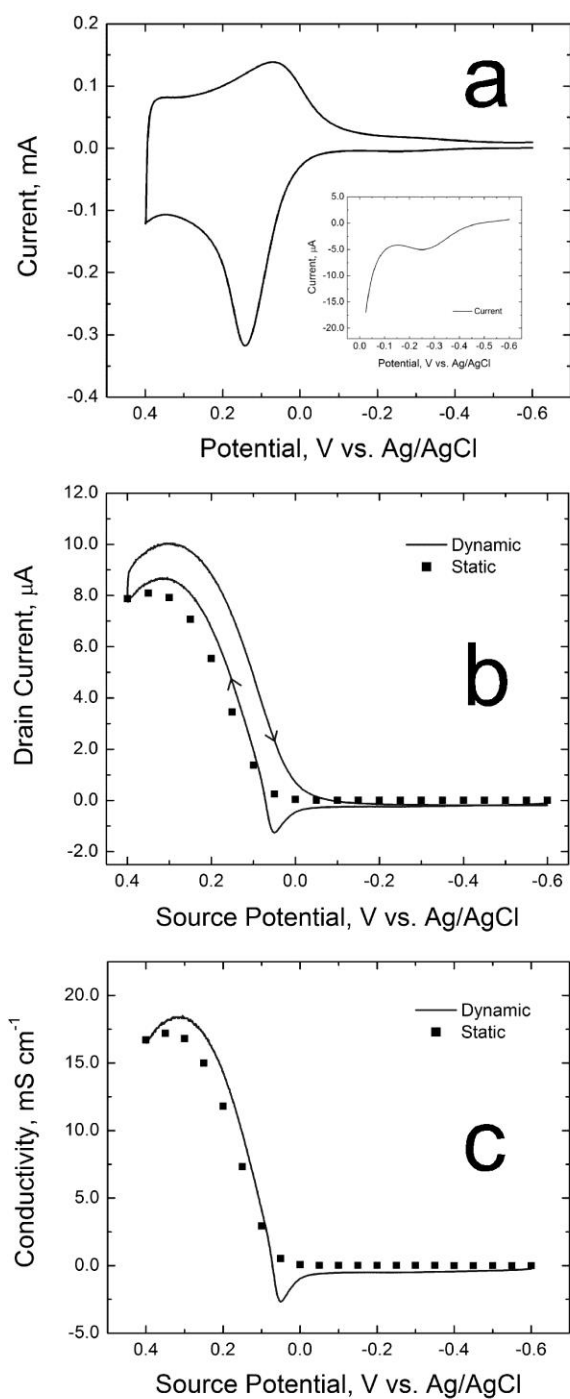
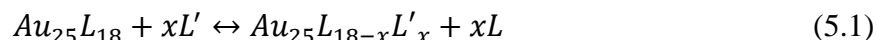


Figure 4.2. (a) CV of an IrOx NP film on a Pt electrode surface. (b) Current at electrode 1 (“drain”) vs potential of electrode 2 (“source”). (c) Potential-dependent apparent conductivity of the IrOx film

CHAPTER 5: INVOLVEMENT OF CHARGE TRANSFER IN LIGAND EXCHANGE REACTIONS OF Au₂₅ MONOLAYER PROTECTED CLUSTERS⁵

5.1 Introduction

Au monolayer-protected clusters in the very small size regime (< 2 nm) exhibit molecule-like characteristics, such as a HOMO-LUMO gap⁷⁶ or paramagnetism.²⁴⁷ The crystal structures of the molecule-like cluster Au₂₅(PhC₂S)₁₈⁹ and others³⁸ have been elucidated and several catalytic and sensing roles²⁸⁴ identified, providing impetus to seek complete understanding of their structure-property relationships. In our previous studies,^{53,60} ligand exchanges of Au₂₅(PhC₂S)₁₈ were found to be rapid and follow an associative mechanism, being first-order in nanoparticle and in incoming ligand L', as in



Introduction of electron withdrawing ligands such as 4-bromobenzenethiol (BrPhSH) into the nanoparticle ligand shell produces a shift of the Au₂₅^{1+/0} and Au₂₅^{0/1-} nanoparticle redox waves to more positive potentials. However, while previous studies explored consequences of ligand exchanges on Au₂₅ MPC electrochemical properties, many aspects of the exchange remain incompletely understood. The present study seeks to determine the dependence of the initial rate

⁵ This chapter is reproduced in part with permission from the *Journal of Physical Chemistry Letters*, submitted for publication. Unpublished work copyright 2015 American Chemical Society.

of ligand exchange on nanoparticles charge state and the role(s) the nanoparticle's electronics properties in the mechanism.

We are also interested in gaining a better understanding of the structural and property differences between thiolate-protected Au MPCs and those containing ligands with a higher-order chalcogen linker, e.g. Se or Te. Recent literature has produced examples of solubility²⁴⁶ and stability²⁴⁴ properties and of unique structures^{245,285-287} that are imparted by using alkyl/arene-selenolates and -tellurates as protecting ligands. There are also reports of selenolate-protected Ag clusters.^{288,289} These provide impetus for unraveling how such materials possibly differ from those of thiolate-protected Au MPCs. That the Se-Au bond is more covalent than S-Au would imply a lessening of charge transfer between the metal and ligands.²⁴⁵ The elucidation of the chemistry of these clusters is hampered by synthetic difficulties caused by the ligand readily oxidizing in air. Here, we seek to minimize the ligand oxidation problem by examining the dynamics of partial (rather than complete) ligand exchange, e.g. only a few thiolate ligands are replaced by selenolate ligands, and propose a mechanistic basis for the observed differences.

5.2 Experimental

Highly monodisperse $\text{Au}_{25}(\text{PhC}_2\text{S})_{18}$ was synthesized and known charge states (i.e. 50% Au_{25}^{+1} , 50% Au_{25}^0) were prepared as reported previously^{118,290}. All ^1H NMR measurements were made using a Bruker 500 MHz spectrometer. About 20 mg of Au_{25} MPCs were dissolved in ca. 1 mL of CD_2Cl_2 containing a known amount of acetonitrile (serving as an internal standard), and the solution was transferred into an NMR tube. The temperature was equilibrated using a liquid nitrogen cooling apparatus and shims optimized. Temperatures of the NMR experiments were calibrated using pure methanol using a delta ppm calculation. The incoming exchange ligands, thiophenol (PhSH), benzeneselenol (PhSeH), or 4-bromobenzenethiol (BrPhSH) were

added in a 2:1 molar ratio with respect to the existing nanoparticle ligands (e.g. 36:1 with respect to NP concentration) and mixed. The spectrometer was re-shimmed following addition of the exchange ligand. Repetitive spectral scans were made at programmed time intervals over the course of 4-5 hours. (NMR spectrum acquisition conditions were $D1 = 1$ s, ppm range = 20, acquisition time = 3.3 s). The resulting spectra were processed in MestreNova, including automatic phase correction, manual cubic splines baseline correction, and integration.

The area of the methylene quartet at ~ 2.8 ppm (relative to a known amount of acetonitrile standard added, 1.93 ppm Figure 5.1.) of the HS- CH_2 -CH₂Ph liberated from the Au₂₅ nanoparticle during ligand exchange was used to quantify the extent of ligand exchange.⁶⁰ Plots of the reaction progress over time shows an initial linear growth of the quartet peak area, then gradual rollover to a plateau region (Figure 5.2). The average slopes from the first ten data points (ca. 10 min.) represent the initial ligand exchange reaction rate; from these slopes were calculated the pseudo-first order rate constant using plots of the natural log of the fraction of unexchanged ligand versus time (Figure 5.3). The linear fits were satisfactory ($r^2 > 0.9$), and second-order rate constants (k , $\text{M}^{-1} \text{s}^{-1}$) result from dividing the pseudo-first order rate constant (s^{-1}) by the incoming ligand concentration.

5.3 Results and Discussion

Table 5.1 shows the effect of Au₂₅ nanoparticle charge state on the initial rate of its phenylethanethiolate ligand exchange with an electron-withdrawing ligand (p-bromothiophenol). By using data from early in the exchange reaction, appreciable positive shifts of the nanoparticle 0/−1 and +1/0 formal redox potentials^{53,60} are avoided, so that the observed differences in rate are attributable to the established charge state of the nanoparticle. Previously, density functional theory charge analysis⁶⁰ suggested charge is transferred inside the semirings of the ligands,

mostly from nearest-neighbor atoms. Here, a depletion of electron density in the semirings, in going from an entirely -1 to an entirely +1 nanoparticle, is seen to retard the rate of exchange when the incoming ligand has an electron-withdrawing substituent. Analogous effects are observed in comparing electron transfer rates of $\text{Au}_{25}^{+1/0}$ and $\text{Au}_{25}^{-1/0}$ redox couples in electron transfer reactions were previously observed, as rate was again lower in the more charge-depleted clusters^{58,118}. Together with the present data, it is evident that a rate-determining step of the ligand exchange reaction involves at least partial transfer of charge from the incoming ligand to the semirings of the Au_{25} molecule.

Table 5.2 shows the effect of temperature on the rate constants for ligand exchanges of benzene-thiol and benzene-selenol with $\text{Au}_{25}(\text{C}_2\text{Ph})_{18}$ MPCs having a -1 charge state. The -10 and 25 °C temperature range was chosen to aim at rate constants on the order of $10^{-4} \text{ M}^{-1} \text{ s}^{-1}$, which allow quantitation. It was of interest to compare rate constants of ligand exchange reactions involving either thiolate or selenolate according to electron donating capability. The pKa's of 4-bromobenzenethiol, benzenethiol, benzeneselenol are 6.08, 6.5 and 5.9, respectively. In DMSO, that of 4-bromobenzenethiol is 9.0,²⁹¹ benzenethiol is 10.3,²⁹¹ and benzeneselenol is 7.1.²⁹² The difference in pKa between provide explanation of why exchange with benzeneselenolate or 4-bromobenzenethiol as the incoming ligand is more rapid than that of the thiol by about an order of magnitude over the range of temperatures studied. The exchange reaction likely involves partial or complete charge transfer between the incoming ligand and deprotonation of the incoming ligand is concerted with association to the nanoparticle. Complete proton dissociation from the incoming ligand, before binding to the nanoparticle, would result in an unfavorable electrostatic repulsion. The literature of selenolate SAMs on Au surfaces, if viewed as a two-dimensional analogs to MPCs, is relevant; recent work²⁹³ on replacement of

thiolates by selenolates on Au(111) surfaces at room temperature is rapid, complete, occurs primarily at defects, and the resulting selenolate–gold attachment is labile. The kinetics of SAM formation and rearrangement of ligands on Au surfaces- or analogous clusters- may share similar properties in which stronger electronic coupling of the headgroup ($\text{Se} > \text{S}$) promotes association.^{294,295} The implication is that ligand exchange involves at least a partial charge transfer between the nanoparticle and the incoming ligand and that this describes a rate determining condition.

In conclusion, this study shows that electron density or charge state of the nanoparticle as well as the incoming ligand can play a role in the mechanism of ligand exchange. The higher electron density in the semirings of the negatively charged clusters as well as higher electronic coupling of the selenolate ligand compared to thiolate can qualitatively account for the differences in quantitative rate constants of ligand exchange observed here. The order of magnitude difference observed for the rate constant of ligand exchange with the –Se ligand gives a measure of the large extent by which the electronic coupling of the incoming ligand and cluster semirings influences cluster assembly and behavior. Further of differences in nanoparticle properties, including solid state conductivities of their films should give a better sense of how these clusters can be incorporated into devices as sensors, catalysts, and electronic components.

5.4 Acknowledgements

This research was supported in part by the Office of Naval Research and the National Science Foundation. T. M. C. acknowledges support from a National Defense Science & Engineering Graduate (NDSEG) Fellowship, from the Department of Defense. The authors would like to thank Marc ter Horst and Laura Adduci of the UNC Nuclear Magnetic Resonance Facility for helpful discussions.

5.5 Tables and figures

Table 5.1. Dependence of ligand exchange kinetics for 4-bromothiophenol incoming ligand on charge state of $\text{Au}_{25}(\text{C}_2\text{Ph})_{18}$ MPCs (N = number of experiments).

MPC	MPC Charge	k ($\text{M}^{-1} \text{s}^{-1}$)	N
$\text{Au}_{25}(\text{C}_2\text{Ph})_{18}^{0/-1}$	all -1	$(1.2 \pm 0.5) \times 10^{-4}$	3
$\text{Au}_{25}(\text{C}_2\text{Ph})_{18}^{0/-1}$	50% -1	$(8.7 \pm 3.1) \times 10^{-5}$	2
$\text{Au}_{25}(\text{C}_2\text{Ph})_{18}^{+1/0}$	all +1	$(1.9 \pm 1.3) \times 10^{-5}$	2

Table 5.2. Comparison of ligand exchange kinetics for benzene-thiol or -selenol incoming ligands in $\text{Au}_{25}(\text{C}_2\text{Ph})_{18}$ MPCs in the 100% -1 charge state (N = number of experiments).

Incoming Ligand	Temp ($^{\circ}\text{C}$)	k ($\text{M}^{-1} \text{s}^{-1}$)	N
PhSH	$\sim 0^{\text{a}}$	$(8.7 \pm 7.6) \times 10^{-5}$	4
	10	$(5.7 \pm 1.7) \times 10^{-4}$	3
PhSeH	-10	$(3.1 \pm 1.4) \times 10^{-4}$	3
	$\sim 0^{\text{a}}$	$(4.5 \pm 2.0) \times 10^{-4}$	4
	25	$(1.2 \pm 0.2) \times 10^{-3}$	2

^a Approximate temperature

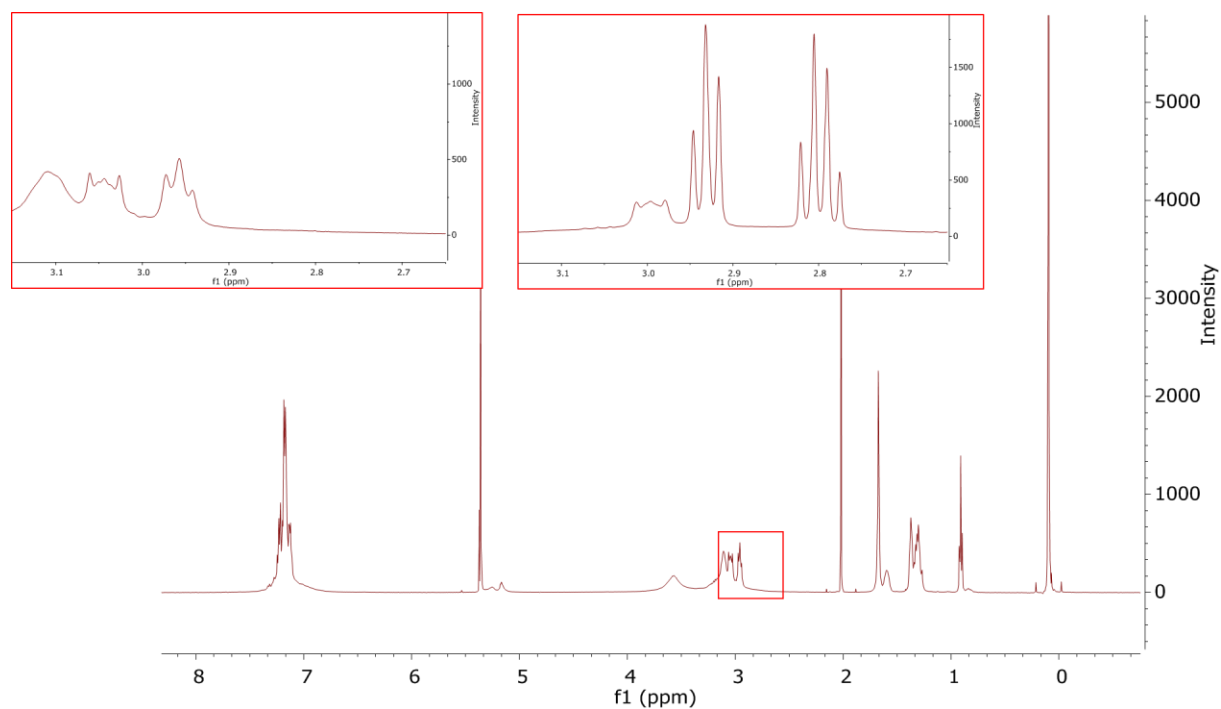


Figure 5.1. NMR spectrum of Au₂₅(PhC₂S)₁₈⁻¹ in CD₂Cl₂ with CH₃CN as an internal standard (1.93 ppm). Upper left inset: The 2.65-3.15 ppm region of the original spectrum; upper right inset: 2.65-3.15 ppm region after a ligand exchange reaction has taken place, showing the appearance of the quartet at 2.76 ppm corresponding to the protons alpha to the thiol group of the liberated PhC₂SH.

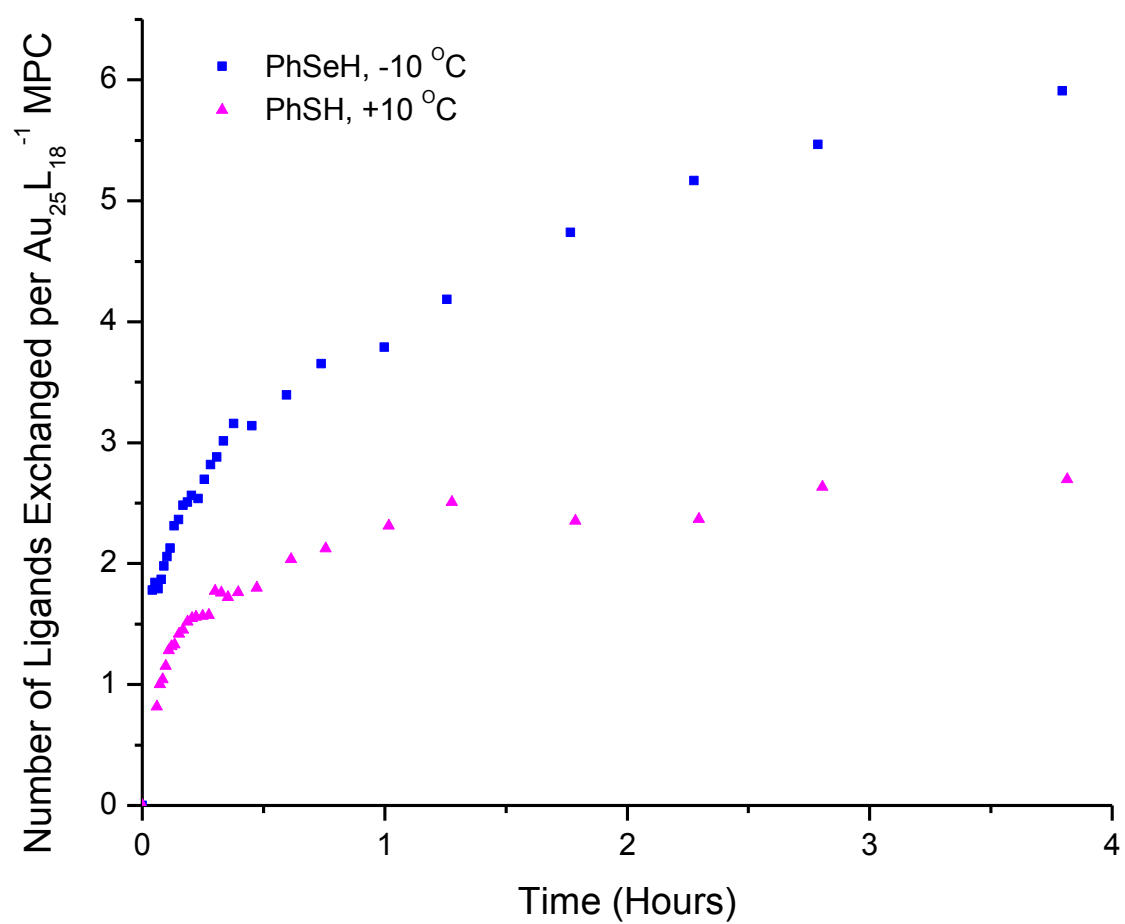


Figure 5.2. Number of ligands of $\text{Au}_{25}(\text{PhC}_2\text{S})_{18}^{-1}$ replaced by incoming ligand, either thiolate or selenolate, during the ligand exchange reaction, as monitored by ^1H NMR.

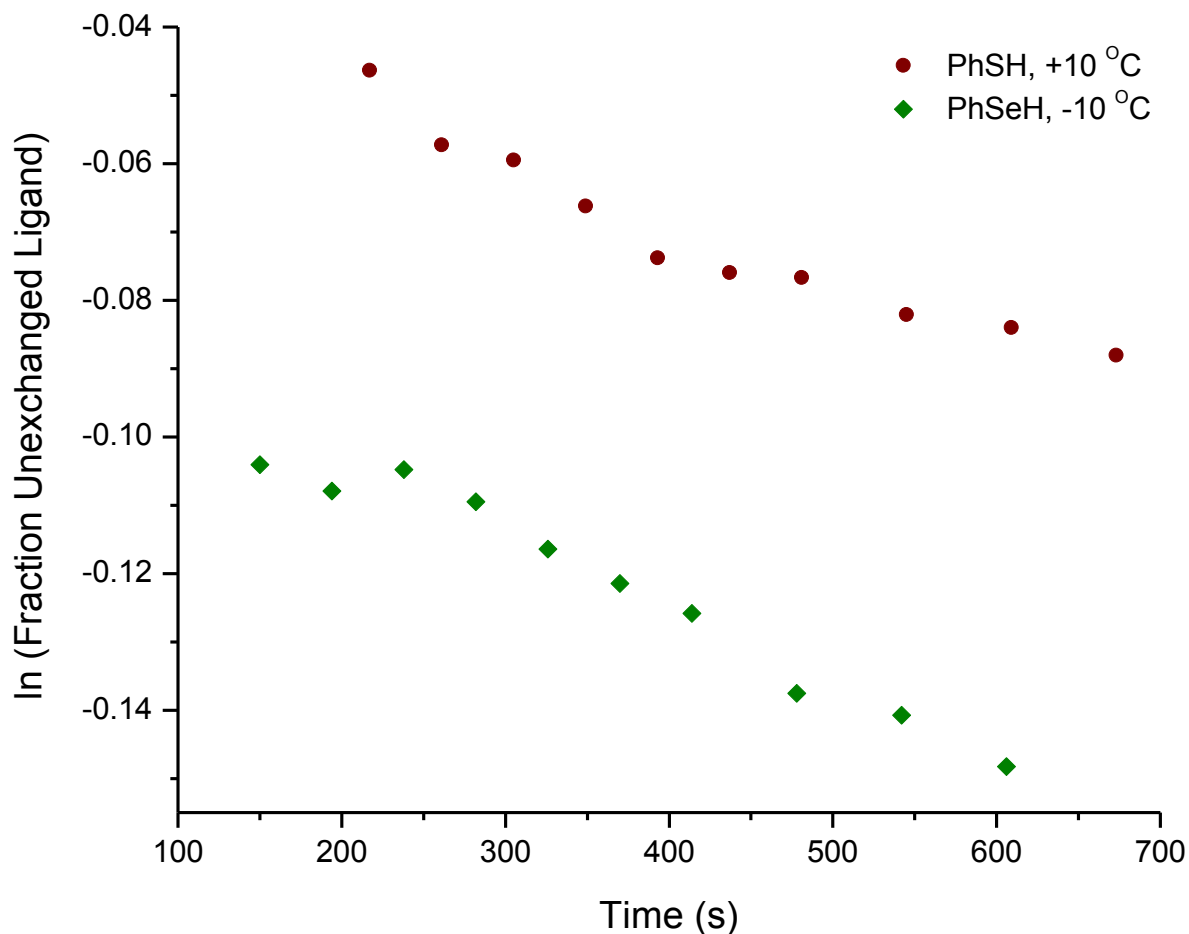


Figure 5.3. Plot of the natural log of the fraction of ligands of $\text{Au}_{25}(\text{PhC}_2\text{S})_{18}^{-1}$ not replaced by molecules of incoming ligand, either thiol or selenol, over the course of the ligand exchange reaction. The first ten data points, collected within the first ten minutes exchange, were linearized to obtain the initial ligand exchange rate constant.

APPENDIX A: MORE DETAILED INFORMATION ABOUT $\text{Au}_{25}(\text{SC}_2\text{PH})_{18}$ AND $\text{Au}_{144}(\text{SC}_6\text{H}_{13})_{60}$ SYNTHESSES AND A SCHEMATIC OF THE IDA ELECTRODE⁶

A.1 Synthesis of $\text{Au}_{144}(\text{SC}_6\text{H}_{13})_{60}$

Monodisperse $\text{Au}_{144}(\text{SC}_6\text{H}_{13})_{60}$ was synthesized according to Hicks et al.⁷⁰ with some modifications. The synthesis is adapted from the Brust method,¹ involving a transfer of aqueous hydrogen tetrachloroaurate to the organic phase where it binds to hexanethiol ligand, followed by a reduction with sodium borohydride and several purification steps. The polydisperse Au MPCs undergo size focusing (also called annealing) which greatly increases core size purity for the synthesis of $\text{Au}_{144}(\text{SC}_6\text{H}_{13})_{60}$. In this process, Au MPCs are thought to simultaneously undergo core fusion (core size growth) and etching (core size reduction) in the presence of excess thiol and open air over a period of days to reach the most thermodynamically stable state of core size 144. The mechanism of size focusing is not well understood but results in the formation of monodisperse Au MPCs and Au-thiol polymer as by-product indicating the mechanism may involve transfer of Au to (from) the nanoparticle core from (to) the excess thiol.

1 g of $\text{HAuCl}_4 : 3\text{H}_2\text{O}$ is dissolved in ~ 10 mL nanopure H_2O . Tetraoctylammonium bromide ($\text{Oct}_4\text{N}^+\text{Br}^-$) in a 1:1 mole ratio with the gold salt is dissolved in ~10 mL toluene in a 250 mL round bottom flask. The aqueous solution of $\text{HAuCl}_4 : 3\text{H}_2\text{O}$ is added to the $\text{Oct}_4\text{N}^+\text{Br}^-$ /toluene and stirred for 30 minutes or until the top layer is a deep reddish color. The aqueous layer is removed with a 125 mL separatory funnel and transferred into a 500 mL round bottom flask. 1-hexanethiol in a 3:1 ratio with $\text{HAuCl}_4 : 3\text{H}_2\text{O}$ is added and stirred (large stir bar at high speed) for 20 minutes or until colorless. NaBH_4 in a 10:1 ratio with the $\text{HAuCl}_4 : 3\text{H}_2\text{O}$ is

⁶ The materials in this Appendix were adapted from the Supporting Information section accompanying Carducci, T. M.; Murray, R. W. *J Am Chem Soc* 2013, 135, 11351.

dissolved in a minimal amount of nanopure H₂O and cooled on ice for at least 20 minutes before adding to the stirring reaction mixture. The reaction mixture is transferred to an ice bath. NaBH₄ is added all at once, and stirred (large stir bar at medium speed) for 1 hour. Excess NaBH₄ is extracted with Nanopure H₂O in a 500 mL separatory funnel three times. The organic layer (toluene plus Au MPCs) is transferred to a 250 mL round bottom flask and rotovapped to a sludge. ~100 mL of absolute ethanol is added and stirred overnight (medium stir bar at high speed). At this point, the flask is kept covered in aluminum foil when possible to prevent photooxidation. The Au MPCs in ethanol are filtered through a medium frit funnel and the ethanol-soluble portion of Au MPCs collected and transferred into a 250 mL round bottom flask and rotovapped to a sludge. ~100 mL of acetonitrile is added and stirred overnight (medium stir bar at high speed). The Au MPCs in acetonitrile are filtered through a medium funnel. The acetonitrile-insoluble Au MPCs are collected with dichloromethane, transferred to a 100 mL round bottom flask, and rotovapped to dryness. 10 mL dichloromethane is added and stirred (small stir bar at high speed), then 10 μ L 1-hexanethiol is added. The flask is capped and stirred for four days. The flask is opened for at one minute on day 2 of stirring to reoxygenate the reaction. The flask is rotovapped to dryness and washed three times with acetonitrile to remove excess thiol. The monodisperse Au₁₄₄ MPCs are transferred to scintillation vials with dichloromethane and rotovapped to dryness. The vials are stored overnight in a vacuum oven before weighing. The Au₁₄₄ MPCs are then characterized by cyclic voltammetry and differential pulse voltammetry.

A.2 Synthesis of Au₂₅(SC₂Ph)₁₈

0.5 g of HAuCl₄ : 3H₂O and (Oct)₄N⁺Br⁻ in a 1:1 ratio are dissolved in 35 mL fresh THF in a 100 mL round bottom flask. 0.9 mL HSC₂Ph is added and stirred overnight (small stir bar at

high speed). NaBH_4 in a 10:1 ratio with the $\text{HAuCl}_4 : 3\text{H}_2\text{O}$ is dissolved in 6 mL Nanopure H_2O and cooled on ice for at least 20 minutes before adding to the stirring reaction mixture. NaBH_4 is added all at once, and stirred (small stir bar at high speed) for four days. During the four day stirring, the flask is covered minimally with a petri dish. The reaction mixture is filtered through a medium frit funnel to collect solid precipitates and rotovapped to near dryness (water will remain). The Au MPCs are reconstituted in ~25 mL toluene and transferred to a 250 mL separatory funnel. The Au MPCs in toluene are washed three times with Nanopure H_2O then rotovapped to a sludge and then washed three times with methanol to remove excess $(\text{Oct})_4\text{N}^+\text{Br}^-$. The Au MPCs are reconstituted in dichloromethane, transferred to scintillation vials, and rotovapped to dryness. The vials are stored overnight in a vacuum oven before weighing. The Au_{25} MPCs are then characterized by cyclic voltammetry, differential pulse voltammetry, and UV-visible spectroscopy.

A.3 Figures

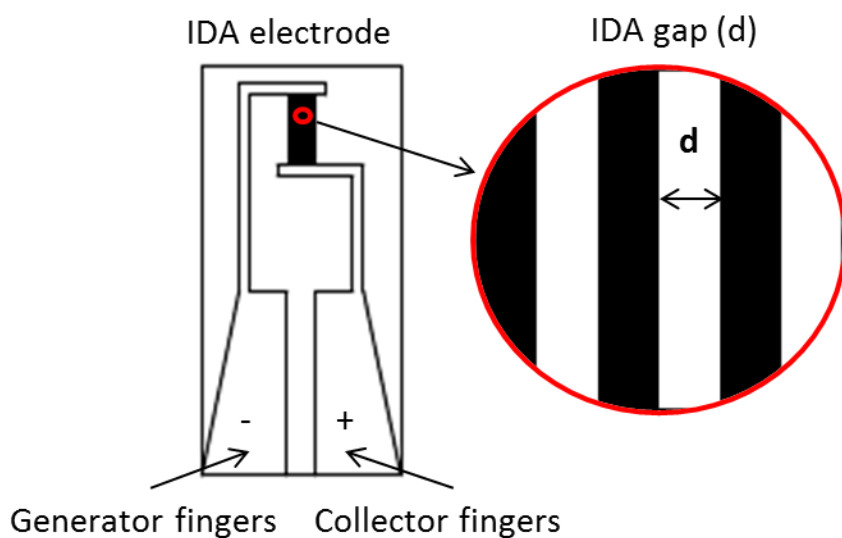


Figure A.1. Schematic of the interdigitated array (IDA) electrode used to collect conductivity data. The mixed-valent solid-state Au MPC film is dropcasted atop the fingers and the IDA electrode is affixed to the cryostat sample stage.

APPENDIX B: RECALCULATED VALUES OF σ_{EL} BASED ON THE IMPROVED ESTIMATES OF δ ⁷

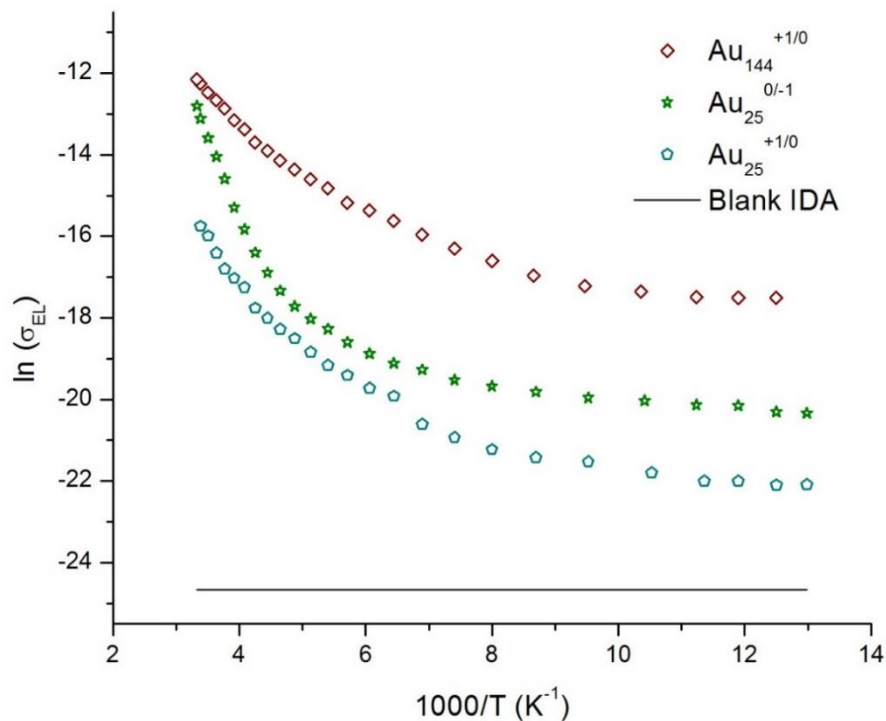


Figure B.1. Arrhenius plots of solid-state nonferrocenated MPC films containing mixed valent proportions ($\sim 50\%$) of $\text{Au}_{144}^{+1/0}$, $\text{Au}_{25}^{+1/0}$, and $\text{Au}_{25}^{0/-1}$. This data was published previously but was recalculated due to the determination of more accurate values of δ and presented here for comparison purposes.

⁷ The materials in this Appendix were adapted from the Supporting Information section accompanying Carducci, T. M.; Blackwell, R. E.; Murray, R. W. *J Am Chem Soc* **2014**, *136*, 11182.

REFERENCES

- (1) Brust, M.; Walker, M.; Bethell, D.; Schiffrin, D. J.; Whyman, R. *Journal of the Chemical Society, Chemical Communications* **1994**, 801.
- (2) Whitesides, G. M.; Grzybowski, B. *Science* **2002**, 295, 2418.
- (3) Mrksich, M.; Whitesides, G. M. *Annual review of biophysics and biomolecular structure* **1996**, 25, 55.
- (4) Terrill, R. H.; Postlethwaite, T. A.; Chen, C.-h.; Poon, C.-D.; Terzis, A.; Chen, A.; Hutchison, J. E.; Clark, M. R.; Wignall, G.; et, a. *J. Am. Chem. Soc.* **1995**, 117, 12537.
- (5) Hostetler, M. J.; Green, S. J.; Stokes, J. J.; Murray, R. W. *Journal of the American Chemical Society* **1996**, 118, 4212.
- (6) Ingram, R. S.; Hostetler, M. J.; Murray, R. W.; Schaaff, T. G.; Khoury, J.; Whetten, R. L.; Bigioni, T. P.; Guthrie, D. K.; First, P. N. *J. Am. Chem. Soc.* **1997**, 119, 9279.
- (7) Green, S. J.; Stokes, J. J.; Hostetler, M. J.; Pietron, J.; Murray, R. W. *The Journal of Physical Chemistry B* **1997**, 101, 2663.
- (8) Sardar, R.; Funston, A. M.; Mulvaney, P.; Murray, R. W. *Langmuir* **2009**, 25, 13840.
- (9) Heaven, M. W.; Dass, A.; White, P. S.; Holt, K. M.; Murray, R. W. *Journal of the American Chemical Society* **2008**, 130, 3754.
- (10) Zhu, M.; Aikens, C. M.; Hollander, F. J.; Schatz, G. C.; Jin, R. *J Am Chem Soc* **2008**, 130, 5883.
- (11) Akola, J.; Walter, M.; Whetten, R. L.; Hakkinen, H.; Gronbeck, H. *J Am Chem Soc* **2008**, 130, 3756.
- (12) Murray, R. W. *Chemical Reviews* **2008**, 108, 2688.
- (13) Astruc, D.; Boisselier, E.; Ornelas, C. *Chem Rev* **2010**, 110, 1857.
- (14) Hostetler, M. J.; Templeton, A. C.; Murray, R. W. *Langmuir* **1999**, 15, 3782.
- (15) Templeton, A. C.; Hostetler, M. J.; Kraft, C. T.; Murray, R. W. *J. Am. Chem. Soc.* **1998**, 120, 1906.
- (16) Ingram, R. S.; Hostetler, M. J.; Murray, R. W. *Journal of the American Chemical Society* **1997**, 119, 9175.
- (17) Toikkanen, O.; Ruiz, V.; Ronnholm, G.; Kalkkinen, N.; Liljeroth, P.; Quinn, B. M. *J Am Chem Soc* **2008**, 130, 11049.

- (18) Gies, A. P.; Hercules, D. M.; Gerdon, A. E.; Clifffel, D. E. *J Am Chem Soc* **2007**, *129*, 1095.
- (19) Varnavski, O.; Ramakrishna, G.; Kim, J.; Lee, D.; Goodson, T. *J Am Chem Soc* **2010**, *132*, 16.
- (20) Antonello, S.; Hesari, M.; Polo, F.; Maran, F. *Nanoscale* **2012**, *4*, 5333.
- (21) Tracy, J. B.; Crowe, M. C.; Parker, J. F.; Hampe, O.; Fields-Zinna, C. A.; Dass, A.; Murray, R. W. *J. Am. Chem. Soc.* **2007**, *129*, 16209.
- (22) Georganopoulou, D. G.; Mirkin, M. V.; Murray, R. W. *Nano Letters* **2004**, *4*, 1763.
- (23) Hakkinen, H.; Walter, M.; Gronbeck, H. *The journal of physical chemistry. B* **2006**, *110*, 9927.
- (24) Templeton, A. C.; Wuelfing, W. P.; Murray, R. W. *Accounts of chemical research* **2000**, *33*, 27.
- (25) Oja, S. M.; Wood, M.; Zhang, B. *Analytical Chemistry* **2012**, *85*, 473.
- (26) Devarajan, S.; Sampath, S.; Wiley-VCH Verlag GmbH & Co. KGaA: 2004; Vol. 2, p 646.
- (27) Love, J. C.; Estroff, L. A.; Kriebel, J. K.; Nuzzo, R. G.; Whitesides, G. M. *Chemical Reviews* **2005**, *105*, 1103.
- (28) Zamborini, F. P.; Bao, L.; Dasari, R. *Anal Chem* **2012**, *84*, 541.
- (29) *Nanoscale* **2012**, *4*, 4009.
- (30) Schmid, G.; Pfeil, R.; Boese, R.; Brandermann, F.; Meyer, S.; Calis, G. H. M.; Van, d. V. J. W. A. *Chem. Ber.* **1981**, *114*, 3634.
- (31) Tsunoyama, R.; Tsunoyama, H.; Pannopard, P.; Limtrakul, J.; Tsukuda, T. *The Journal of Physical Chemistry C* **2010**, *114*, 16004.
- (32) Mulvaney, P. *Langmuir* **1996**, *12*, 788.
- (33) Menard, L. D.; Xu, H.; Gao, S.-P.; Twisten, R. D.; Harper, A. S.; Song, Y.; Wang, G.; Douglas, A. D.; Yang, J. C.; Frenkel, A. I.; Murray, R. W.; Nuzzo, R. G. *The Journal of Physical Chemistry B* **2006**, *110*, 14564.
- (34) Tracy, J. B.; Kalyuzhny, G.; Crowe, M. C.; Balasubramanian, R.; Choi, J. P.; Murray, R. W. *J Am Chem Soc* **2007**, *129*, 6706.
- (35) Dass, A.; Stevenson, A.; Dubay, G. R.; Tracy, J. B.; Murray, R. W. *J. Am. Chem. Soc.* **2008**, *130*, 5940.

- (36) Dass, A.; Holt, K.; Parker, J. F.; Feldberg, S. W.; Murray, R. W. *The Journal of Physical Chemistry C* **2008**, *112*, 20276.
- (37) Fields-Zinna, C. A.; Sardar, R.; Beasley, C. A.; Murray, R. W. *J Am Chem Soc* **2009**, *131*, 16266.
- (38) Jadzinsky, P. D.; Calero, G.; Ackerson, C. J.; Bushnell, D. A.; Kornberg, R. D. *Science* **2007**, *318*, 430.
- (39) Levi-Kalisman, Y.; Jadzinsky, P. D.; Kalisman, N.; Tsunoyama, H.; Tsukuda, T.; Bushnell, D. A.; Kornberg, R. D. *J Am Chem Soc* **2011**, *133*, 2976.
- (40) Whetten, R. L.; Price, R. C. *Science* **2007**, *318*, 407.
- (41) Qian, H.; Eckenhoff, W. T.; Zhu, Y.; Pintauer, T.; Jin, R. *J. Am. Chem. Soc.* **2010**, *132*, 8280.
- (42) Zeng, C.; Qian, H.; Li, T.; Li, G.; Rosi, N. L.; Yoon, B.; Barnett, R. N.; Whetten, R. L.; Landman, U.; Jin, R. *Angewandte Chemie* **2012**, *51*, 13114.
- (43) Qian, H.; Jin, R. *Nano Lett.* **2009**, *9*, 4083.
- (44) Oh, S.-K.; Kim, Y.-G.; Ye, H.; Crooks, R. M. *Langmuir* **2003**, *19*, 10420.
- (45) Garcia-Martinez, J. C.; Crooks, R. M. *J Am Chem Soc* **2004**, *126*, 16170.
- (46) Knecht, M. R.; Garcia-Martinez, J. C.; Crooks, R. M. *Langmuir* **2005**, *21*, 11981.
- (47) Knecht, M. R.; Garcia-Martinez, J. C.; Crooks, R. M. *Chem. Mater.* **2006**, *18*, 5039.
- (48) Knecht, M. R.; Weir, M. G.; Frenkel, A. I.; Crooks, R. M. *Chem. Mater.* **2008**, *20*, 1019.
- (49) Weir, M. G.; Knecht, M. R.; Frenkel, A. I.; Crooks, R. M. *Langmuir* **2010**, *26*, 1137.
- (50) Kim, Y.-G.; Garcia-Martinez, J. C.; Crooks, R. M. *Langmuir* **2005**, *21*, 5485.
- (51) Wolfe, R. L.; Murray, R. W. *Anal Chem* **2006**, *78*, 1167.
- (52) Jimenez, V. L.; Georganopoulou, D. G.; White, R. J.; Harper, A. S.; Mills, A. J.; Lee, D.; Murray, R. W. *Langmuir* **2004**, *20*, 6864.
- (53) Guo, R.; Murray, R. W. *J Am Chem Soc* **2005**, *127*, 12140.
- (54) Wang, W.; Lee, D.; Murray, R. W. *The journal of physical chemistry. B* **2006**, *110*, 10258.
- (55) Wang, G.; Guo, R.; Kalyuzhny, G.; Choi, J. P.; Murray, R. W. *The journal of physical chemistry. B* **2006**, *110*, 20282.

- (56) Choi, J. P.; Murray, R. W. *J Am Chem Soc* **2006**, *128*, 10496.
- (57) Wolfe, R. L.; Balasubramanian, R.; Tracy, J. B.; Murray, R. W. *Langmuir* **2007**, *23*, 2247.
- (58) Antonello, S.; Holm, A. H.; Instuli, E.; Maran, F. *J. Am. Chem. Soc.* **2007**, *129*, 9836.
- (59) Parker, J. F.; Choi, J.-P.; Wang, W.; Murray, R. W. *The Journal of Physical Chemistry C* **2008**, *112*, 13976.
- (60) Parker, J. F.; Kacprzak, K. A.; Lopez-Acevedo, O.; Häkkinen, H.; Murray, R. W. *The Journal of Physical Chemistry C* **2010**, *114*, 8276.
- (61) Zhu, M.; Eckenhoff, W. T.; Pintauer, T.; Jin, R. *The Journal of Physical Chemistry C* **2008**, *112*, 14221.
- (62) Zhu, M.; Aikens, C. M.; Hendrich, M. P.; Gupta, R.; Qian, H.; Schatz, G. C.; Jin, R. *J Am Chem Soc* **2009**, *131*, 2490.
- (63) Bard, A. J.; Faulkner, L. R. In *Electrochemical Methods Fundamentals and Applications*; 2 ed.; John Wiley & Sons: Hoboken, NJ, 2001, p 736.
- (64) Wang, G.; Huang, T.; Murray, R. W.; Menard, L.; Nuzzo, R. G. *J Am Chem Soc* **2005**, *127*, 812.
- (65) Li, L.; Liu, H.; Shen, Y.; Zhang, J.; Zhu, J. *J. Anal Chem* **2011**, *83*, 661.
- (66) Swanick, K. N.; Hesari, M.; Workentin, M. S.; Ding, Z. *J Am Chem Soc* **2012**, *134*, 15205.
- (67) Toikkanen, O.; Carlsson, S.; Dass, A.; Rönholm, G.; Kalkkinen, N.; Quinn, B. M. *The Journal of Physical Chemistry Letters* **2010**, *1*, 32.
- (68) Nimmala, P. R.; Yoon, B.; Whetten, R. L.; Landman, U.; Dass, A. *The Journal of Physical Chemistry A* **2013**, *117*, 504.
- (69) Balasubramanian, R.; Guo, R.; Mills, A. J.; Murray, R. W. *J Am Chem Soc* **2005**, *127*, 8126.
- (70) Hicks, J. F.; Miles, D. T.; Murray, R. W. *J Am Chem Soc* **2002**, *124*, 13322.
- (71) Hicks, J. F.; Templeton, A. C.; Chen, S.; Sheran, K. M.; Jasti, R.; Murray, R. W.; Debord, J.; Schaaff, T. G.; Whetten, R. L. *Anal Chem* **1999**, *71*, 3703.
- (72) Zamborini, F. P.; Hicks, J. F.; Murray, R. W. *Journal of the American Chemical Society* **2000**, *122*, 4514.
- (73) Lopez-Acevedo, O.; Akola, J.; Whetten, R. L.; Grönbeck, H.; Häkkinen, H. *The Journal of Physical Chemistry C* **2009**, *113*, 5035.

- (74) Mertens, S. F. L.; Blech, K.; Sologubenko, A. S.; Mayer, J.; Simon, U.; Wandlowski, T. *Electrochim. Acta* **2009**, *54*, 5006.
- (75) Koivisto, J.; Malola, S.; Kumara, C.; Dass, A.; Häkkinen, H.; Pettersson, M. *The Journal of Physical Chemistry Letters* **2012**, *3*, 3076.
- (76) Chen, S.; Ingram, R. S.; Hostetler, M. J.; Pietron, J. J.; Murray, R. W.; Schaaff, T. G.; Khoury, J. T.; Alvarez, M. M.; Whetten, R. L. *Science* **1998**, *280*, 2098.
- (77) Chen, S.; Murray, R. W.; Feldberg, S. W. *The Journal of Physical Chemistry B* **1998**, *102*, 9898.
- (78) Peterson, R. R.; Cliffler, D. E. *Langmuir* **2006**, *22*, 10307.
- (79) García-Raya, D.; Madueño, R.; Blázquez, M.; Pineda, T. *The Journal of Physical Chemistry C* **2009**, *113*, 8756.
- (80) Lee, D.; Donkers, R. L.; DeSimone, J. M.; Murray, R. W. *J. Am. Chem. Soc.* **2003**, *125*, 1182.
- (81) Chen, S.; Yang, Y. *J Am Chem Soc* **2002**, *124*, 5280.
- (82) Yang, Y.; Grant, K. M.; White, H. S.; Chen, S. *Langmuir* **2003**, *19*, 9446.
- (83) Pietron, J. J.; Hicks, J. F.; Murray, R. W. *Journal of the American Chemical Society* **1999**, *121*, 5565.
- (84) Quinn, B. M.; Liljeroth, P.; Kontturi, K. *J Am Chem Soc* **2002**, *124*, 12915.
- (85) Hicks, J. F.; Zamborini, F. P.; Murray, R. W. *The Journal of Physical Chemistry B* **2002**, *106*, 7751.
- (86) Chen, S. *The Journal of Physical Chemistry B* **2000**, *104*, 663.
- (87) Chen, S. *Journal of the American Chemical Society* **2000**, *122*, 7420.
- (88) Chen, S.; Pei, R. *J Am Chem Soc* **2001**, *123*, 10607.
- (89) Liu, F.; Khan, K.; Liang, J. H.; Yan, J. W.; Wu, D. Y.; Mao, B. W.; Jensen, P. S.; Zhang, J.; Ulstrup, J. *Chemphyschem : a European journal of chemical physics and physical chemistry* **2013**, *14*, 952.
- (90) Men, Y.; Kubo, K.; Kurihara, M.; Nishihara, H. *Phys. Chem. Chem. Phys.* **2001**, *3*, 3427.
- (91) Brennan, J. L.; Branham, M. R.; Hicks, J. F.; Osisek, A. J.; Donkers, R. L.; Georganopoulou, D. G.; Murray, R. W. *Anal Chem* **2004**, *76*, 5611.
- (92) Hicks, J. F.; Zamborini, F. P.; Osisek, A. J.; Murray, R. W. *Journal of the American Chemical Society* **2001**, *123*, 7048.

- (93) Zamborini, F. P.; Leopold, M. C.; Hicks, J. F.; Kulesza, P. J.; Malik, M. A.; Murray, R. W. *J Am Chem Soc* **2002**, *124*, 8958.
- (94) Uosaki, K.; Kondo, T.; Okamura, M.; Song, W. *Faraday Discussions* **2002**, *121*, 373.
- (95) Chen, S.; Pei, R.; Zhao, T.; Dyer, D. J. *The Journal of Physical Chemistry B* **2002**, *106*, 1903.
- (96) Brust, M.; Bethell, D.; Kiely, C. J.; Schiffrin, D. J. *Langmuir* **1998**, *14*, 5425.
- (97) Liljeroth, P.; Vanmaekelbergh, D.; Ruiz, V.; Kontturi, K.; Jiang, H.; Kauppinen, E.; Quinn, B. M. *J. Am. Chem. Soc.* **2004**, *126*, 7126.
- (98) Joseph, Y.; Besnard, I.; Rosenberger, M.; Guse, B.; Nothofer, H.-G.; Wessels, J. M.; Wild, U.; Knop-Gericke, A.; Su, D.; Schlögl, R.; Yasuda, A.; Vossmeier, T. *The Journal of Physical Chemistry B* **2003**, *107*, 7406.
- (99) Laaksonen, T.; Ruiz, V.; Liljeroth, P.; Quinn, B. M. *J. Phys. Chem. C* **2008**, *112*, 15637.
- (100) Liljeroth, P.; Quinn, B. M. *J. Am. Chem. Soc.* **2006**, *128*, 4922.
- (101) Yang, Y.; Pradhan, S.; Chen, S. *J Am Chem Soc* **2004**, *126*, 76.
- (102) Chen, S. *Analytica Chimica Acta* **2003**, *496*, 29.
- (103) Kim, J.; Lee, D. *J. Am. Chem. Soc.* **2006**, *128*, 4518.
- (104) Li, W.; Su, B. *Electrochemistry Communications* **2012**, *22*, 8.
- (105) Deng, F.; Chen, S. *Langmuir* **2007**, *23*, 936.
- (106) Deng, F.; Chen, S. *Physical chemistry chemical physics : PCCP* **2005**, *7*, 3375.
- (107) Wang, W.; Murray, R. W. *Analytical Chemistry* **2007**, *79*, 1213.
- (108) Laaksonen, T.; Ruiz, V.; Murtomaeki, L.; Quinn, B. M. *J. Am. Chem. Soc.* **2007**, *129*, 7732.
- (109) Ahonen, P.; Ruiz, V.; Kontturi, K.; Liljeroth, P.; Quinn, B. M. *J Phys Chem C* **2008**, *112*, 2724.
- (110) Ranganathan, S.; Guo, R.; Murray, R. W. *Langmuir* **2007**, *23*, 7372.
- (111) Xu, R.; Sun, Y.; Yang, J.-Y.; He, L.; Nie, J.-C.; Li, L.; Li, Y. *Applied Physics Letters* **2010**, *97*, 113101.
- (112) Savéant, J. M. *Journal of Electroanalytical Chemistry and Interfacial Electrochemistry* **1988**, *242*, 1.
- (113) White, R. J.; White, H. S. *Analytical Chemistry* **2005**, *77*, 214 A.

- (114) Terrill, R. H.; Hutchison, J. E.; Murray, R. W. *The Journal of Physical Chemistry B* **1997**, *101*, 1535.
- (115) Jernigan, J. C.; Surridge, N. A.; Zvanut, M. E.; Silver, M.; Murray, R. W. *The Journal of Physical Chemistry* **1989**, *93*, 4620.
- (116) Wuelfing, W. P.; Green, S. J.; Pietron, J. J.; Cliffler, D. E.; Murray, R. W. *J. Am. Chem. Soc.* **2000**, *122*, 11465.
- (117) Wuelfing, W. P.; Murray, R. W. *The Journal of Physical Chemistry B* **2002**, *106*, 3139.
- (118) Carducci, T. M.; Murray, R. W. *J Am Chem Soc* **2013**, *135*, 11351.
- (119) Pradhan, S.; Kang, X.; Mendoza, E.; Chen, S. *Appl. Phys. Lett.* **2009**, *94*, 042113/1.
- (120) Pradhan, S.; Sun, J.; Deng, F.; Chen, S. *Adv. Mater. (Weinheim, Ger.)* **2006**, *18*, 3279.
- (121) Wallner, A.; Jafri, S. H.; Blom, T.; Gogoll, A.; Leifer, K.; Baumgartner, J.; Ottosson, H. *Langmuir* **2011**, *27*, 9057.
- (122) Zamborini, F. P.; Smart, L. E.; Leopold, M. C.; Murray, R. W. *Analytica Chimica Acta* **2003**, *496*, 3.
- (123) Leopold, M. C.; Donkers, R. L.; Georganopoulou, D.; Fisher, M.; Zamborini, F. P.; Murray, R. W. *Faraday Discussions* **2004**, *125*, 63.
- (124) Fishelson, N.; Shkrob, I.; Lev, O.; Gun, J.; Modestov, A. D. *Langmuir* **2001**, *17*, 403.
- (125) Trudeau, P. E.; Orozco, A.; Kwan, E.; Dhirani, A. A. *The Journal of Chemical Physics* **2002**, *117*, 3978.
- (126) Trudeau, P. E.; Escorcia, A.; Dhirani, A. A. *The Journal of Chemical Physics* **2003**, *119*, 5267.
- (127) Wang, G. R.; Wang, L.; Rendeng, Q.; Wang, J.; Luo, J.; Zhong, C.-J. *Journal of Materials Chemistry* **2007**, *17*, 457.
- (128) Choi, J.-P.; Coble, M. M.; Branham, M. R.; DeSimone, J. M.; Murray, R. W. *The Journal of Physical Chemistry C* **2007**, *111*, 3778.
- (129) Branham, M. R.; Douglas, A. D.; Mills, A. J.; Tracy, J. B.; White, P. S.; Murray, R. W. *Langmuir* **2006**, *22*, 11376.
- (130) Wu, Z.; Lanni, E.; Chen, W.; Bier, M. E.; Ly, D.; Jin, R. *J Am Chem Soc* **2009**, *131*, 16672.
- (131) Snow, A. W.; Wohltjen, H. *Chemistry of Materials* **1998**, *10*, 947.

- (132) Zabet-Khosousi, A.; Trudeau, P. E.; Suganuma, Y.; Dhirani, A. A.; Statt, B. *Physical review letters* **2006**, *96*, 156403.
- (133) Suganuma, Y.; Dhirani, A. A. *The journal of physical chemistry. B* **2005**, *109*, 15391.
- (134) Nair, A. S.; Kimura, K. *Langmuir* **2009**, *25*, 1750.
- (135) Nair, A. S.; Kimura, K. *J Chem Phys* **2008**, *129*, 184117.
- (136) Muller, K. H.; Herrmann, J.; Wei, G.; Raguse, B.; Wieczorek, L. *J. Phys. Chem. C* **2009**, *113*, 18027.
- (137) McCreery, R. L. *Chemistry of Materials* **2004**, *16*, 4477.
- (138) Kumara, C.; Dass, A. *Nanoscale* **2011**, *3*, 3064.
- (139) Li, Y.; Cox, J. T.; Zhang, B. *Journal of the American Chemical Society* **2010**, *132*, 3047.
- (140) Kwon, S. J.; Zhou, H.; Fan, F.-R. F.; Vorobyev, V.; Zhang, B.; Bard, A. J. *Physical Chemistry Chemical Physics* **2011**, *13*, 5394.
- (141) Zhou, H.; Fan, F.-R. F.; Bard, A. J. *The Journal of Physical Chemistry Letters* **2010**, *1*, 2671.
- (142) Kwon, S. J.; Fan, F.-R. F.; Bard, A. J. *Journal of the American Chemical Society* **2010**, *132*, 13165.
- (143) Chen, S.; Huang, K. *J. Cluster Sci.* **2000**, *11*, 405.
- (144) Ghosh, D.; Chen, S. *Journal of Materials Chemistry* **2008**, *18*, 755.
- (145) Zhou, Z.-Y.; Kang, X.; Song, Y.; Chen, S. *Chemical Communications* **2011**, *47*, 6075.
- (146) He, G.; Song, Y.; Kang, X.; Chen, S. *Electrochimica Acta* **2013**, *94*, 98.
- (147) Meier, J.; Friedrich, K. A.; Stimming, U. *Faraday Discuss.* **2002**, *121*, 365.
- (148) Meier, J.; Schiotz, J.; Liu, P.; Norskov, J. K.; Stimming, U. *Chem. Phys. Lett.* **2004**, *390*, 440.
- (149) Zhou, Z.-Y.; Kang, X.; Song, Y.; Chen, S. *The Journal of Physical Chemistry C* **2012**, *116*, 10592.
- (150) Dubois, J. G. A.; Gerritsen, J. W.; Shafranjuk, S. E.; Boon, E. J. G.; Schmid, G.; Kempen, H. v. *EPL (Europhysics Letters)* **1996**, *33*, 279.
- (151) Ye, H.; Crooks, R. M. *J Am Chem Soc* **2007**, *129*, 3627.
- (152) Polsky, R.; Gill, R.; Kaganovsky, L.; Willner, I. *Anal. Chem.* **2006**, *78*, 2268.

- (153) Kang, X.; Zuckerman, N. B.; Konopelski, J. P.; Chen, S. *Angewandte Chemie* **2010**, *49*, 9496.
- (154) Chen, W.; Zuckerman, N. B.; Kang, X.; Ghosh, D.; Konopelski, J. P.; Chen, S. *The Journal of Physical Chemistry C* **2010**, *114*, 18146.
- (155) Ghosh, D.; Chen, S. *Chemical Physics Letters* **2008**, *465*, 115.
- (156) Kang, X.; Chen, S. *Nanoscale* **2012**, *4*, 4183.
- (157) Chen, W.; Zuckerman, N. B.; Lewis, J. W.; Konopelski, J. P.; Chen, S. *The Journal of Physical Chemistry C* **2009**, *113*, 16988.
- (158) Chen, W.; Pradhan, S.; Chen, S. *Nanoscale* **2011**, *3*, 2294.
- (159) Kang, X.; Song, Y.; Chen, S. *Journal of Materials Chemistry* **2012**, *22*, 19250.
- (160) Cheng, W.; Dong, S.; Wang, E. *Electrochemistry Communications* **2002**, *4*, 412.
- (161) Aslam, M.; Mulla, I. S.; Vijayamohanan, K. *Applied Physics Letters* **2001**, *79*, 689.
- (162) Taleb, A.; Yanpeng, X.; Munteanu, S.; Kanoufi, F.; Dubot, P. *Electrochimica Acta* **2013**, *88*, 621.
- (163) Skewis, L. R.; Reinhard, B. M. *ACS applied materials & interfaces* **2010**, *2*, 35.
- (164) Huang, T.; Murray, R. W. *The Journal of Physical Chemistry B* **2003**, *107*, 7434.
- (165) Wu, Z.; Jiang, D.-e.; Lanni, E.; Bier, M. E.; Jin, R. *The Journal of Physical Chemistry Letters* **2010**, *1*, 1423.
- (166) Chakraborty, I.; Govindarajan, A.; Erusappan, J.; Ghosh, A.; Pradeep, T.; Yoon, B.; Whetten, R. L.; Landman, U. *Nano Lett* **2012**, *12*, 5861.
- (167) Chen, S.; Sommers, J. M. *The Journal of Physical Chemistry B* **2001**, *105*, 8816.
- (168) Kakade, B. A.; Shintri, S. S.; Sathe, B. R.; Halligudi, S. B.; Pillai, V. K. *Advanced Materials* **2007**, *19*, 272.
- (169) Henglein, A.; Giersig, M. *The Journal of Physical Chemistry B* **2000**, *104*, 5056.
- (170) Cao, Y.; Jin, R.; Mirkin, C. A. *J Am Chem Soc* **2001**, *123*, 7961.
- (171) Malola, S.; Häkkinen, H. *The Journal of Physical Chemistry Letters* **2011**, *2*, 2316.
- (172) Negishi, Y.; Munakata, K.; Ohgake, W.; Nobusada, K. *The Journal of Physical Chemistry Letters* **2012**, *3*, 2209.
- (173) Negishi, Y.; Kurashige, W.; Niihori, Y.; Iwasa, T.; Nobusada, K. *Physical Chemistry Chemical Physics* **2010**, *12*, 6219.

- (174) Niihori, Y.; Kurashige, W.; Matsuzaki, M.; Negishi, Y. *Nanoscale* **2013**, *5*, 508.
- (175) Chandler, B. D.; Long, C. G.; Gilbertson, J. D.; Pursell, C. J.; Vijayaraghavan, G.; Stevenson, K. J. *The Journal of Physical Chemistry C* **2010**, *114*, 11498.
- (176) Ibanez, F. J.; Zamborini, F. P. *ACS nano* **2008**, *2*, 1543.
- (177) Cabo-Fernandez, L.; Bradley, D. F.; Romani, S.; Higgins, S. J.; Schiffrin, D. J. *Chemphyschem : a European journal of chemical physics and physical chemistry* **2012**, *13*, 2997.
- (178) Kim, J. M.; Koo, C. M.; Kim, J. *Electroanalysis* **2011**, *23*, 2019.
- (179) Stiles, R. L.; Balasubramanian, R.; Feldberg, S. W.; Murray, R. W. *J Am Chem Soc* **2008**, *130*, 1856.
- (180) Chen, S. *Langmuir* **2001**, *17*, 6664.
- (181) Sardar, R.; Beasley, C. A.; Murray, R. W. *Analytical Chemistry* **2009**, *81*, 6960.
- (182) Beasley, C. A.; Sardar, R.; Barnes, N. M.; Murray, R. W. *The Journal of Physical Chemistry C* **2010**, *114*, 18384.
- (183) Chow, K.-F.; Sardar, R.; Sassin, M. B.; Wallace, J. M.; Feldberg, S. W.; Rolison, D. R.; Long, J. W.; Murray, R. W. *The Journal of Physical Chemistry C* **2012**, *116*, 9283.
- (184) Dong, T. Y.; Shih, H. W.; Chang, L. S. *Langmuir* **2004**, *20*, 9340.
- (185) Gittins, D. I.; Bethell, D.; Schiffrin, D. J.; Nichols, R. J. *Nature* **2000**, *408*, 67.
- (186) Horikoshi, T.; Itoh, M.; Kurihara, M.; Kubo, K.; Nishihara, H. *Journal of Electroanalytical Chemistry* **1999**, *473*, 113.
- (187) Yamada, M.; Nishihara, H. *Chemical Communications* **2002**, 2578.
- (188) Yamada, M.; Tadera, T.; Kubo, K.; Nishihara, H. *The Journal of Physical Chemistry B* **2003**, *107*, 3703.
- (189) Yamada, M.; Nishihara, H. *Langmuir* **2003**, *19*, 8050.
- (190) Pietron, J. J.; Murray, R. W. *The Journal of Physical Chemistry B* **1999**, *103*, 4440.
- (191) Ingram, R. S.; Murray, R. W. *Langmuir* **1998**, *14*, 4115.
- (192) Yamada, M.; Tadera, T.; Kubo, K.; Nishihara, H. *Langmuir* **2001**, *17*, 2363.
- (193) Lopez-Acevedo, O.; Rintala, J.; Virtanen, S.; Femoni, C.; Tiozzo, C.; Gronbeck, H.; Pettersson, M.; Hakkinen, H. *J. Am. Chem. Soc.* **2009**, *131*, 12573.
- (194) Miles, D. T.; Murray, R. W. *Analytical Chemistry* **2001**, *73*, 921.

- (195) Chen, S.; Huang, K. *Langmuir* **2000**, *16*, 2014.
- (196) Gittins, D. I.; Bethell, D.; Nichols, R. J.; Schiffrin, D. J. *Advanced Materials* **1999**, *11*, 737.
- (197) Holm, A. H.; Ceccato, M.; Donkers, R. L.; Fabris, L.; Pace, G.; Maran, F. *Langmuir* **2006**, *22*, 10584.
- (198) Boal, A. K.; Rotello, V. M. *Journal of the American Chemical Society* **1999**, *121*, 4914.
- (199) Boal, A. K.; Rotello, V. M. *J Am Chem Soc* **2002**, *124*, 5019.
- (200) Bayir, A.; Jordan, B. J.; Verma, A.; Pollier, M. A.; Cooke, G.; Rotello, V. M. *Chem Commun (Camb)* **2006**, 4033.
- (201) Abad, J. M.; Gass, M.; Bleloch, A.; Schiffrin, D. J. *J Am Chem Soc* **2009**, *131*, 10229.
- (202) Mirkhalaf, F.; Schiffrin, D. J. *Langmuir* **2010**, *26*, 14995.
- (203) Zhu, Y.; Qian, H.; Drake, B. A.; Jin, R. *Angewandte Chemie* **2010**, *49*, 1295.
- (204) Lyalin, A.; Taketsugu, T. *The Journal of Physical Chemistry Letters* **2010**, *1*, 1752.
- (205) Tang, D.; Hu, C. *The Journal of Physical Chemistry Letters* **2011**, *2*, 2972.
- (206) Negishi, Y.; Mizuno, M.; Hirayama, M.; Omatoi, M.; Takayama, T.; Iwase, A.; Kudo, A. *Nanoscale* **2013**, *5*, 7188.
- (207) Zaramella, D.; Scrimin, P.; Prins, L. J. *J Am Chem Soc* **2012**, *134*, 8396.
- (208) Novo, C.; Funston, A. M.; Mulvaney, P. *Nat. Nanotechnol.* **2008**, *3*, 598.
- (209) Xiao, X.; Bard, A. J. *J Am Chem Soc* **2007**, *129*, 9610.
- (210) Xiao, X.; Pan, S.; Jang, J. S.; Fan, F.-R. F.; Bard, A. J. *The Journal of Physical Chemistry C* **2009**, *113*, 14978.
- (211) Xiao, X.; Fan, F. R.; Zhou, J.; Bard, A. J. *J Am Chem Soc* **2008**, *130*, 16669.
- (212) Baron, R.; Wildgoose, G. G.; Compton, R. G. *Journal of nanoscience and nanotechnology* **2009**, *9*, 2274.
- (213) Nakashima, D.; Marken, F.; Oyama, M. *Electroanalysis* **2013**, *25*, 975.
- (214) Xu, L.-P.; Chen, S. *Chemical Physics Letters* **2009**, *468*, 222.
- (215) Shao, Y.; Mirkin, M. V.; Fish, G.; Kokotov, S.; Palanker, D.; Lewis, A. *Anal. Chem.* **1997**, *69*, 1627.

- (216) Wohltjen, H.; Snow, A. W. *Analytical Chemistry* **1998**, *70*, 2856.
- (217) Cai, Q. Y.; Zellers, E. T. *Anal Chem* **2002**, *74*, 3533.
- (218) Steinecker, W. H.; Rowe, M. P.; Zellers, E. T. *Anal Chem* **2007**, *79*, 4977.
- (219) Raguse, B.; Chow, E.; Barton, C. S.; Wieczorek, L. *Analytical Chemistry* **2007**, *79*, 7333.
- (220) Ibanez, F. J.; Gowrishetty, U.; Crain, M. M.; Walsh, K. M.; Zamborini, F. P. *Anal Chem* **2006**, *78*, 753.
- (221) Kumar, S. S.; Kwak, K.; Lee, D. *Analytical Chemistry* **2011**, *83*, 3244.
- (222) Li, L.; Zhu, A.; Tian, Y. *Chem Commun (Camb)* **2013**, *49*, 1279.
- (223) Chauhan, N.; Singh, A.; Narang, J.; Dahiya, S.; Pundir, C. S. *The Analyst* **2012**, *137*, 5113.
- (224) Jeong, B.; Akter, R.; Han, O. H.; Rhee, C. K.; Rahman, M. A. *Anal Chem* **2013**, *85*, 1784.
- (225) Loftus, A. F.; Reighard, K. P.; Kapourales, S. A.; Leopold, M. C. *J Am Chem Soc* **2008**, *130*, 1649.
- (226) Tran, T. D.; Vargo, M. L.; Gerig, J. K.; Gulka, C. P.; Trawick, M. L.; Dattelbaum, J. D.; Leopold, M. C. *J Colloid Interface Sci* **2010**, *352*, 50.
- (227) Vargo, M. L.; Gulka, C. P.; Gerig, J. K.; Manieri, C. M.; Dattelbaum, J. D.; Marks, C. B.; Lawrence, N. T.; Trawick, M. L.; Leopold, M. C. *Langmuir* **2010**, *26*, 560.
- (228) Campbell-Rance, D. S.; Doan, T. T.; Leopold, M. C. *Journal of Electroanalytical Chemistry* **2011**, *662*, 343.
- (229) Xia, N.; Deng, D.; Zhang, L.; Yuan, B.; Jing, M.; Du, J.; Liu, L. *Biosensors & bioelectronics* **2013**, *43*, 155.
- (230) Gao, Z. D.; Guan, F. F.; Li, C. Y.; Liu, H. F.; Song, Y. Y. *Biosensors & bioelectronics* **2013**, *41*, 771.
- (231) Ackerson, C. J.; Jadzinsky, P. D.; Jensen, G. J.; Kornberg, R. D. *J Am Chem Soc* **2006**, *128*, 2635.
- (232) de la Escosura-Muniz, A.; Parolo, C.; Maran, F.; Mekoci, A. *Nanoscale* **2011**, *3*, 3350.
- (233) Wang, J.; Xu, D.; Kawde, A. N.; Polsky, R. *Anal Chem* **2001**, *73*, 5576.
- (234) Nakagawa, T.; Beasley, C. A.; Murray, R. W. *The Journal of Physical Chemistry C* **2009**, *113*, 12958.

- (235) Nakagawa, T.; Bjorge, N. S.; Murray, R. W. *Journal of the American Chemical Society* **2009**, *131*, 15578.
- (236) Michaux, K. E.; Murray, R. W. *Langmuir* **2013**, *29*, 12254.
- (237) Gambardella, A. A.; Feldberg, S. W.; Murray, R. W. *Journal of the American Chemical Society* **2012**, *134*, 5774.
- (238) Gambardella, A. A.; Bjorge, N. S.; Alspaugh, V. K.; Murray, R. W. *The Journal of Physical Chemistry C* **2011**, *115*, 21659.
- (239) Chang, C. H.; Yuen, T. S.; Nagao, Y.; Yugami, H. *Journal of Power Sources* **2010**, *195*, 5938.
- (240) Salimi, A.; Hallaj, R.; Kavosi, B.; Hagighi, B. *Analytica Chimica Acta* **2010**, *661*, 28.
- (241) Sanchez Casalongue, H. G.; Ng, M. L.; Kaya, S.; Friebe, D.; Ogasawara, H.; Nilsson, A. *Angewandte Chemie* **2014**, *126*, 7297.
- (242) Parker, J. F.; Weaver, J. E. F.; McCallum, F.; Fields-Zinna, C. A.; Murray, R. W. *Langmuir* **2010**, *26*, 13650.
- (243) Parker, J. F.; Fields-Zinna, C. A.; Murray, R. W. *Accounts of chemical research* **2010**, *43*, 1289.
- (244) Kurashige, W.; Yamaguchi, M.; Nobusada, K.; Negishi, Y. *The Journal of Physical Chemistry Letters* **2012**, *3*, 2649.
- (245) Negishi, Y.; Kurashige, W.; Kamimura, U. *Langmuir* **2011**, *27*, 12289.
- (246) Meng, X.; Xu, Q.; Wang, S.; Zhu, M. *Nanoscale* **2012**, *4*, 4161.
- (247) Qian, H.; Zhu, Y.; Jin, R. *ACS nano* **2009**, *3*, 3795.
- (248) Wang, Z. W.; Toikkanen, O.; Yin, F.; Li, Z. Y.; Quinn, B. M.; Palmer, R. E. *J Am Chem Soc* **2010**, *132*, 2854.
- (249) Qian, H.; Jin, R. *Chemistry of Materials* **2011**, *23*, 2209.
- (250) Lee, W.-Y.; Hostetler, M. J.; Murray, R. W.; Majda, M. *Israel Journal of Chemistry* **1997**, *37*, 213.
- (251) Chen, S. *Journal of Materials Chemistry* **2007**, *17*, 4115.
- (252) Chaki, N. K.; Singh, P.; Dharmadhikari, C. V.; Vijayamohanan, K. P. *Langmuir* **2004**, *20*, 10208.
- (253) Chaki, N. K.; Kakade, B.; Vijayamohanan, K. P.; Singh, P.; Dharmadhikari, C. V. *Physical Chemistry Chemical Physics* **2006**, *8*, 1837.

- (254) Suganuma, Y.; Trudeau, P.-E.; Dhirani, A.-A.; Leathem, B.; Shieh, B. *The Journal of Chemical Physics* **2003**, *118*, 9769.
- (255) Suganuma, Y.; Trudeau, P. E.; Dhirani, A. A. *Physical Review B* **2002**, *66*, 241405.
- (256) Chen, S.; Xu, L.-P.; Pradhan, S.; Chen, W. *Solid State Communications* **2007**, *144*, 124.
- (257) Miles, D. T.; Murray, R. W. *Analytical Chemistry* **2003**, *75*, 1251.
- (258) Joanis, P.; Tie, M.; Dhirani, A.-A. *Langmuir* **2013**, *29*, 1264.
- (259) Jeffrey, L. D.; Al-Amin, D. *Nanotechnology* **2008**, *19*, 025202.
- (260) Dunford, J. L.; Suganuma, Y.; Dhirani, A. A.; Statt, B. *Physical Review B* **2005**, *72*, 075441.
- (261) Zabet-Khosousi, A.; Trudeau, P.-E.; Suganuma, Y.; Dhirani, A.-A.; Statt, B. *Physical review letters* **2006**, *96*, 156403.
- (262) Li, C. P.; Wu, C. H.; Wei, K. H.; Sheu, J. T.; Huang, J. Y.; Jeng, U. S.; Liang, K. S. *Advanced Functional Materials* **2007**, *17*, 2283.
- (263) Zabet-Khosousi, A.; Dhirani, A. A. *Chem Rev* **2008**, *108*, 4072.
- (264) Pettibone, J. M.; Hudgens, J. W. *ACS nano* **2011**, *5*, 2989.
- (265) Holstein, T. In *Tunneling in Biological Systems*; Britton Chance, R. A. M., Don Charles DeVault, J. Robert Schrieffer, Hans Frauenfelder, Norman Sutin, Ed.; Academic Press: New York, NY, 1979, p 129.
- (266) B. P. Block, S. A. B., Therald Moeller, J. D. Chrisp, P. Gentile and L. O. Morgan In *Inorganic Syntheses*; Bailar, J. C., Ed.; McGraw-Hill Book Company, Inc.: New York, NY, 1953; Vol. 4, p 14.
- (267) Glemser, O.; Sauer, H. In *Handbook of Preparative Inorganic Chemistry*; 2 ed.; Brauer, G., Ed.; Academic Press: New York, 1963; Vol. 2, p 1057.
- (268) Lee, D.; Donkers, R. L.; Wang, G.; Harper, A. S.; Murray, R. W. *Journal of the American Chemical Society* **2004**, *126*, 6193.
- (269) Guidez, E. B.; Aikens, C. M. *Physical chemistry chemical physics : PCCP* **2012**, *14*, 4287.
- (270) Chen, S. *Journal of Electroanalytical Chemistry* **2004**, *574*, 153.
- (271) Hostetler, M. J.; Wingate, J. E.; Zhong, C.-J.; Harris, J. E.; Vachet, R. W.; Clark, M. R.; Londono, J. D.; Green, S. J.; Stokes, J. J.; Wignall, G. D.; Glish, G. L.; Porter, M. D.; Evans, N. D.; Murray, R. W. *Langmuir* **1998**, *14*, 17.

- (272) Mars, A.; Parolo, C.; Raouafi, N.; Boujlel, K.; Merkoci, A. *Journal of Materials Chemistry B* **2013**, *1*, 2951.
- (273) Diaz, A. F.; Castillo, J. I. *J. Chem. Soc. Chem. Comm.* **1980**, *9*, 397.
- (274) Pickup, P. G.; Kutner, W.; Leidner, C. R.; Murray, R. W. *J. Am. Chem. Soc.* **1984**, *106*, 1991.
- (275) Pickup, P. G.; Murray, R. W. *J. Am. Chem. Soc.* **1983**, *105*, 4510.
- (276) Pickup, P. G.; Murray, R. W. *J. Electrochem. Soc.* **1984**, *131*, 833.
- (277) Feldberg, S. W. *J. Am. Chem. Soc.* **1984**, *106*, 4671.
- (278) Feldman, B. J.; Murray, R. W. *J. Am. Chem. Soc.* **1985**, *107*, 872.
- (279) Ofer, D.; Crooks, R. M.; Wrighton, M. S. *J. Am. Chem. Soc.* **1990**, *112*, 7869.
- (280) Paul, E. W.; Ricco, A. J.; Wrighton, M. S. *J. Am. Chem. Soc.* **1985**, *89*, 1441.
- (281) Thackeray, J. W.; White, H. S.; Wrighton, M. S. *J. Am. Chem. Soc.* **1985**, *89*, 5133.
- (282) Jernigan, J. C.; Wilbourn, K. O.; Murray, R. W. *Journal of Electroanalytical Chemistry and Interfacial Electrochemistry* **1987**, *222*, 193.
- (283) Conway, B. E.; Mozota, J. *Electrochimica Acta* **1983**, *28*, 9.
- (284) Carducci, T. M.; Murray, R. W. In *Nanoelectrochemistry*; Mirkin, M. V., Amemiya, S., Eds.; CRC Press, a Taylor & Francis group: 2015.
- (285) Song, Y.; Wang, S.; Zhang, J.; Kang, X.; Chen, S.; Li, P.; Sheng, H.; Zhu, M. *J Am Chem Soc* **2014**, *136*, 2963.
- (286) Kurashige, W.; Yamazoe, S.; Kanehira, K.; Tsukuda, T.; Negishi, Y. *J. Phys. Chem. Lett.* **2013**, *4*, 3181.
- (287) Kurashige, W.; Yamazoe, S.; Yamaguchi, M.; Nishido, K.; Nobusada, K.; Tsukuda, T.; Negishi, Y. *The Journal of Physical Chemistry Letters* **2014**, *5*, 2072.
- (288) Chakraborty, I.; Kurashige, W.; Kanehira, K.; Gell, L.; Häkkinen, H.; Negishi, Y.; Pradeep, T. *The Journal of Physical Chemistry Letters* **2013**, *4*, 3351.
- (289) MacDonald, D. G.; Kübel, C.; Corrigan, J. F. *Inorganic Chemistry* **2011**, *50*, 3252.
- (290) Carducci, T. M.; Blackwell, R. E.; Murray, R. W. *J Am Chem Soc* **2014**, *136*, 11182.
- (291) Bordwell, F. G.; Hughes, D. L. *The Journal of Organic Chemistry* **1982**, *47*, 3224.

- (292) Courtet-Coupez, J.; Laouenan, A.; LeDemezet, M. *Compt Rend C* **1968**, 267, 1475.
- (293) Hohman, J. N.; Thomas, J. C.; Zhao, Y.; Auluck, H.; Kim, M.; Vijselaar, W.; Kommeren, S.; Terfort, A.; Weiss, P. S. *J Am Chem Soc* **2014**, 136, 8110.
- (294) Patrone, L.; Palacin, S.; Bourgoïn, J. P.; Lagoute, J.; Zambelli, T.; Gauthier, S. *Chemical Physics* **2002**, 281, 325.
- (295) Monnell, J. D.; Stapleton, J. J.; Jackiw, J. J.; Dunbar, T.; Reinerth, W. A.; Dirk, S. M.; Tour, J. M.; Allara, D. L.; Weiss, P. S. *The Journal of Physical Chemistry B* **2004**, 108, 9834.